Title

Characterization of Light Scattering in Transparent Polycrystalline Laser Ceramics

Permalink

https://escholarship.org/uc/item/0545x114

Author

Sharma, Saurabh

Publication Date

2013

Peer reviewed|Thesis/dissertation

UNIVERSITY OF CALIFORNIA

Los Angeles

Characterization of Light Scattering in

Transparent Polycrystalline Laser Ceramics

A dissertation submitted in partial satisfaction of the

requirements for the degree Doctor of Philosophy

in Materials Science Engineering

by

Saurabh Sharma

2013

ABSTRACT OF THE DISSERTATION

Characterization of Light Scattering in

Transparent Polycrystalline Laser Ceramics

By

Saurabh Sharma

Doctor of Philosophy in Materials Science Engineering

University of California, Los Angeles, 2013

Professor Mark S. Goorsky, Chair

Limitations in single-crystal growth technology have led to the development of transparent Polycrystalline Laser Materials (PLMs) as viable alternatives towards fabricating large dimension laser gain media having engineered dopant profiles to improve the thermo-optic properties and continue power scaling of solid-state laser systems operating in the 1 - 5 μm wavelength range. Bulk scattering due to non-uniform refractive index distribution is the primary loss mechanism in the PLMs, resulting in the degradation of laser performance and lower output power. The objective of this dissertation was to formulate a methodology for fast, reliable and accurate identification and characterization of bulk scatter in Erbium (Er) and Neodymium (Nd) doped YAG (Yttrium Aluminum Garnet – $Y_3Al_5O_{12}$) and Yttria (Yttrium Oxide – Y_2O_3) PLMs. Scanning Electron Microscopy, Transmission Electron Microscopy, and

Confocal Laser Scanning Microscopy were used for material characterization and investigation of PLM microstructures at various stages of fabrication, thus identifying the source of refractive index inhomogeneities, which result in bulk scattering. Three optical characterization techniques, Transmitted Beam Wavefront Profiling (TBWP), Angle Resolved Scatter (ARS) measurements, and Schlieren Imaging, to identify bulk scatter in PLMs, are developed. TBWP was able to directly and quickly image the distortions introduced to a propagating laser beam caused by the presence of bulk scattering in the PLMs. ARS was able to map the distribution of the scattered intensity in space, and was found to be very sensitive for comparing samples. A modified white light Schlieren imaging setup utilizing variable focusing capability, demonstrated high sensitivity for directly imaging local spatial variations in refractive index across and through the entire PLM regardless of dimensions. Finally, by comparing laser performance of 0.9% Nd:YAG single crystal, high quality and low quality PLMs, with results from TBWP and Schlieren Images, the utility of characterization techniques towards identifying bulk scatter and assessing the optical quality are validated. The methods developed are applicable towards the characterization of any transparent material exhibiting bulk scatter.

The dissertation of Saurabh Sharma is approved.

Bruce S. Dunn

Ioanna Kakoulli

Robin L. Garrell

Ramesh K. Shori

Mark S. Goorsky, Committee Chair

University of California, Los Angeles

2013

Table of Contents

List of Figures

List of Tables

Acknowledgements

During all these years at UCLA (University of California, Los Angeles), there have been many people I have had the opportunity to meet and learn from, and I would like to remember and thank them all. First of all, my advisor, Prof. Mark S. Goorsky, who has been an excellent teacher. I would like to thank Prof. Bruce Dunn, Prof. Robin Garrell, Prof. Ioanna Kakoulli and Dr. Ramesh Shori, for sparing their valuable time to be members on my dissertation committee.

I would like to specially thank Dr. Ramesh Shori for being my mentor, nurturing me all these years and helping me evolve this far. These few words are the least to express my gratitude, and that I continue to cherish this relationship. I would next like to thank my colleague and friend, Dr. Jerome Keith Miller, as most of the Schlieren imaging setup and laser work has been possible because of your initial work, continued guidance and support during my research path.

I would like to acknowledge the support of the US Navy, NAWC-WD, China Lake to have given me the opportunity to work during my research, and to be a part of an excellent work environment and wonderful co-workers. I would like to thank my Division head Ms. Joni M. Pentony and Physics Branch head Dr. K. K. Law at China Lake, for all the encouragement and support. The discussions with you on all the topics research or otherwise, have been most enlightening, and I look forward to having more.

I would like to thank the Materials Science and Engineering faculty and the support staff at UCLA. It is an honor to be a part of such an elite institution; it has been

VITA

2003	Bachelor of Engineering in Electronics & Telecommunications (JSS-ATE) B.R. Ambedkar University, Agra, India
2006	Master of Science in Electrical Engineering, University of California, Los Angeles Los Angeles, CA
2007	Engineer, Advanced R&D Div. Spectra Physics - Newport Lasers, Sunnyvale, CA
2010	Master of Science in Electrical Engineering, University of California, Los Angeles Los Angeles, CA
2010 - Present	Engineer, Physics div. US Navy (NAWC-WD), China Lake, CA

PUBLICATIONS

Saurabh Sharma and M. S. Goorsky, "High Resolution Double-Crystal X-ray Diffraction Imaging for Interfacial Defect Detection in Bonded Wafers", ECS Trans., volume 50, issue 7, (2013).

Saurabh Sharma, Ramesh Shori, J. Keith Miller, "Spectroscopic properties of Er-sesquoxides", Proc. SPIE 8235, Solid State Lasers XXI: Technology and Devices, 82350F (2012).

K. Law, R. Shori, J. Miller, **Saurabh Sharma,** "Mid-wave/long-wave infrared lasers and their sensing applications" Proc. SPIE 8031, Micro- and Nanotechnology Sensors, Systems, and Applications III, 80312E (2011).

J. Ballato, T. Hawkins, P. Foy, R. Stolen, B. Kokuoz, M. Ellison, C. McMillen, J. Reppert, A. M. Rao, M. Daw, **Saurabh Sharma**, R. Shori, O. Stafsudd, R. R. Rice, D. R. Powers, "Silicon optical fiber", Optics Express, Vol. 16, Issue 23, pp. 18675-18683 (2008).

Saurabh Sharma, C. Vergien, R. Shori, "Room temperature multi-wavelength operation in Er:YAlO3" Proc. SPIE 6451, Solid State Lasers XVI: Technology and Devices, 64510Q (2007)

Chapter 1

Introduction

1.1   Laser Applications

LASER (Light Amplification by Stimulated Emission of Radiation) is one of the few inventions by man that has been the enabling technology leading to a turning point in the development of science and engineering. Ever since the first demonstration of laser in 1960, a wide variety of hosts (gases, liquids, semiconductors, solids (crystalline and polycrystalline, glasses, fluorides both in bulk and fiber form) doped with different rare earth (Lanthanides or inner transition) elements and even electrons, have been utilized for generation of coherent Laser radiation [1, 2].

The unique properties of lasers (spatial and temporal coherence, high brightness and monochromatic emission), have enabled the development of diverse range of scientific [3, 4], medical and dental [5 - 7], industrial [8, 9], and military [10, 11] applications. Many of these applications were not even conceivable until the advent of the laser. As the number of applications using lasers has grown, so has the diversity of host materials doped with rare earth elements (active ions), with each new discovery being driven by the need to generate specific optical parameters like emission wavelengths (UV – LWIR – THz), output waveforms (continuous wave or pulsed durations as short as atto-seconds), and output power levels (up to 100s kW in the case of the chemical oxygen-iodine laser). Quality of the laser beam, namely, the spectral line-width, beam divergence and spatial profile (diffraction limited or near-diffraction limited) also represent important parameters for many applications.

1.2   Solid State Laser Materials

The most common type of lasers used in many of the research, industrial and military applications are Solid State Lasers (SSL). Depending on the host material (i.e., oxides such as YAG (Yttrium Aluminum Garnet - $Y_3Al_5O_{12}$), YVO_3, Al_2O_3, GGG (Gadolinium Gallium Garnet - $Gd_3Ga_5O_{12}$); fluorides such as YLF, LuLiF; II-VI; and glasses) and the active ions doped into the host material (i.e., rare earth elements such as Yb, Nd, Tm, Ho, Er, or even transition metals such as Cr^{+2} or Fe^{+2}), it is possible to generate laser wavelengths ranging from UV to the Mid-IR [12]. Virtually all gain media used in SSL are single crystals, which are usually grown by Czochralski (CZ) or Bridgman method [13].

Regardless of the application, the trend among the laser research community has been towards generation of higher and higher output power levels and with near theoretical optical-optical conversion efficiency between the pump and lasing wavelengths. In the case of military applications, the need for higher output power combined with emission in mid-wave IR spectral region (Mid-IR: 2 - 5 µm) is not just a trend but the driving force behind the growth in photonic materials development and thermal management engineering.

The thermal management challenges have led to rebirth in development of transparent sesquoxides (e.g., Y_2O_3, Lu_2O_3, and Sc_2O_3) [14]. As these sesquoxides (Y_2O_3, Lu_2O_3, and Sc_2O_3) have higher thermal conductivity compared to YAG (13 - 16 W/m-K vs. ~ 11 W/m-K), they appear to be better suited for high laser power applications. As the sesquoxides materials are refractory in nature, with melting points higher than 2400 °C, reproducibility in growing large dimension single-crystal, of very high purity and optically transparent, has proven to be expensive and difficult [12, 13, 71].

The growth of laser quality single-crystal materials, like YAG, is still a "black art", involving processes and growth techniques known to very few in the crystal growth field. Within the US, there are only handful of entities / individuals that have the necessary skills and capabilities to grow large dimension (~ 6" diameter x 12" length) laser quality YAG boules. There are no published reports of anyone having grown (via CZ or Bridgeman methods) laser quality transparent sesquoxide materials in any large dimensions [71, 74, 80].

In the absence of usable dimension and laser quality sesquoxides, the demand for laser gain material for use in high power (kW-class) bulk SSL, is being momentarily addressed by fabrication and bonding of plates of Nd:YAG or Yb:YAG media [14]. The YAG plate dimensions used in high power lasers are typically about 6 cm x 6 cm x 2 cm. The costs associated with bonding was often times on par with the fabrication cost of just the gain media , making the final costs of just the laser gain media even higher than the boule costs.

The growth of large dimension single crystals, by the CZ method is limited to YAG and similar oxide (like GGG) materials which have low melting temperatures ~1940 $^{\circ}$C and which can be grown in iridium crucibles (melting point 2466 $^{\circ}$C). The growth of a large dimension (typically 6" diam. x 16" long) Nd:YAG or Yb:YAG boule by CZ method is costly (~ $50K per growth run) and time-consuming (~ 4 weeks).

Even after having grown such a boule, the yield of usable laser quality material from each boule is at best 60% due to defects in the boule caused by birefringence stresses and non-uniform doping profile, resulting from lattice mismatch between the active ion (in this case Nd or Yb) and the Y site, in the YAG host. High Resolution Double-Crystal X-Ray Topography was found

to be ideal towards the identification of stresses in the crystal (Figure 1.1 (c)), but performing similar analysis is not applicable in the case of Polycrystalline Laser Materials (PLMs).

The segregation of the active ion in the melt (e.g.,, Nd in case of Nd:YAG) leads to the maximum achievable doping of ~ 1.1% which adds even more constraints on the laser design [12]. Until very recently, the yield from bonding parts was less than half, leading to a net-yield of usable material to < 30% from a boule.

(a)   (b)   (c)
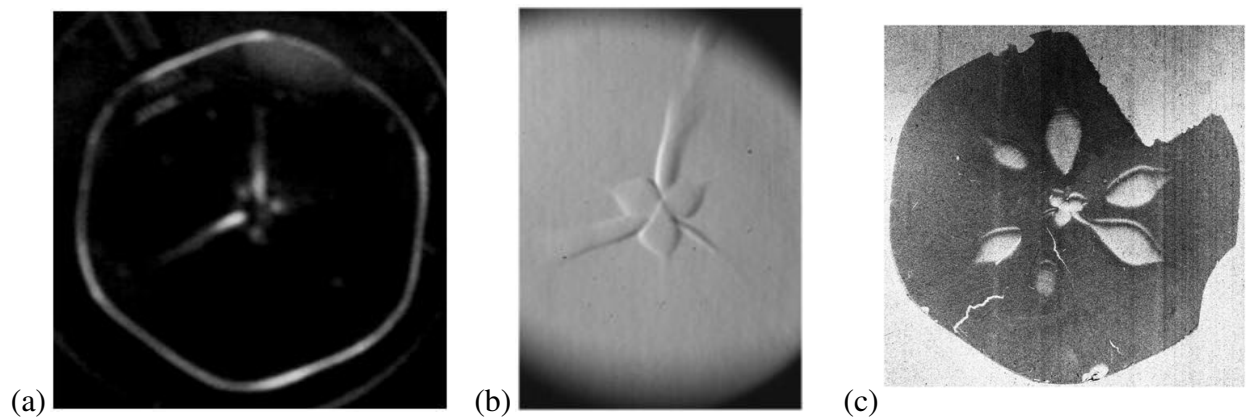
Figure 1.1: Image of a Single Crystal 1% Erbium doped YAG (1 inch in diameter) under (a) Cross-polarized, (b) Schlieren and (c) High Resolution Double-Crystal X-Ray Topography (top right section not imaged due to shadowing from magnets holding crystal). We clearly see the center of the crystal is highly stressed, and has three 'arms' spreading outwards. The regions between these arms (< 60 % area) is of uniform and low stress, and is useful for laser applications.

1.3   Polycrystalline Laser Media (PLM)

The progress for generating higher and higher power levels (10s - 100s kW) from a single aperture bulk SSL has been limited, due to the lack of availability of large dimensioned laser gain media. One solution has been to bond multiple pieces of laser gain media, ending up with a single larger dimension piece (typically 4 ~ 5 x starting dimension) [14].

While bonding has yielded larger pieces of laser gain media, the yield, reproducibility, and prohibitive costs of laser quality samples (i.e., laser quality transparency and no visible bond lines) have proven to be an impractical long-term solution.

A more attractive alternative has been to fabricate Polycrystalline Laser Materials (PLMs) via powder compaction [15]. The first reported lasing in PLMs was demonstrated in 1964 in Dy:CaF$_2$ glass-ceramic which was fabricated via hot-pressing of powders [16]. Two years later, lasing was demonstrated in ceramic Nd:YAG which was fabricated by via cold-pressing and sintering [17]. Another eight years later, laser oscillations were demonstrated in sesquoxides doped with Nd [18].

All these initial demonstrations of fabrication of PLMs were limited to material of small dimensions, low output power levels (few mW at most), and often at liquid nitrogen or liquid helium temperatures. It was not until almost two decades later that ceramic PLM became popular again when ceramic Nd:YAG was shown to lase at room temperature generating a few hundreds of mW [19].

Even though powder compaction had been known since the 1940s, there was little success in producing laser quality transparent materials until the mid - 1990s. PLMs are being considered as the enabling technology for high power laser applications. In addition to larger dimensioned laser gain media, PLMs offer many advantages over CZ growth technique such as lower near-net-shape, composite design, complex doping profiles, compositions, and configurations; that have been but an elusive dream using a conventional CZ crystal growth technique.

Another key advantage, in terms of processing is that the fabrication of PLMs requires much lower processing temperature, e.g., in case of YAG ~1500 $^{\circ}$C vs. ~2000 $^{\circ}$C required in melting for CZ growth. The presence of impurities is one the biggest contributing factors, that lead to laser performance degradation by interacting with the optically active (e.g.,, the rare earth elements such as Nd, Yb, Tm, Er…) dopant ion [12]. The lower processing temperature (compared to the melting point of YAG and sesquoxides) also reduces the possibility of contamination by impurities in the finished sample. The fabrication of transparent PLM is achieved using methods which resemble a mix of powder metallurgy and traditional ceramic or pottery making, which is why they are sometimes also called 'Fine-ceramics'. The difference lies in the processing steps which employs very precise control of processing and manufacturing conditions, and require the use of ultra high purity starting powders [14, 20].

Recent advances in material processing techniques have demonstrated the ability of fabricating large dimension highly transparent polycrystalline material with optical, thermal, and mechanical properties similar to those of single-crystal laser materials [14]. Since the first lasing in transparent (oxide) ceramic laser material as reported in 1995, there have been many advances in both the PLM development and lasers designs utilizing PLMs [19 - 24].

Currently, the Solid State Heat Capacity Laser (SSHCL) at Lawrence Livermore National Labs uses the world's largest dimensioned laser-quality transparent (Nd:YAG) PLMs as amplifier slabs with dimensions of 10cm x 10cm x 2cm [25]. Even though large dimension polycrystalline ceramic materials have been mass produced, the reproducibility of transparent laser quality, large dimensioned PLMs with low bulk scattering continues to be a challenge.

1.4   Bulk Scattering Loss

The loss or extinction coefficient used to characterize laser material has significant impact on the laser performance in terms of output power and spatial beam quality. In general, the attenuation or extinction of a propagating electromagnetic (EM) wave through any material is due to loss from absorption or scattering [26, 27]. Absorption in a material is a conversion of energy from one form to another form (usually heat). Scattering, on the other hand, not only causes the redirection of the incident energy which effectively appears as a loss in incident intensity along the direction of propagation, but also leads to wavefront distortion of the transmitted EM wave [28].

The total scattering loss coefficient is attributed to surface scatter, resulting from material surface imperfections, and bulk-scatter, resulting from the presence of volumetric microstructure defects. Surface scattering is an important and complex process and has been addressed in depth in the literature [29, 30]. Suppression of the surface scatter component is achieved by polishing the surfaces of the material until the surface micro-roughness is $\lambda/50$ or better (where λ is typically 632 nm from a He-Ne laser).

At the microscopic level, the loss due to bulk scattering is a result of the interaction of the EM wave with the microstructure of the sample. The morphology of microstructures present in the sample is dependent on the PLM fabrication process. The discontinuity of the dielectric constant is manifested as variations in the refractive index, distributed across the volume of the PLM sample, resulting in bulk scattering. Figure 1.2 depicts the different types of microstructures such as pores, voids, secondary phases, inclusions, grain boundaries, and density fluctuations within the PLM that lead to the refractive index variations [31].
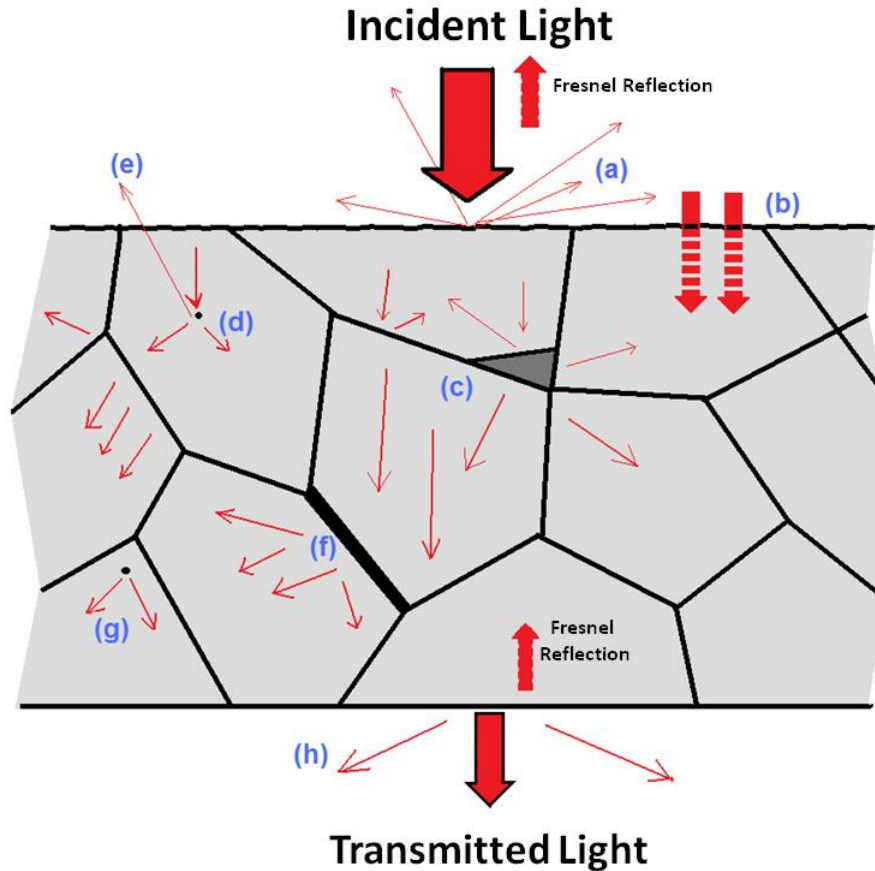
Figure 1.2: Bulk scattering loss in a polycrystalline material is due to scattering centers that result in an effective refractive index discontinuity in the material. The light wave incident on the polycrystalline material suffers losses from the following: (a) surface scatter, (b) absorption, (c) voids, (d) scatter from pores, (e) back scatter from pores, (f) secondary phase, (g) forward scatter from pores, (h) back surface scatter.

The bulk scattering observed in PLMs is a result of the collective interference effects resulting from this microstructure, which behave as multiple scattering centers. The amount of bulk scattering (both magnitude and spatial distribution) observed in a PLM depends on the density, and the effective cross section of the scattering centers [32, 33]. All polycrystalline materials exhibit internal interfaces in the form of grain boundaries which can be viewed as surfaces separating the regions of crystalline order. Domains in glass are volumes of short-range order which are similar to the grains in a polycrystalline solid.

Light scattering in optical quality glass fiber is due to the presence of molecular level compositional fluctuations and irregularities in the fiber structure [34]. While the compositional fluctuation is much smaller than the wavelength of light (where $\lambda \sim 500$ nm), however, over the optical path length across the fiber, the cumulative effect of the fluctuations results in loss. This represents a process that is indicative of presence of a distributed loss, and the cumulative effect manifests as bulk scattering. Characterization of bulk scattering provides a figure of merit that represents an effective in-line transmission loss of energy, as an EM wave propagate through the PLM.

1.5   Characterization of Bulk Scatter

Even though the first reference attributing loss in transparent polycrystalline materials to bulk scatter was identified over four decades ago [18], a systematic and thorough investigation was not possible until recently due to lack of availability and need of transparent ceramic materials [28]. The issue of transparency in ceramic (specifically hot-pressed alumina) and the methodology for identifying bulk scatter was first addressed in 1979 [35, 36].

In efforts aimed at developing transparent polycrystalline alumina for use in high-pressure light bulbs, it was predicted that a very low volume fraction of pores (leading to > 99.5% of maximum density) was necessary in order to achieve the theoretical transmission limit through polycrystalline alumina [25, 37]. The technique for testing bulk-scatter amounted to placing a very thin sample (~ mm) of the polycrystalline material on a black and white typed text, and visually assessing the transparency on the basis of whether or not the text underneath was clearly visible [36]. The authors mentioned that the assessment of transparency was very subjective and left to the judgment of the human eye.

9

In one of the first systematic studies investigating source of scattering in transparent polycrystalline YAG, it was observed that the scattering centers were randomly distributed in the materials, and were of varied morphology and dimensions [38, 39]. The diversity in size of the scattering centers suggests that bulk scattering cannot be accurately modeled using simple Rayleigh or Mie scattering theories. To date, the bulk-scattering coefficient for PLMs has been estimated using a simplified form of the Beer-Lambert equation at a randomly chosen wavelength. Traditionally, the Beer-Lambert law is used to calculate absorption coefficient in rarified gases and dilute liquids, from transmission measurements [26 – 28].

The transmission measurements are performed using very small volumes, to minimize the optical path length and the errors arising from multiple scattering and interference effects [40 - 42]. While the Beer-Lambert technique leads to a quantitative assessment for lumped transmission loss through a sample, the technique is inherently incapable of yielding any information as to the (microscopic) origins leading to the lumped transmission loss.

The characterization of bulk scattering in ceramic PLMs is a necessary metric to evaluate the fabrication process and to qualify the ceramic sample for use as a laser material. Accordingly, another technique routinely used to directly evaluate the quality of PLMs, is to compare the laser performance. Specifically, the threshold, total output power versus input power and the slope efficiency are compared, where the only variation in the setup is the laser gain material.

In the baseline setup, the laser gain media is a crystalline laser material and in the experimental setup, the laser gain media is a PLM. The crystalline and PLM gain media are identical in dimension, composition, and any anti-reflective coatings. Not only is this technique

time consuming, but also very costly. There is considerable effort required in the selection and preparation of the selected samples and objectively comparing the laser performance. In the absence of an alternative methodology to determine bulk scattering and assess the quality of PLM, the above methodology continues to be utilized throughout the industry and academia.

Bulk scattering in PLM is a complex process, and has been identified to be the primary cause of in-line transmission loss and spatial distortion of a propagating laser beam. An accurate determination of bulk scattering is critical, for predicting the performance of lasers utilizing PLMs [19, 43]. Despite all the advances in fabrication of transparent laser quality PLMs over the past two decades, the determination of bulk scatter in PLMs is performed using a simplified adaptation of the qualitative method outlined in the first study investigating transparency in hot-pressed alumina.

To reiterate, the technique relies on looking at a black and white pattern (like typed or printed text) or lettering through a very thin sample (< few mm thick) of the polycrystalline ceramic material, and determining the presence of bulk scatter based on whether or not the black text or pattern is clearly visible. Because the characterization of bulk scatter in transparent PLM is not a single point measurement, it should not and cannot be represented by single value (α_{scat}) determined from an exponential decay (i.e., a modified Beer-Lambert equation). Even if a sample is deemed to have low transmission loss and is optically transparent, as determined by simply looking through the sample, the sample can still be unusable as a laser gain media due to the presence of microscopic defects as they relate to the spatial wave front distortion of a laser beam.

1.6   Dissertation Outline

In the case of PLMs specifically, the ability to read the text through the PLM as the primary means to qualifying the transparency and thus its use as a viable laser gain media is incorrect. This methodology does not accurately detect the presence of bulk scattering, gives no information about the distortions introduced when an EM wave travels through the PLM and nor does it show the cumulative effects on the bulk scattering loss present in a representative dimensioned sample due to extended optical path length. The goal of the present dissertation was to develop a more accurate, and time and cost efficient methodologies for characterizing bulk scatter in PLMs. The PLMs used in the study were Erbium (Er) or Neodymium (Nd) doped transparent polycrystalline Y_2O_3, and YAG laser gain media.

Chapter 2 reviews the theoretical background for calculating bulk scattering and how loss due to bulk scattering affects the performance of PLMs. The origin of bulk scatter is explained in terms of discontinuities in the refractive index (dielectric constant) of PLMs. The description and derivation of the extinction coefficient due to bulk scattering, based on the Beer-Lambert law is presented.

Chapter 3 describes the morphology of the PLMs microstructure using optical microscope, Scanning Electron Microscope (SEM), Transmission Electron Microscope (TEM) and Confocal Laser Scanning Microscope (CLSM) to identify the various scattering centers. Samples from different stages of the PLM fabrication sequence are studied. The main purpose is to image and identify features that are the cause of refractive index inhomogeneities, and lead to bulk scattering loss in the PLMs. The measurements are related to optical spectroscopy and lasing characteristics of PLMs and further discussed in Chapters 5.

12

Chapter 4 elaborates on methodology developed in the present effort for characterizing the bulk scattering in the polycrystalline ceramic (specifically applied to Er:Y$_2$O$_3$). The techniques developed include, in-line transmitted laser beam wave-front imaging, angle resolved scatter measurements and Schlieren imaging.

Chapter 5 reports the optical spectroscopy and laser results. The laser performance (threshold and output power) in Er:YAG and Nd:YAG, single crystal and PLM are compared and related to the bulk scatter measurements developed in chapter 4.

Chapter 6 summarizes the dissertation and proposes improvements that could lead to better sensitivity and resolution of the bulk scatter measurements in PLMs. Additional experiments which would lead to improving the fundamental understanding of bulk scattering in PLMs are suggested.

Chapter 2

Theoretical Background

2.1   Lasers

LASER is the acronym for <u>L</u>ight <u>A</u>mplification by <u>S</u>timulated <u>E</u>mission of <u>R</u>adiation [1]. Laser light is very different from most electromagnetic radiation, in that it is highly monochromatic, has temporal and spatial coherence, and is highly directional with relatively low divergence [45, 12].   It can be focused to a small spot, producing flux densities as high as terawatts per cm^2 [3]. Lasers are in essence optical amplifiers. The basic design of a solid-state laser oscillator, shown in Figure 2.1, consists of a gain media located between a resonator that is formed by two mirrors of reflectivity R_1 (~100%) and R_2 (<100%). The emission wavelengths from gain media depend on the active ion (e.g., Er, Nd, Yb, etc) and its concentration in the host material. The cavity mirrors are coated for a specific wavelength or narrow spectral region, matching the emission wavelength of the gain media.

The gain media is excited or pumped by an external source (P_{in}) which leads to a population inversion (N) within the gain media of length (l) as shown schematically in Figure 2.2. The population inversion leads to the initial spontaneous radiation emission from the gain media. The resonator mirrors perform the function of optical feedback with mirror R_1 reflecting virtually all of the (initial spontaneous) optical radiation along the resonator optical axis back and forth between mirrors R_1 and R_2 and across the gain media. Each time the photons pass through the gain media (round trip length = $2l$), they extract more energy from the population inversion via stimulated emission (versus generating more spontaneous emission) [45].
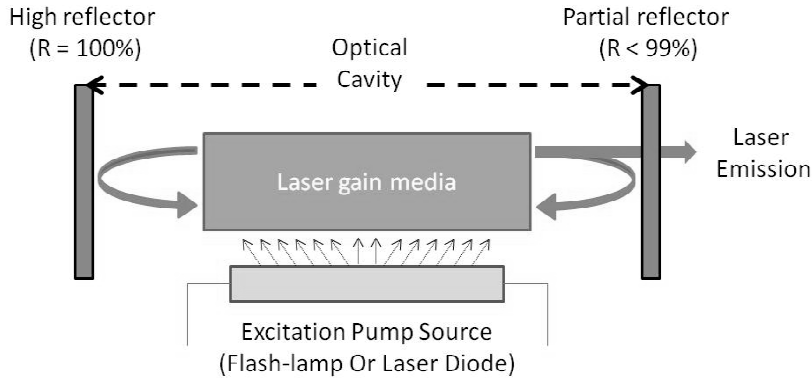
Figure 2.1: The basic design of a solid-state laser oscillator. The cavity is made using two highly reflective mirrors, on either side of the laser gain-media. The gain-media at the center of the optical cavity generates and amplifies light, producing the Laser radiation.
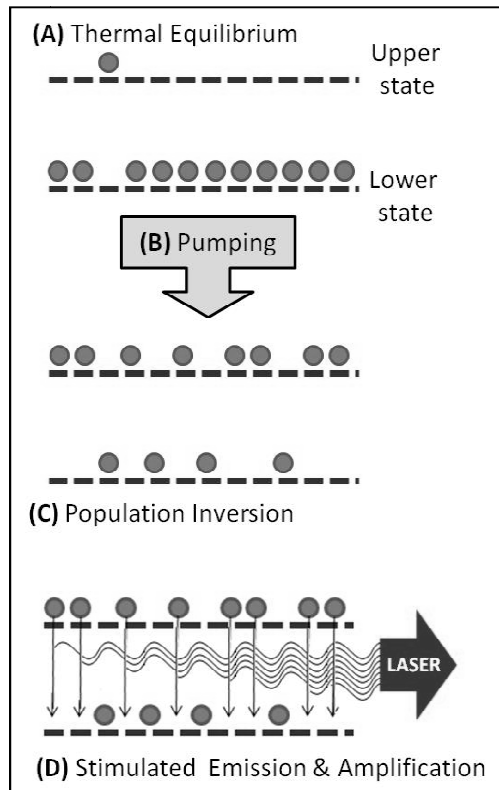
Figure 2.2: Excitation or Pumping creates the 'Population Inversion', in the gain media. The stimulated emission and amplification of light in the laser resonator occurs from this population inversion.

The amplification or the small signal gain 'g' is a product of the population inversion (N) and the stimulated emission cross section (σ_{SE}) [46, 47, 48]. A laser beam is then generated through the output coupler mirror R_2, once the photons are amplified and overcome the combined cavity and material losses. A stable operating point is reached when the round trip gain (G) and the losses are equal,

$$G = R_1.R_2.exp^{(g.(2l))} = 1 \tag{1}$$

In a laser oscillator, a number of loss mechanisms are responsible for attenuating the beam. By combining all the losses proportional to the length of the gain medium, (i.e, absorption and bulk scattering losses) as a single attenuation coefficient δ ($= \alpha_a + \alpha_s$), the threshold condition for oscillation becomes,

$$R_1.R_2.exp^{[(g-\delta).(2l)]} = 1 \tag{2}$$

The small-signal gain (g) depends only on the material parameters and the amount of pump power delivered to the gain material, whereas the saturated gain depends on the power density in the resonator. The saturation intensity (I_s), defines a flux in the gain material when the small-signal gain coefficient is reduced by one-half, and is expressed as:

$$I_s = \frac{h.v}{\sigma_{SE}.\tau_f} \tag{3}$$

The expression for saturated gain is,

$$I = I_s.\left[\frac{2.g_o.L}{\delta - \ln R_2} - 1\right] \tag{4}$$

From the correlative principles, the output power (P_{out}) can be expressed as,

$$P_{out} = A.I.\left(\frac{1-R_2}{1+R_2}\right) \tag{5}$$

The fraction of the intra-cavity power coupled out of the resonator as useful laser output beam is,

$$P_{out} = A.I_s.\left[\frac{2.g_o.L}{\delta - \ln R_2} - 1\right].\left(\frac{1-R_2}{1+R_2}\right) \tag{6}$$

16

where I_s, A, l and R are known quantities and the unsaturated gain coefficient g_0 and the resonator losses δ are extrapolated quantities. For any transparent laser material, the attenuation loss coefficient (δ) of the laser material has a significant impact on the laser performance.

The extinction loss in the material consists of bulk scattering and absorption. The primary limitations to widespread use of polycrystalline laser materials (PLMs), has been the increased loss from bulk-scattering which leads to a reduction of the in-line transmission, and more importantly, to distortion of the laser beam as it propagates through this gain media. The optical distortion (shape and energy distribution) to the oscillating optical field in the resonator cavity is caused by the random spatial variations of the refractive index in the gain media, arising from the presence of microstructure defects.

The fabrication conditions for making the transparent polycrystalline laser gain media and the resulting microstructures have historically been accepted to be the source of bulk-scattering. The spatial phase variations result in random interference patterns of the oscillating optical field leading to degradation of the output beam profile and a reduction in the intra-cavity flux intensity. This reduction of the intra-cavity flux appears as increased cavity losses, quenching the extraction efficiency of the laser and limiting the output power. If the bulk-scattering loss in the gain media is more than the round-trip gain in the laser cavity, it does not have the ability to amplify the photons in the resonator.

The increased loss due to bulk scattering require higher reflectivity output coupler for oscillation, which leads to a increased susceptibility for the coating damage on the resonator mirrors.

2.2   Scattering of Electromagnetic Radiation

Bulk scattering cause the deflection of light rays in random directions due to the presence of inhomogeneities which result in the change in the refractive index (i.e., the dielectric constant) of the material as seen by the EM wave as it propagates through the media [27, 29, 30, 49]. When the frequency of the incoming EM wave is equal to the natural frequency of free vibration of the particles in the material, one observes resonant absorption. As the EM fields oscillate in the wave, the electrons in the material oscillate at the same frequency and thus radiate their own EM wave (emission) that is at the same frequency, but usually with a phase delay [54, 56].

Scattering in matter, occurs at frequencies that do not correspond to the natural frequency of the particles. As they are forced vibrations which do not follow Hooke's law, some of the net energy is radiated in other directions (in case of elastic scattering from molecules the scattering is in random directions) or in some cases even at different frequencies (Raman and Brioulline scattering) [57]. The origin of bulk scattering can be explained using the Maxwell's equations which describe the interaction of matter and EM radiation [50]. In the case a linear, homogeneous and isotropic material, the electric displacement (**D**) is related to the electric field strength (**E**) and the polarization density (**P**) as,

$$\boldsymbol{D} = \varepsilon_o \boldsymbol{E} + \boldsymbol{P} = \varepsilon_o \left(1 + \chi_e\right) \boldsymbol{E} \tag{7}$$

and, the magnetic field strength (**H**) is related to the magnetic flux density (**B**):

$$\boldsymbol{B} = \mu_o \boldsymbol{H} \tag{8}$$

where ε_o and μ_o are is the permittivity and the permeability of free space, and χ_e is the electric susceptibility of the material respectively.

18

The general form of Maxwell's equations express the electric ($\mathbf{E}$) and the magnetic ($\mathbf{B}$) field for an EM wave in terms of the total charge (ρ). For propagation of the EM radiation in free space, the Maxwell's equations can be written as [51, 52]:

$$\nabla . \boldsymbol{E} = \frac{\rho}{\varepsilon_o} \qquad \text{(Gauss's law)} \qquad (9)$$

$$\nabla . \boldsymbol{B} = 0 \qquad \text{(Gauss's law for magnetism)} \qquad (10)$$

$$\nabla \, X \, \boldsymbol{E} = -\frac{\partial \boldsymbol{B}}{\partial t} \qquad \text{(Faraday's law of induction)} \qquad (11)$$

$$\nabla \, X \, \boldsymbol{B} = \mu_o \boldsymbol{J} + \mu_o \varepsilon_o \frac{\partial \boldsymbol{E}}{\partial t} \qquad \text{(Ampere's circuital law)} \qquad (12)$$

In a vacuum and charge free space ($\rho = 0$), equations (9) and (10) reduce to:

$$\nabla . \boldsymbol{E} = 0 \qquad (13)$$

$$\nabla \, X \, \boldsymbol{B} = \mu_o \varepsilon_o \frac{\partial \boldsymbol{E}}{\partial t} \qquad (14)$$

Taking the curl of the equation (11), and using the vector identity, yields

$$\nabla \, X \, (\nabla \, X \, \boldsymbol{E}) = \nabla(\nabla . \boldsymbol{E}) - \nabla^2 \mathbf{E} = -\nabla^2 \mathbf{E} \qquad (15)$$

Substituting equation (14) in (15) gives:

$$\nabla \, X \, (\nabla \, X \, \boldsymbol{E}) = -\frac{\partial}{\partial t}(\nabla \, X \, \mathbf{B}) = -\mu_o \varepsilon_o \frac{\partial^2 \boldsymbol{E}}{\partial t^2} \qquad (16)$$

Since the assumption is made that the environment is charge free space (i.e., $\rho = 0$), combining equations (13) and (10) lead to the general form of the EM wave equation in free space:

$$\nabla^2 E = \mu_o \varepsilon_o \cdot \frac{\partial^2 E}{\partial t^2} = \frac{1}{c_o^2} \cdot \frac{\partial^2 E}{\partial t^2} \tag{17}$$

where, ∇^2 is the Laplace operator, and $c_0 = 2.998 \times 10^8$ m/sec is the speed of light in free space.

The speed of light can also be expressed in terms of the permittivity and the permeability of free space:

$$c_o^2 = \frac{1}{\mu_o \varepsilon_o} \tag{18}$$

In one dimension, the wave equation in reduces to:

$$\frac{\partial^2 E}{\partial x^2} = -\frac{1}{c_o^2} \cdot \frac{\partial^2 E}{\partial t^2} \tag{19}$$

Equation (19) is the one dimensional second-order partial differential equation, which describes the propagation of EM waves through vacuum. The solution of the wave equation is given by,

$$E(x,t) = E_0 \cdot \exp^{+i(kx-\omega t)} \tag{20}$$

where k is wave number and ω is angular frequency. In case of propagation through a media, the general form of the wave equation remains the same as shown in equation (19), with the following modifications:

$$\mu \rightarrow \mu_0 \cdot \mu_r \tag{21}$$

and

$$\varepsilon \rightarrow \varepsilon_0 \cdot \varepsilon_r = (1 + \chi)\varepsilon_r \tag{22}$$

The response of normal materials to external fields is causal, and depends on the frequency of the applied field. When an EM wave travels through a material, its phase velocity is reduced, due to interaction between the electric field component of the EM wave and the electric susceptibility of the medium [53]. The frequency dependence also implies that a material does not respond instantaneously to an applied field, and hence exhibits a phase difference.

The refractive index (n) of a material (in this case, the optical material) describes how light (EM radiation) propagates through that medium. It is defined as the ratio of the velocity of light in a given uniform medium (phase velocity, v) to the velocity of light in vacuum (c), and is denoted by:

$$n = \frac{c}{v} \tag{23}$$

Rearranging, we obtain

$$v = \frac{c}{n} \tag{24}$$

Using equations (14), (21) and (22), we obtain the relation between the refractive index for a material, (n) and the absolute permittivity of the material, as

$$v = \frac{1}{\sqrt{(\varepsilon_0.\varepsilon_r).(\mu_0.\mu_r)}} \tag{25}$$

Hence,

$$n = \sqrt{(\varepsilon_r . \mu_r)} \approx \sqrt{\varepsilon_r} \tag{26}$$

This is because, at optical frequencies, $\mu_r \to 1$ and the refractive index is dependent on the permittivity only. This is in the case of a linear, homogeneous and isotropic material. In case of materials with inhomogeneities, an effective value of dielectric constant is calculated using the Maxwell-Garnett mixing rule. The effective dielectric constant (ε_{eff}) for a material containing two or more spatially separated phases in relatively low ($< 20\%$) volume fractions (f) is given as [55]

$$\varepsilon_{eff} = \varepsilon \left[1 - \frac{3.f.(\varepsilon-1)}{1+2\varepsilon+f(\varepsilon-1)}\right] \tag{27}$$

However, the theory becomes invalid for larger volume fractions, which can be true for the case of pores and voids in PLMs [55].

When a wave propagates from one linear isotropic media to another, the frequency (ν) of the wave and hence its energy (E = hν) does not change, but the wavelength in the medium is reduced, as

$$\lambda = \frac{\lambda_o}{n} \tag{28}$$

where λ_0 is the wavelength in a vacuum.

The Snell–Descartes law (Snell's law) or the law of refraction is used to describe the relationship between the angles of incidence and refraction, when light passes through a boundary between two different isotropic media (Figure 2.3). Snell's law states that the ratio of the phase velocities (v_1, v_2) in the two media is equal to the sine of the angles of incidence (θ_1) and refraction (θ_2), and to the opposite ratio of the indices of refraction (n_1, n_2):

$$\frac{n_2}{n_1} = \frac{v_1}{v_2} = \frac{Sin\,(\theta_1)}{Sin\,(\theta_2)} \tag{29}$$

The Fresnel equations, describe the behavior of light when moving between media of differing refractive indices. For the plane-polarized light, the reflection coefficient is:

$$r_\theta = \frac{n_2\,Cos\,(\theta_1) - n_1\,Cos\,(\theta_2)}{n_2\,Cos\,(\theta_1) + n_1\,Cos\,(\theta_2)} \tag{30}$$

The reflectivity at normal incidence $(\theta = 0)$ is:

$$|r| = r_0 = \frac{n_2 - n_1}{n_2 + n_1} \tag{31}$$

The amplitude reflection coefficient is related to the percent reflectance R (%) by:

$$R\,(\%) = \{\,|r|^2 . 100\,\} \tag{32}$$

And, from the conservation of energy, the percent transmission coefficient T (%) can be determined to be:

$$T\,(\%) = 100 - R\,(\%) = \{\,(1 - |r|^2) . 100\,\} \tag{33}$$
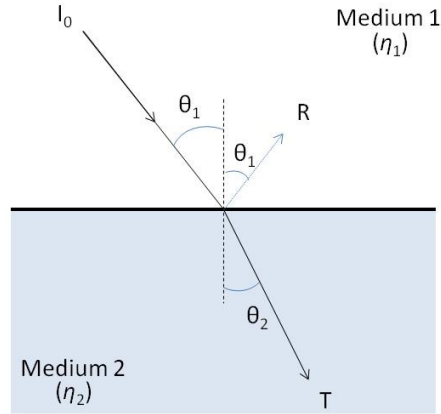
Figure 2.3: Snell's Law of Reflection. I_o is the incident beam on the interface of the two media. The reflected beam is R, where as the transmitted beam is T. The angle of incidence and reflection are the same, where as the angle of refraction depends on the difference in the refractive index of the two media.

The variation of refractive index of materials with wavelength is defined as dispersion. The Sellmeier Equation is used to describe analytically the dispersion of light, for a particular medium. The general form of the Sellmeier equation is:

$$n^2(\lambda) = A + \frac{B_1 \lambda^2}{\lambda^2 - C_1} + \frac{B_2 \lambda^2}{\lambda^2 - C_2} \tag{34}$$

Based on the Kramers–Kronig relations, the refractive index for a given material can be written as a sum of real and complex index of refraction:

$$n = n_R + i n_k \tag{35}$$

The wavelength dependant real part of the refractive index (n_R) relates to the phase-velocity of the wave. The imaginary part of the refractive index (n_k), also referred to as the attenuation coefficient, describes the absorption (or amplification in case of gain) of light by the medium as it propagates through the medium.

23

2.3   Extinction of Electromagnetic Wave in Matter

When a collimated beam of light passes through a substance, assuming the absence of non-linear processes and re-radiation (emission or fluorescence), the beam will lose intensity (extinction). The extinction is due to absorption (conversion of the incident photons to lattice heat or another form of energy) and scattering (change in direction of the propagating photon). The "absorption coefficient" measures loss due to the absorption only, while the "attenuation coefficient" measures the total loss including scattering.

Any quantity that decreases by a fixed percent at regular intervals (distance or time) is said to follow exponential decay and, is represented as,

$$b \cdot e^{-k.x} \tag{36}$$

where b is the initial value before measuring decay, k is the decay rate, and x is the number of intervals.

The "optical depth" or "optical thickness" (τ_λ) expresses the quantity of light removed from a beam by scattering and/or absorption, and is defined as the distance at which the input is reduced by (1/e) or to 36.78 % of input intensity [61, 62]. First proposed in the early 1800s, the Bouguer - Lambert law states that absorption in a material is proportional to the path-length of light [58, 59]. Consider a uniform absorbing sample, divided into thin sections, each of length dx, and perpendicular to the incoming collimated beam of light (Figure 2.4).

The light exiting (I) any of the sections is less intense than the input (I_o) because some of the photons get absorbed and do not exit from the other side. The difference in intensity between

the two is proportional to the length section of absorbing material dx, the light entering the section I_o:

$$\frac{dI}{dx} \propto I_o \tag{37}$$

Rearranging equation (37) yields:

$$dI = -\alpha_{abs} . I_o . dx \tag{38}$$

In equation (38), α_{abs} is the absorption coefficient, and is used to describe how much light is absorbed (hence, the negative sign) through the media. Integrating equation (38) over the total length of the sample leads to:

$$I = I_o . e^{(-\alpha_{abs} . x)} \tag{39}$$

Beer modified the exponential form of the Bouguer-Lambert absorption law wherein the absorption was proportional to the concentration of absorbing species in the material [60].

Let 'A' be the crossection area of a slab of an arbitrary transparent material, with 'N' absorbing particles per unit volume (Figure 2.4). Each particle has a cross section area σ, and is a hypothetical area describing the likelihood of light (or other radiation) being attenuated by it [64].

The effective cross-section σ, is then the sum of the individual cross-sections due to absorption (σ_A), scattering (σ_S) and luminescence (σ_L):

$$\sigma = \sigma_A + \sigma_S + \sigma_L \tag{40}$$

By selecting a particular wavelength region, one can neglect scattering or emission ($\sigma_S = \sigma_L = 0$), and thus only investigate absorption ($\sigma = \sigma_A$). This implies that the particles having an absorption cross section σ, is perpendicular to the path of light through the media such that the

photon of light is absorbed and does not reach the detector if it strikes the particle, or is transmitted (reaches the detector) if it does not.

Let dx be a differential thickness of a section, such that one particle in the slab cannot obscure another, when viewed along the x-direction. The fraction of incident intensity absorbed (dI_x) by this section of volume ($A.dx$) is proportional to the total opaque area, due to the particles given by:

$$\sigma_A \cdot N \cdot (A.dx) \tag{41}$$

Dividing equation (41) by the cross section area (A), gives:

$$\sigma_A \cdot N \cdot (dx) \tag{42}$$

The number of photons absorbed by this section with an effective opaque area (given by equation (42)) is proportional to the total number of photons incident (I_o):

$$dI_x = -\sigma_A \cdot N \cdot I_o \cdot dx \tag{43}$$

As the intensity is reduced passing through the slab, dI_x is negative. The solution to this differential equation is:

$$\ln(I_x) = -\sigma_A \cdot N \cdot x + C \tag{44}$$

For a slab of real thickness 'ℓ', with an input intensity of I_0 (at $z = 0$), and output intensity of I_ℓ (at $z = \ell$), the reduction in intensity across the material is:

$$\ln(I_o) - \ln(I_\ell) = -\sigma_A \cdot N \cdot \ell \tag{45}$$

Rearranging equation (45), yields the familiar exponential form:

$$I = I_o \cdot e^{-\sigma_A \cdot N \cdot \ell} = I_o \cdot e^{-\alpha_A \cdot \ell} \tag{46}$$

Where, α_A ($= N \cdot \sigma_A$) is the absorption coefficient with units of inverse length^{-1}.
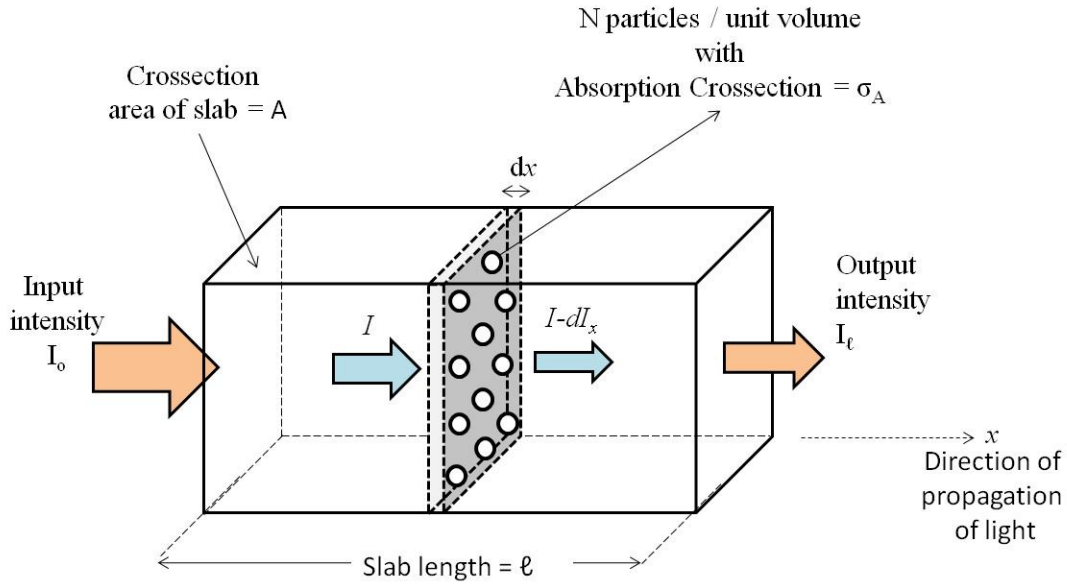
Figure 2.4: Schematic representation of the modified Beer-Lambert law, with absorption as a function of the concentration of absorbing species in the material.

2.4   Limitations of Beer-Lambert Law

The most critical factor of light scattering is the length scale of the scattering centers (the inhomogeneities) in the material, relative to the wavelength (λ) of the light being scattered [26, 49]. There is no simple relationship between the scattering cross-section and the physical size of the particles (d). Most scattering processes are classified into three broad categories, on the basis of this comparison:

     i.   Rayleigh Scattering (d $\ll \lambda$)

    ii.   Mie Scattering (d $\gg \lambda$)

  iii.   Resonance domain or Critical phenomena (d $\sim \lambda$)

Rayleigh scattering is the elastic scattering of light or other electromagnetic radiation, by particles much smaller (d $\ll \lambda$) than the wavelength of the light. It can occur when light travels in transparent solids and liquids, but is most prominently seen in gases [49, 65].

The intensity *I* of light scattered by a single small particle from a beam of unpolarized light of wavelength λ and intensity I_0 is given by,

$$I = I_o \cdot \left(\frac{d}{2}\right)^6 \cdot \left(\frac{\eta^2-1}{\eta^2+2}\right)^2 \cdot \left(\frac{2\pi}{\lambda}\right)^4 \cdot \left(\frac{1+cos^2\theta}{2R^2}\right) \tag{47}$$

where *R* is the distance to the particle, θ is the scattering angle, *n* is the refractive index of the particle, and *d* is the diameter of the particle [26, 27, 49].

The angular distribution of Rayleigh scattering, governed by the $(1 + cos^2\theta)$ term, and is symmetric about the plane normal to the incident direction of the light (i.e., about $\theta = 90°$). Intensity distribution in Rayleigh scattering is symmetric, so the forward scatter equals the backwards scatter. For particles with diameters much larger than the wavelength of light, the Mie scattering approximation is used, the limiting case of which is geometric optics [63].

For Mie scattering, there is no generalized formulation for scattered intensity. In case of large spheres (d >> λ), the anomalous diffraction approximation is used to calculate the scattering efficiency (Q) [49]:

$$Q = 2 - \left(\frac{4}{p}\right)\sin p + \left(\frac{4}{p^2}\right)(1 - \cos p) \tag{48}$$

Where,

$$p = \frac{4\pi a}{\lambda}(n-1) \tag{49}$$

Equation (49) is the phase delay experienced by the wave of wavelength λ, passing through the sphere having a refractive index ratio of 'n' (between inside and outside of the sphere). In the resonance domain, sizes of the particles (the structural variations) inside the material are comparable to the wavelength of light. Elastic light scattering in the resonance domain is still an active area of interest. In this case, the wavelength-sized particles scatter light very efficiently.

Multiple scattering from many particles in close proximity also falls into that domain. In multiple scattering, the scattered field from one particle is influenced by the field from other particles, and the resultant effect must be handled collectively. Critical opalescence is one such phenomenon, usually seen in transparent liquids having density fluctuations around the critical point of phase transition. As the sizes of the particles in the gas and liquid region approach the length scale of the wavelength of light, the light is scattered strongly, causing the normally transparent fluid to appear cloudy or turbid.

Turbidity (or haze) is mostly used for characterizing solid suspensions in liquids, but can also be applied to transparent solids such as glass or plastic [66, 67, 68]. In transparent plastic sheet production, the haze present in the film is defined as the percentage of light that is deflected more than 2.5° from the incoming light direction [69, 70]. The reduction of the intensity of light due to scattering and absorption is used to approximate the scattering coefficient, as an analogous measurement to the absorption coefficient.

In order for Beer's law of absorption to be applicable for a given material, the following conditions need to be satisfied [49]:

1. The absorbers must act independently of each other.

2. The absorbing medium must be homogeneous in the interaction volume.

3. The absorbing medium must not scatter (single or multiple) the radiation.

4. The incident radiation must consist of parallel rays, each traversing the same length in the absorbing medium and preferably be monochromatic.

5. The incident flux must not influence the material by causing optical saturation or pumping, and giving rise to stimulated emission.

29

From these limitations, it can be seen that that the application of the Beer-Lambert exponential equation to explain bulk scattering in polycrystalline transparent ceramics is an over simplistic model. The extinction coefficient is calculated using the Beer-Lambert law, from the reduction of intensity of the incident light through the sample. The reduction in intensity through the sample is measured using a point detector, which does not isolate the process of absorption and scatter. Consequently, most of the reported scattering coefficients in literature are extinction coefficients, which is a combination of both absorption and scatter losses.

The lumped loss, as measured by the Beer-Lambert technique, does not differentiate the mechanism by which the reduction of intensity occurs. Also, the measurements are performed on thin samples (usually < few mm), and the corresponding values of the bulk-scattering coefficient (α_S) obtained, are hence valid for a small optical path length only. In such cases, a large fraction of intensity makes it to the detector, which makes the measured losses due to bulk scattering from the sample appear small. This measurement method does not give any indication of the distortions of the spatial profile of transmitted beam due to the defects and inhomogeneities present in PLMs, which is the true loss due to bulk scattering.

Towards this end, a better methodology is necessary to determine the presence of the inhomogeneities in the PLMs. Even though some PLM samples are optically transparent (qualitatively, as determined by observing the clarity of the black and white target through the bulk), and have a low scattering coefficient, they show poor laser performance and sometimes even fail. Since the scattering is the critical loss mechanism in PLMs, its reduction is especially important for increasing laser performance and leading to high power generation.

Chapter 3

Material Characterization

3.1   Introduction

The overall objective of the present study is to support the need for higher power solid state lasers (P_{out} >10s kW) that has necessitated larger dimension laser gain media. Conventional techniques for fabricating (single crystal) laser gain media via melting raw materials (i.e., Czochralski (CZ)) have reached a limit in terms of the maximum usable portion (fraction) of a boule that can be grown [71, 72, 73]. One solution around this limitation has been to use polycrystalline laser materials (PLMs) which can be fabricated in large dimension and require lower processing temperatures than does the CZ technique.

This ability to process at lower temperature has also led to interest in sesquoxides materials such as Y_2O_3, Sc_2O_3, and Lu_2O_3 due to their higher thermal conductivity relative to oxides such as YAG. Since sesquoxides have a much higher melting point (T_{MP} ~ 2400 ^{o}C), sesquoxides cannot be grown using CZ technique and can only be fabricated using ceramic processing techniques [74]. Single crystal sapphire and synthetic ruby crystals (T_{MP} ~ 2040 ^{o}C) are most commonly fabricated using the CZ technique [128].

While PLMs have been successfully incorporated in high power lasers [75], the reproducibility of PLM fabrication continues to be problematic and there is no reliable, time and cost effective diagnostic technique for analyzing PLMs. The present research attempts to develop a solution to the diagnostic limitation.

Traditionally, a ceramic is defined as an inorganic or nonmetallic solid that is prepared using powdered starting materials and fabricated into desired shapes via a heat treatment [76]. Most ceramics are composed of two or more elements with a complex microstructure. Material properties of the ceramics can often be tailored to the desired application depending on the composition and microstructure. The microstructure of a material is influenced heavily by the fabrication conditions; hence, microstructural characterization is a critical step for optimizing the desired material properties [77, 78].

Materialography, the study of a materials microstructure, provides information about the phase structures (i.e., the phases that exist during sintering and subsequent cooling), grain size, solidification structure, and casting voids in a material [79]. For a polycrystalline ceramic material, the microstructure mainly consists of grains, grain boundaries, secondary phases, pores and voids. Inclusions in a material are classified as either pores (holes) or voids (gaps) depending on their size , for example, a pore is on the scale of < 100 nm, while a gap can be 100s of microns wide [9]. Many macroscopic properties of materials such as hardness, toughness, conductivity, dielectric constant (hence the refractive index since $n = \sqrt{\varepsilon}$) are heavily influenced by the microstructure.

Polycrystalline materials are made up of a large number of single crystals grains (crystallites) separated by grain boundaries, which are generally a few nanometers wide. A grain is a small crystal with a grain boundary, as its growth is impeded by contact with the neighboring grains. In the formation of polycrystalline materials (metals and ceramics), the size of the crystalline grains is determined largely by the size of the crystalline particles present in the starting powders. Moreover, the size of pores, voids and the grain boundaries scales proportional with the grain size.

32

Both pores and voids refer to structural defect, i.e. the absence of material. Pores are generally much smaller than the grains, and can be present both, at the grain-boundaries and inside the grains, whereas voids are larger with sizes similar to the grains. Porosity is commonly observed in metals and ceramics, and is referred to as the micro-holes in the material resulting from the sintering of powders. Voids, on the other hand, are generally much larger, and result from trapped air in the green body.

The pores and voids present in the bulk of the ceramic create a change in the refractive index for the EM wave travelling through the material (the average value of the refractive index of Y_2O_3 is 1.89 and that of air (at NTP) is 1.004, in the wavelength region spanning from 400 nm – 3200 nm). The inhomogeneity in the refractive index (i.e. discontinuity in the dielectric constant) is regarded as the basis of the bulk scattering loss in the ceramic samples.

Even though the overall basic method for fabricating transparent ceramics is the same, there are many variations of for each step. For the present study, a low temperature process using a modification of powder metallurgy is used for the fabrication of transparent ceramic Y_2O_3. The resulting polycrystalline ceramic, depending on the fabrication conditions, consists of grains (ranging from microns to hundreds of microns) and grain boundaries that separate the grains. If the grains and grain boundaries are clean (i.e. free from impurities, inclusions, voids and pores) then the transmission through the ceramic can approach the theoretical maximum, i.e., there are no discontinuities in the dielectric constant.

The fabrication begins with the creation of the starting powders using either sol-gel, solution synthesis or hydrothermal processing [80]. There are two scalable fabrication approaches used for fabricating PLMs by the compaction of the precursor powders [74]. The

first process relies on hot pressing of the powders (< 100 nm particle size) at high pressures (~5,000 psi or 34.47 MPa) and elevated temperatures (~ 2000 ^{o}C) in a graphite furnace. This forms a ceramic body with a > 90 % of the theoretical density.

Under the applied pressure, there is a small deformation of the grains, but there is a considerable reduction in the porosity between the grains. Only the outer surfaces of the adjoining grains fuse, creating porous scaffolding like structure where the gaps filled with gas (air) or are empty. The final step uses Hot Isostatic Pressing (HIP) with an argon gas pressure (~30,000 psi or 206.82 MPa) and high temperature collapses any residual pores to attempt to achieve full density and transparency.

The second, and more commonly used, approach involves cold forming of powders (> 1 µm particle size) with added binders to aid in densification. Cold forming techniques such as Cold Isostatic Pressing (CIP), slip casting, tape casting, extrusion are used to make a low-density (40 - 60% of full density) green body. The green body is further vacuum sintered at elevated temperatures to achieve > 95 % of full density. Finally, the green body is subjected to HIP to achieve full density and transparency. In theory, both approaches should yield fully densified and transparency samples. However, such is not the case and the samples require further annealing.

Sintering is a controlled, scalable and cheaper process for the densification at elevated temperatures, leading to lower porosity in the final ceramic sample. Sintering is the process of bonding powders (solid particles) into a monolithic structure as a result of the particles being compacted into an approximate final shape. Densification via sintering is achieved by slowly heating the green body to ~ 80 % of the melting point, and holding the green body at elevated

temperatures for an extended duration (soaking). The driving force for sintering is the high surface energy of the fine powders, which is lowered by volume (densification) and surface diffusion causing the particles to change their shape and increasing their contact area. The inter-particle spacing or the porosity decreases from the movement of the pores/voids to free surfaces. The elimination of pores from the bulk leads to volume reduction which results in increased densification.

3.2   Methodology

In the previous chapter, an argument was made that microstructure is the origin of the refractive index inhomogeneities that leads to bulk scatter which ultimately results in the in-line transmission loss. As the formation of scattering centers is dependent on the fabrication method used, this chapter details the multiple imaging techniques utilized to understand the evolution of microstructures that are present in during the different stages of the fabrication process. Since the primary motivation for this study was understanding the fundamental material related issue of bulk scattering which limit the use of PLMs in high power lasers, standard material science imaging techniques were used for characterization and a correlation was made with the optical spectroscopic analysis.

Imaging techniques used to study the different stages of fabrication sequence include, optical microscopy, Scanning Electron Microscopy (SEM), Transmission Electron Microscopy (TEM) and Confocal Laser-Light Scanning Microscopy (CLSM). The different stages of Er:Y_2O_3 fabrication process that were investigated include the starting powders, green body and the transparent ceramics. The spectroscopic characteristics (specifically the upper-state radiative fluorescent lifetime), and the grain size measurements (determined using XRD) of the precursor powders were investigated as a function of the calcination temperatures.

The green body, formed from pressing the starting powders, is an intermediate step in the fabrication sequence, and requires additional processing steps for transformation into the transparent PLM. The microstructure of green body and fully dense transparent PLM (after HIP) was imaged. The comparison of the images at the two stages highlights the microstructural differences that result in significant differences in transparency. Finally, the source of inhomogeneities of the refractive index in the transparent PLM which leads to bulk scattering is determined using CLSM.

3.3 Characterization of the Starting Powders

Fabrication of transparent ceramics begins with the formation of the precursors or the 'starting powders' using chemical synthesis. Before the starting powders are compacted, the powders are calcined. Calcination is a thermal treatment, usually in the presence of flowing dry and hot air, performed on ores and other solid materials to bring about a thermal decomposition and removal of residual volatile fractions and water. The calcination temperature significantly affects the microstructure and transparency of the final ceramics [79]. In the present study, six different calcined precursor powder samples were evaluated, whose fabrication is detailed in reference [80].

The samples (H1 - H6) were sequentially extracted from a single batch of 0.5% Er:Y_2O_3 starting powder being calcined in flowing air from room temperature to a maximum of 1100 °C which was limited by the equipment [80]. The powders are identified using their respective calcination temperature at which they were extracted from the batch, as: H1 (25 °C), H2 (600 °C), H3 (800 °C), H4 (1000 °C), H5 (1050 °C) and H6 (1100 °C, annealed for 6 hours). Only sample H6 was heated at a constant temperature (annealing) of 1100 °C for 6 hours.

3.4 Radiative Lifetime

To correlate changes in the starting powder in response to the calcination temperature with spectroscopic characteristics of the powder (as relevant to the PLM usability in a laser), the upper state radiative lifetime of 0.5% Er:Y_2O_3 is used as a metric. The upper state radiative lifetime is one of the indicators used in evaluating a gain media's potential as a useful laser material. Ideally, a long upper state radiative lifetime (100s µs to few ms) is desirable.

The calcination process causes the removal of water and hydrocarbons from the powders, and leads to the formation of optically active Er^{3+} in the 0.5% Er:Y_2O_3 powders. For mid-IR operation, the upper state in Er:Y_2O_3 corresponds to the $^4I_{11/2} \rightarrow {}^4I_{15/2}$ transition. Having a measurable lifetime for this transition is indicative of the creation of the optically active Er^{3+} as the powder is heated.
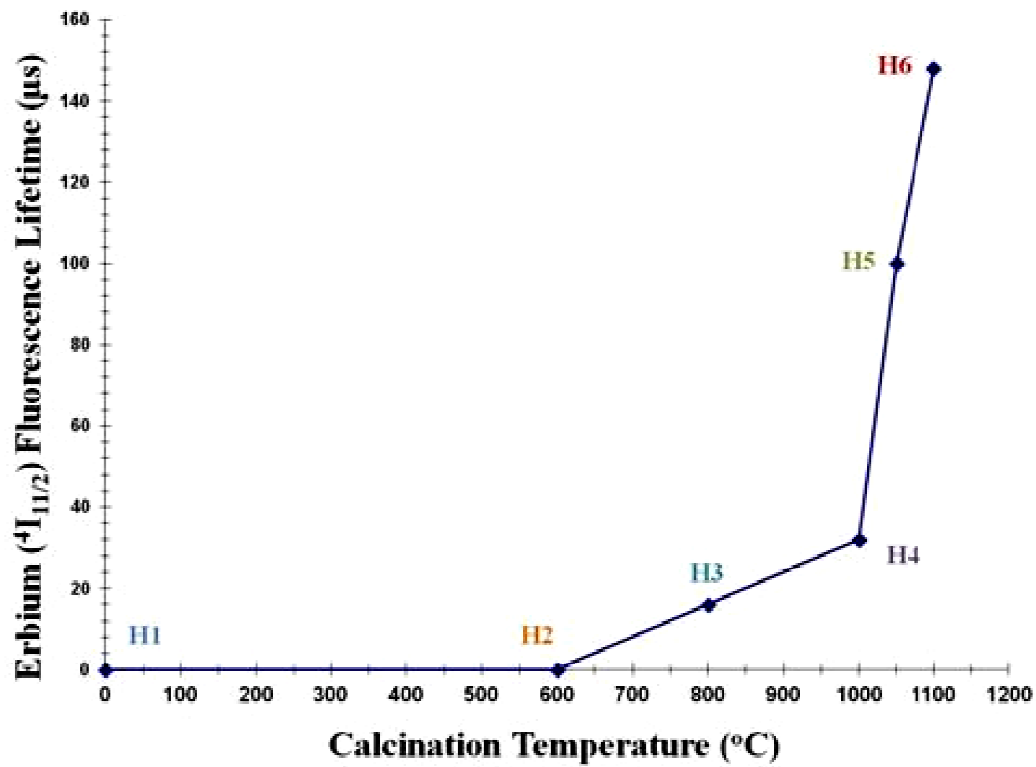
Figure 3.1: Variation in upper state fluorescence lifetime (radiative decay from $^4I_{11/2} \rightarrow {}^4I_{15/2}$, emission $\lambda \sim 1$ µm), as a function of calcination temperature for 0.5% Er:Y_2O_3 starting powders (H1 – H6).

The upper state radiative lifetime increased as the calcination temperature of the powders increased (Figure 3.1). The maximum radiative lifetime and the highest yield were observed for the calcined powder sample H6. The upper state radiative lifetime of the final sintered ceramic sample, made from the H6 powder, was much longer at 1200 µsec, indicating the large scale formation of optically active Er^{3+} in the Y_2O_3 host from sintering at higher temperature. This indicates that the final ceramic formed using the calcined powders has negligible amounts of water and hydrocarbon impurities inside the bulk, which are generally accepted as a one of the major sources of lifetime quenching and attenuation of the fluorescence signal.

3.5   XRD Analysis

Double axis HRXRD (High Resolution X-Ray Diffraction) powder scans were performed on all six samples (Figure 3.2). A Bede D1 high-resolution diffractometer setup with a sealed copper anode X-ray source equipped with a Maxflux™ specular mirror, for collimation. A Si (220) Dual Channel Analyzer (DCA) crystal (two or four bounce) was used to select the Cu $K\alpha_1$ radiation ($\lambda_{K\alpha_1}$ = 0.1540562 nm) from the X-ray source. The 2θ - ω scan used a step size of 0.005° and count time of 3 seconds. The diffractometer setup made it possible to resolve peaks and measure particle sizes up to a micron. The X-ray diffraction pattern of the (un-calcined) precursor precipitates sample H1, formed at room temperature matches the $Y_2(OH)_5(NO)_{0.9}$ phase, with small peaks, at 2θ values of 19.5, 26, 27, 50 and 52 degrees [82, 83]. As the calcination temperature is increased, the formation of Y_2O_3 crystallites from the yttrium nitrate precursor (H1) is observed [84]. With the increasing calcination temperature (to ~ 600 ^{o}C), the decomposition of the $Y_2(OH)_5(NO)_{0.9}$ phase occurs, and results in most of the peaks vanishing and the formation of a new peak at 2θ = 29.03 degrees, as evident in sample H2.

Upon further heating, the powder scans of samples H3 to H6 showed the formation of crystallites as evident from the decreasing peak widths and increasing peak heights. At 800 ^{o}C temperature, the calcined sample H3 shows prominent but very broad peaks, which matches the Y_2O_3 phase. As the calcination temperature is further increased to 1100 ^{o}C, the Full Width at Half Maximum (FWHM), of the peaks become narrower. Sample H6 has the smallest FWHM as show in Figure 3.3. In x-ray diffraction, a shape factor is used to correlate the size of sub-micron particles or crystallites, to the peak broadening (FWHM) in a diffraction pattern. The Scherrer equation is used to estimate the crystallite size, and is limited to nano-scale particles (< 100 nm) [81]
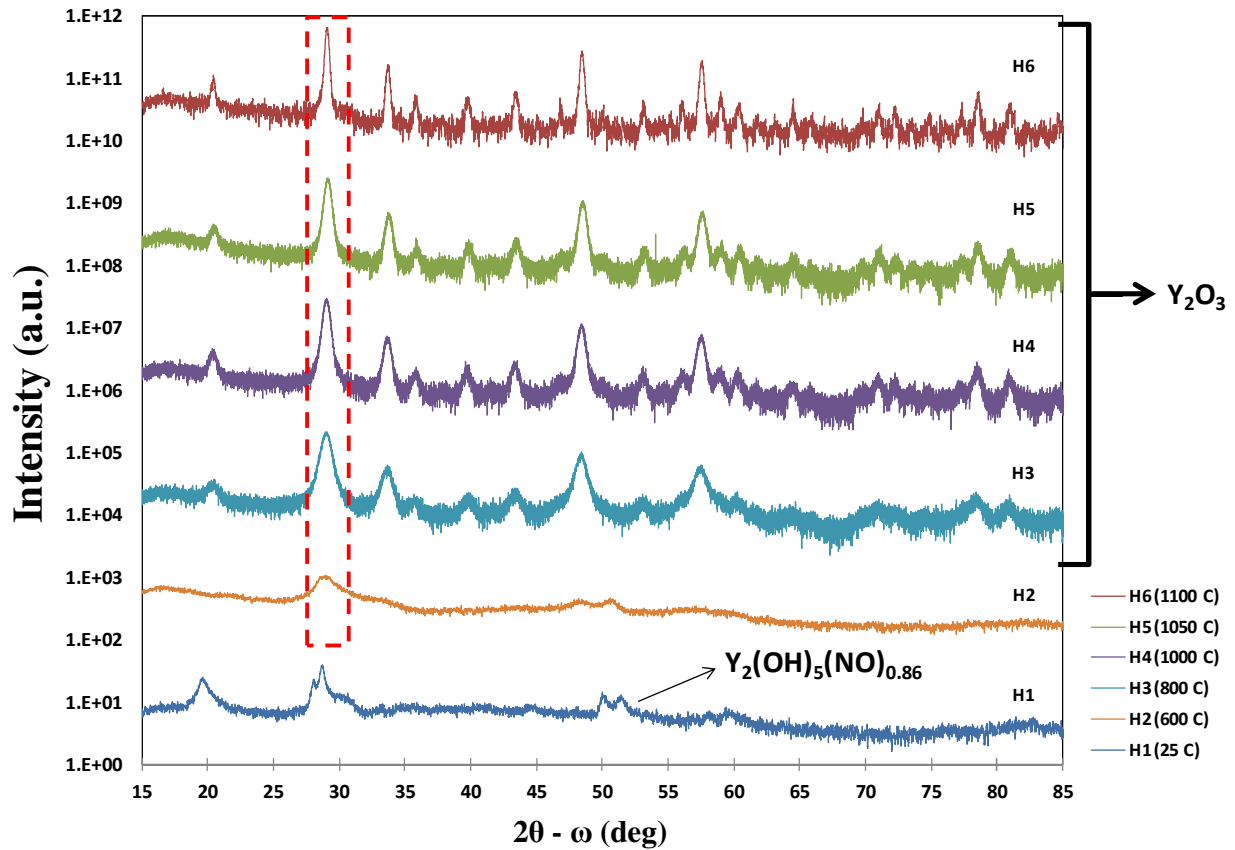
Figure 3.2: 2θ-ω scans for the six calcined powders (0.5% Er:Y_2O_3). Crystallite formation as a function of calcination temperature of the starting powders.

Table 1: Measured FWHM from the diffraction pattern, and calculated particle size using the Scherrer equation.

Sample	Temperature (^{o}C)	Diffraction Angle (2θ)	FWHM (deg)	FWHM (arcsec)	Integral Breadth (β)	Particle Size (nm)
H6	1100	29.04	0.29	1054	0.32	31.06
H5	1050	29.11	0.53	1907	0.56	17.18
H4	1000	29.03	0.55	1985	0.59	16.5
H3	800	29.03	0.80	2892	0.86	11.33
H2	600	28.74	1.77	6386	1.89	5.12
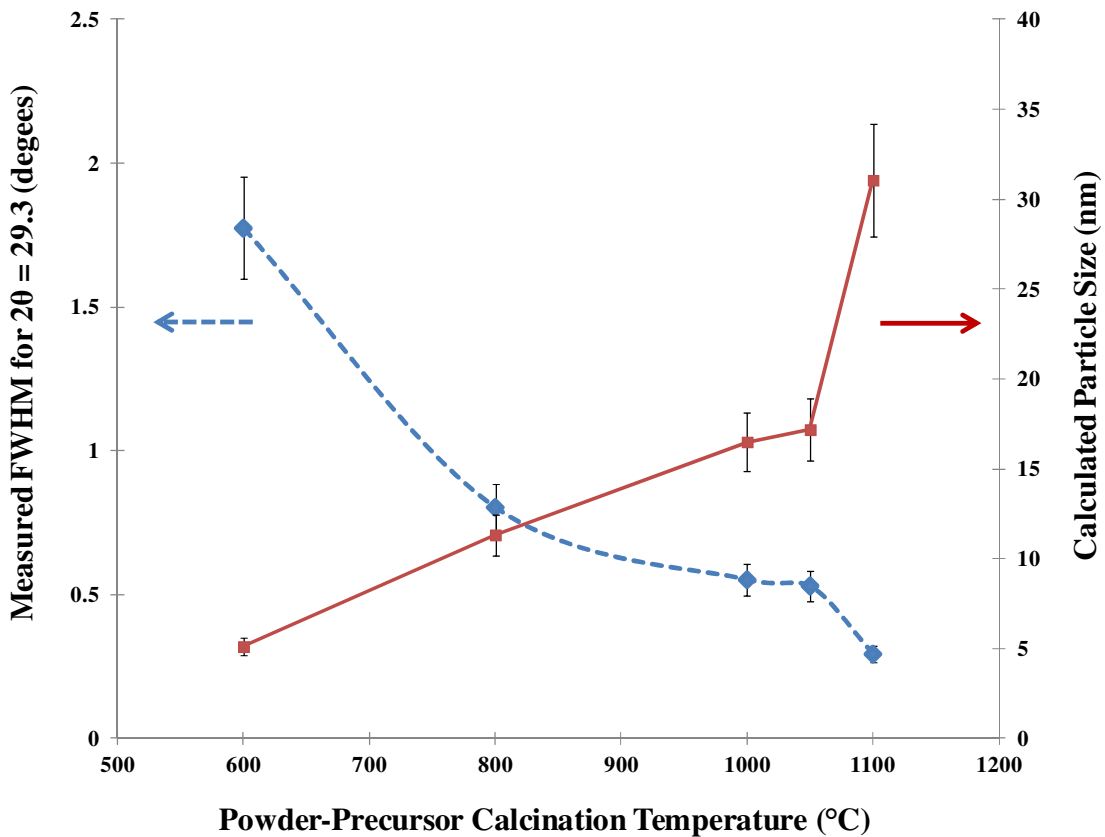
Figure 3.3: (a) Variation in the FWHM at $2\theta = 29.03^{o}$, for 0.5% Er:Y$_2$O$_3$ starting powders (H2 – H6) as a function of calcination temperature. (b) The calculated crystallite size, using the Scherrer equation, at $2\theta = 29.03^{o}$, for the 0.5% Er:Y$_2$O$_3$ starting powders (H2 – H6), as a function of calcination temperature.
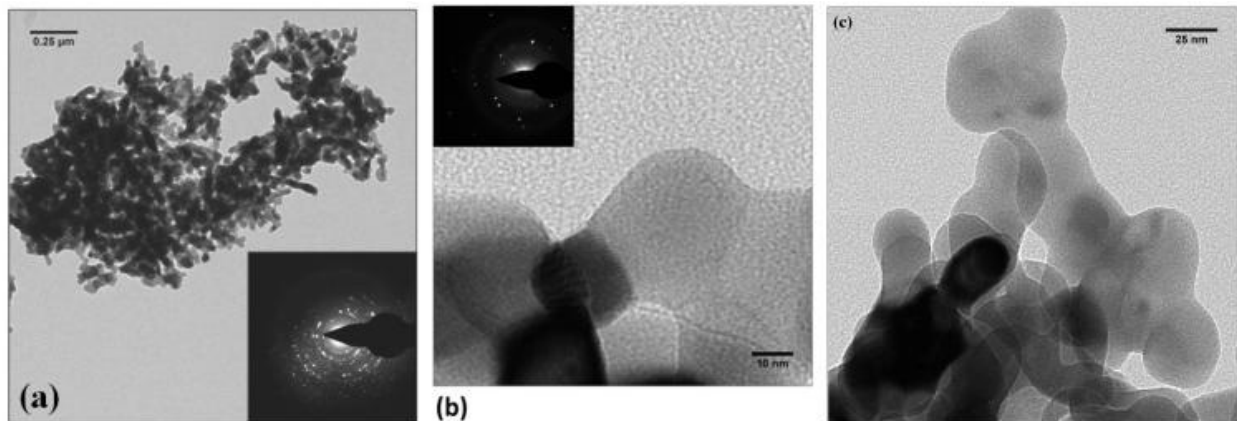
Figure 3.4: (a) HR-TEM images of 0.5% Er:Y_2O_3 powders (sample H6) calcined at 1100°C. Inset is diffraction pattern (b) Micro diffraction confirms the single crystal nature of the individual grains (c) average grain size is between 25 nm to 35 nm.

The crystallite size is a measure of the size of a coherently diffracting domain, and is not necessarily the same as the particle size [81]. A variety of factors contribute to the width of a diffraction peak, like crystallite size, inhomogeneous strain and instrumental effects. Figure 3.3 shows the change in the calculated crystallite size (Table 1) of the powders determined using the FWHM of the 2θ peak, as a function of calcinations temperature.

The powder sample H6 was determined to have a crystallite size of 31 nm. Figure 3.4 shows the TEM images of the Yttria powder sample H6, which was calcined at 1100 ^{o}C for 6 hours. The images show that the particles are spherical in shape, and the individual particle sizes range between 25 - 35 nm. These particle size measurements are very similar to the domain sizes calculated from the diffraction pattern. The single crystal nature of the particles is also confirmed from micro diffraction. The increase in lifetime corresponds to the increase in the particle size (grain growth and coarsening).

3.6   Characterization of Green Body

The green body is an intermediate step in the fabrication sequence formed from pressing (CIP or hot press) the starting powders. The green body used in this study was formed from cold pressing and using micron size undoped Y_2O_3 calcined powders.

An FEI Nova™ NanoSEM environmental SEM (or variable pressure, VP-SEM) allowed imaging of the bare insulating surface of the green body, without a need to deposit a conductive (gold) coating to mitigate charging artifacts.

Visually, the green body was opaque and white in color. For SEM imaging, the green body sample was fractured by applying shearing force to expose the internal structure. Fracturing allowed for the imaging of the internal structure of the ceramics without any alterations introduced from the process of cutting, sectioning and polishing.

Figure 3.5 shows that the non-transparent ceramic has a scaffolding-like structure, with a large number of voids present between the grains. The approximate size of the grains was 1 - 3 µm, and the dimensions of the voids between the grains were in the range of 400 nm – 600 nm.

The dimension of the voids being within the visible region of the EM spectrum (350 nm $< \lambda < 750$ nm) explains the whitish color of the green body. Hence, the green body scatters visible light efficiently and has a white appearance.
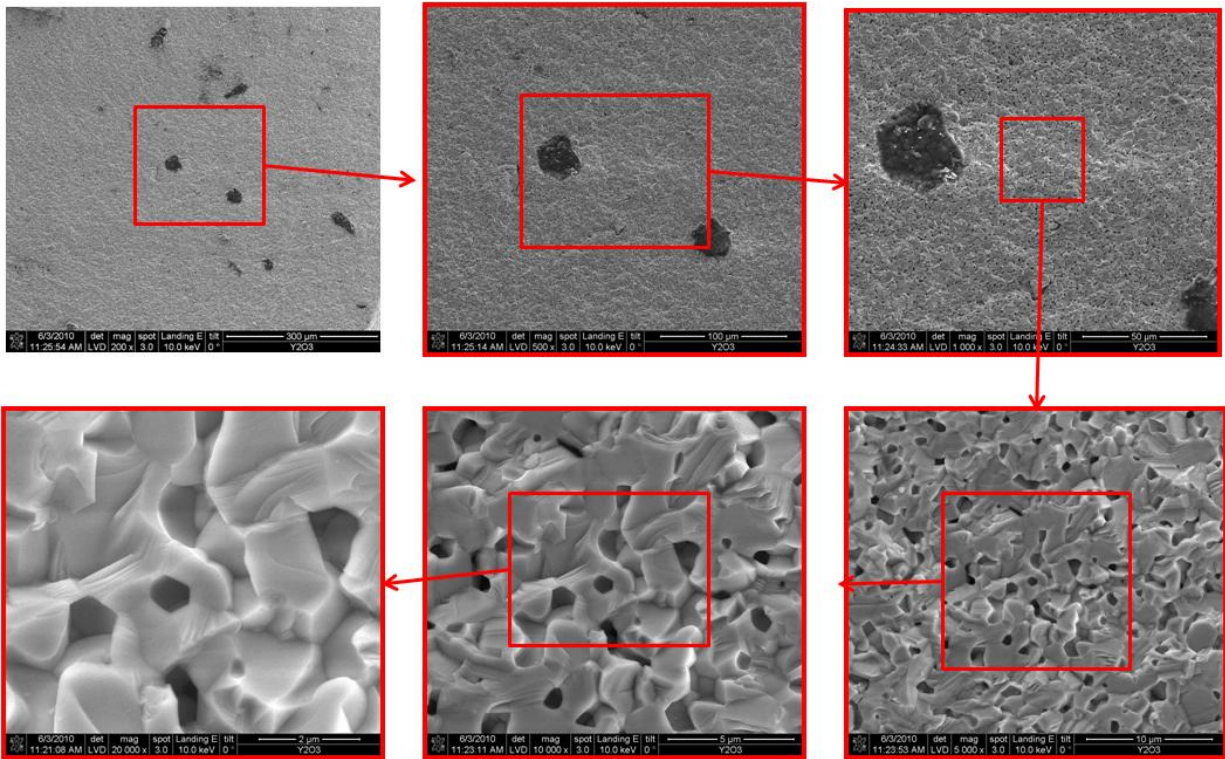
Figure 3.5: VP-SEM image of the fractured surface of an opaque polycrystalline Y$_2$O$_3$ ceramic before hipping, with loosely packed grains and visible porosity (size of voids ~ 500 nm).

3.7   Characterization of Transparent PLM

An additional processing step of HIP is required for transformation of the green body into the transparent PLM. The HIP treatment used argon gas pressure (~ 30,000 psi) and high temperature (> 2000 °C) to remove any porosity between the grains, resulting in a fully densified transparent ceramic.   The transparent sample characterized in this section, was formed by subjecting an opaque green body (similar to the one mentioned in the section 3.4) to HIP process.
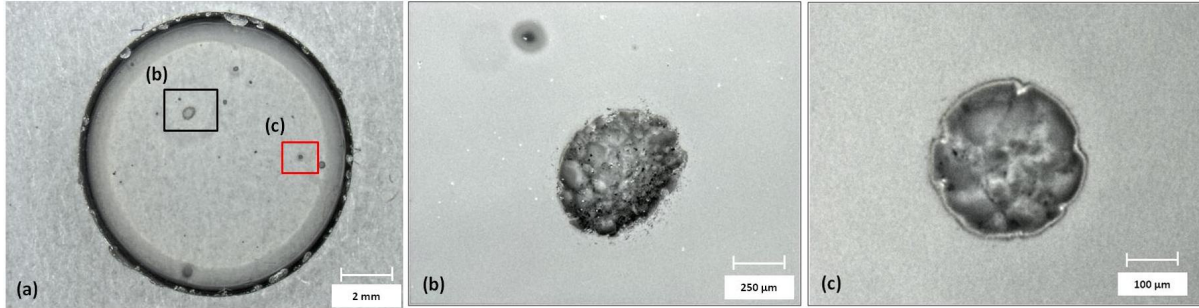
Figure 3.6: Optical images of (a) inclusions in the bulk of the ceramic sample. (b) close up of large size inclusion (~ 500 μm diameter) in the bulk of the ceramic sample (c) small size inclusion (~ 200 μm diameter)

The sample was visually transparent to the naked eye, and it was possible to image (read) through the sample by placing it on a pattern (or text). However, large defects (~ 500 μm in diameter) are visible in the bulk of the sample when held in front of a bright light source. An optical microscope (Keyence Model VHX 1000), with a 200x optical zoom lens, and a 30 mega-pixel digital camera was used for imaging the large defects trapped within the bulk of the undoped Y_2O_3 sample (Figure 3.6 (b)).

The transparent ceramics showed the presence of few large circular and oval shaped defects distributed randomly in the bulk. The size of the defects varied from 50 μm - 500 μm. The presence of these large dimension voids in the green body, left behind during the compaction of the starting powders, is the most likely cause of the defects in the sintered ceramics. The areas around the large defects show the presence of large inhomogeneities in refractive index, which are evident from the transmitted wavefront distortion and Schlieren images, discussed in the next chapter.

The microstructure of the transparent sample was also analyzed using the VP SEM to identify the changes relative to the green body (Figure 3.5). The fractured section of the transparent ceramic showed dense packed grains, with grain size in the 1 - 3 µm range, as was the case of the green body, no voids (gaps) were visible between the grains in the transparent sample. The fractured surface of the grains appears featureless and uniform. This indicates the absence of porosity within the bulk of the individual grains.
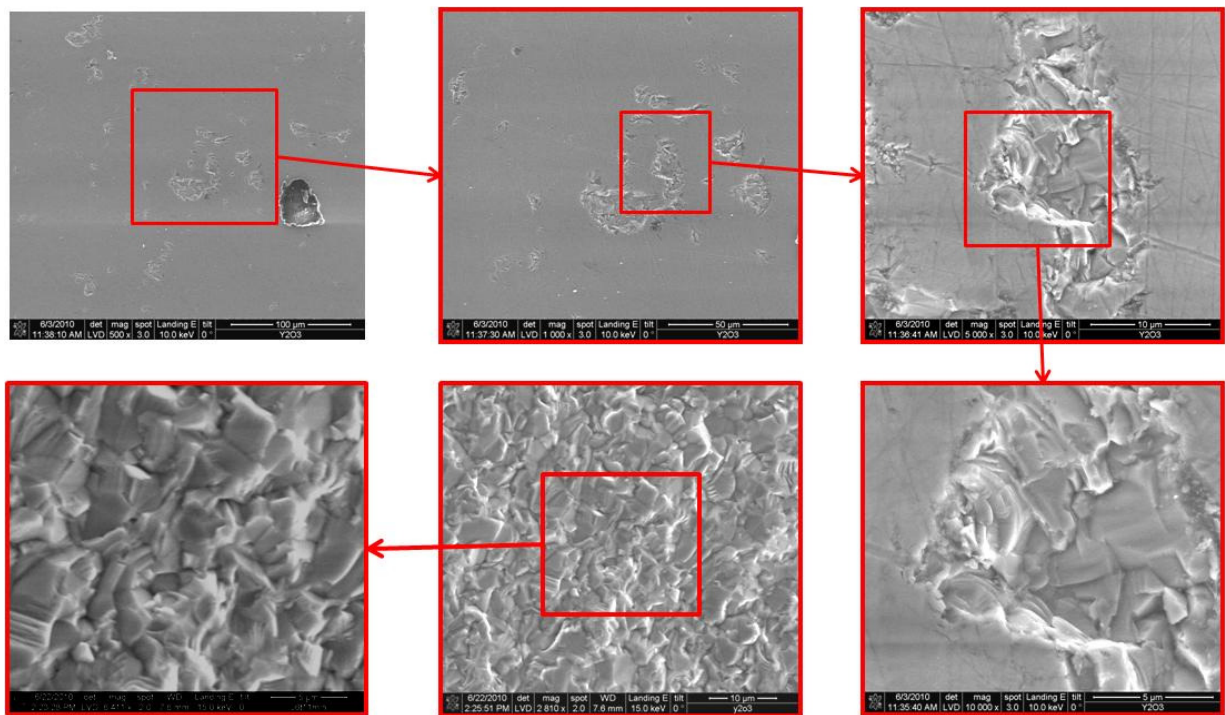
Figure 3.7: VP-SEM image of the fractured surface of a transparent Polycrystalline Y_2O_3 ceramic obtained after the HIP process, with dense packed grains and no visibly porosity.

A Confocal Light Scanning Microscope (CLSM) was used to obtain high-resolution in-focus optical images with depth selectivity, within the transparent samples to reveal the internal structures. The process is very similar to tomography [85]. The CLSM was used to image the variations in the refractive index of the material inside the grain and at the grain boundaries for

the transparent PLM sample. A Leica SP5 MP-STED Confocal microscope was used to image the fractured surface of the transparent ceramic.

The system had multiple laser sources, at different wavelengths (λ = 405, 532, and 632.8 nm) available for scanning a wide variety of materials. In order to obtain the highest resolution, the shortest wavelength (405 nm) source combined with a high numerical aperture (N.A. > 0.95) immersion objective lens was utilized. The immersion fluid used in this case was high purity DI (De-Ionized) water. The sample was intentionally fractured, and a small fractured specimen broken from the transparent sample was imaged using the CLSM in reflectivity mode.

The fractured surface of the polycrystalline ceramic was viewed to identify a flat area on the fractured surface showing the grain boundary between three grains was selected. The sample surface is denoted as the X-Y plane, and the direction going into the bulk of the sample is the Z axis. By changing the microscopes depth of focus, 2-D images (in X-Y plane) at different (Z axis values) depth inside the sample were taken. The scanning laser beam was focused on the sample surface through the high NA objective lens, and viewed using the camera attached to the microscope assembly to obtain the surface image of the sample.

The CLSM was used in reflection mode, to image the variations in the refractive index of the material inside the grain and at the grain boundaries. The 2-D mages are made from raster scanning the laser beam, similar to a SEM, and point by point recording the reflected intensity on the detector. Figure 3.8 shows the stereographic 3-D CLSM image (view using red filter on left, and blue filter on right) in the reflection mode at the triple junction between the three grains.
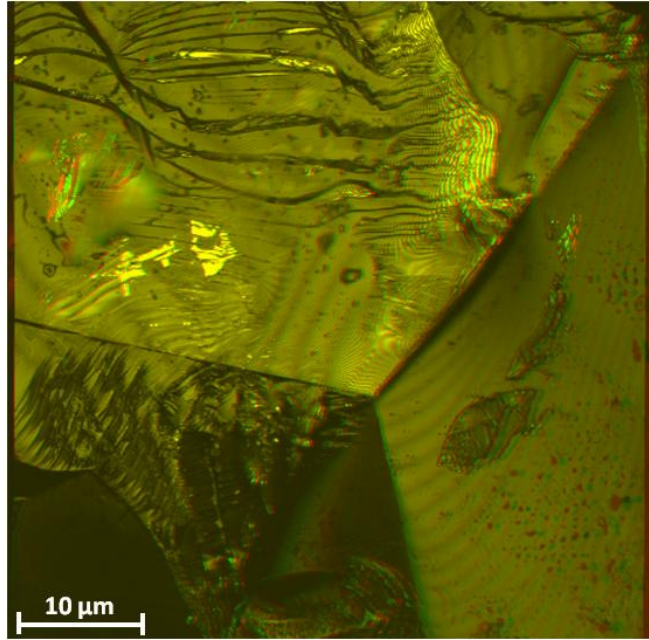
Figure 3.8: False color (Red (Left field)-Green (Right field)) Stereographic 3D
CLSM Image (reflection mode).
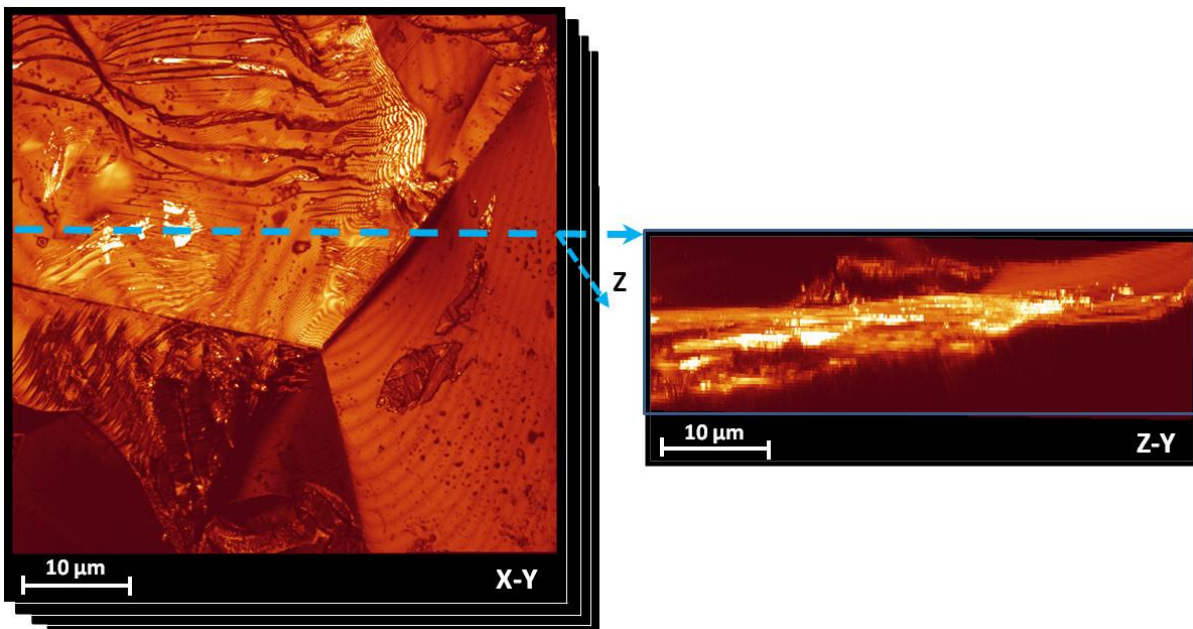
Figure 3.9: (a) Z-Axis Extrapolation of the grain boundary, reconstructed from the 48
slices taken by moving the depth of focus in steps of 200 nm into the bulk
of the sample. (b) Bright areas in the image show the grain boundary,
which represents a different refractive index than the surrounding bulk.

The bright areas in the 2-D images are due to higher reflected intensity, compared to the neighboring areas as measured by the detector. This corresponds to areas on the sample having a difference in refractive index (discontinuity in the dielectric constant) which causes a higher intensity value due to reflection. For imaging the subsurface structure of the grains and the grain-boundary interface, the depth of focus of the scanning laser beam was changed.

To obtain the depth profile, 48 images were taken each at 200 nm depth. All image slices were taken parallel to the surface (X-Y plane), going through a total distance of 10 μm into the bulk (along the Z-axis). From the 48 images, a slice in the Z-Y plane, located at the dashed blue line on the X-Y plane in Figure 3.9 (a), was reconstructed. In this reconstructed image, the bright areas reflecting more light than the surrounding bulk are below the surface and create a surface (Figure 3.9 (b)).

This surface lies between two regions of uniform contrast belonging to the grain on top and the underlying grain. This clearly suggests that the surface corresponds to the grain boundary region, and indicates that this region has a different refractive index than the surrounding grains. This leads us to speculate that the grain boundary region with a slightly lower (< 5 %) refractive index, and is the source of bulk scattering in the sample.

3.8   Conclusions

The main objective of this chapter was to understand and identify the sources of refractive index inhomogeneities that lead to bulk scattering. Samples from various stages of the fabrication sequence of the PLM were characterized in terms of their microstructure and spectroscopic properties. The upper state fluorescence lifetimes of the starting powders was

shown to increase with the increasing calcination temperature. This trend was related to the grain / crystallite size of the powders as a function of calcination temperature.

The crystallite size was calculated using the Scherrer equation using the FWHM values from powder diffraction pattern measurements (Figure 3.3). The calculated particle size was confirmed using HR-TEM to be around 30 nm (Figure 3.4). In terms of the differences in the microstructure of the green body and the transparent ceramic obtained after HIP, the green body had a porous microstructure with 300 nm to 500 nm sized voids between the grains and hence looked opaque.

In case of the transparent ceramic, formed after the HIP treatment of the green body, the microstructure showed close packed grains, with no large voids between the grains. Few large dimension inclusions (defects) were present within the transparent ceramic body, which might otherwise have been created during the packing of the powders to make the green body.

CLSM was used to create tomography images of the microstructure of the transparent ceramic sample by a process of depth sectioning. The tomography images were used to identify the regions that appeared brighter (due to higher reflectivity) in the sample both in the grains and around the grain boundaries. The regions around the grain boundaries showed the highest reflected intensity, indicating a different refractive index (a discontinuity of the dielectric constant) from the rest of the surrounding region (grain). This suggests that grain boundaries are the primary cause of refractive index variations, and hence cause bulk scattering in the transparent ceramic sample.

Chapter 4

Optical Characterization

From a laser system engineering perspective, laser gain media need to have certain spectroscopic characteristics (i.e., absorption and emission spectra at desired wavelengths, favorable fluorescence lifetimes, gain (higher the better)), opto-mechnical properties, thermo-optic properties (i.e., thermal expansion coefficient (lower the better)), and optical properties, (low scatter, uniform refractive index, and high transparency at the desired wavelengths). In terms of solid state lasers, the laser gain media have either been single crystal oxides (i.e., YAG, YSGG, GGG), fluorides, or glasses doped with active ions (e.g., Nd, Er, Yb, etc). The demonstration of the very first laser action in 0.9% Nd:YAG polycrystalline ceramic laser gain media in 1995 redefined laser gain material development and brought into focus the field of fabrication of the polycrystalline laser material (PLM) or ceramic laser media [19].

It is generally accepted in the laser community that single crystal and (good quality) polycrystalline laser materials are identical in every respect except how they are made (CZ growth or polycrystalline fabrication). Even today, the general method of determining the quality of PLM is: (1) fabrication of small scale sample to check for proper stoichiometric ratio of starting powders, (2) polish a sample to inspection quality (sufficient to obtain an absorption spectra and evaluate for presence of defects (pores and inclusions), (3) if the absorption spectra is acceptable and there are no defects present, repeat first two steps for fabrication to desired dimension, (4) polish larger sized sample to laser quality (suitable for making scattering measurements), and (5) use sample in a laser set-up to test for laser performance (i.e., evaluate P_{out} vs. P_{in} curve and compare with theoretical limits).

As far as processing time are concerned, the above mentioned steps can take anywhere from 7 to 11 weeks. Looking more closely, steps 1 and 2 take approximately 3 - 4 weeks (minimum 6 weeks if using CZ growth); steps 3 and 4 can take 2 - 4 weeks or 1 - 3 weeks, respectively, depending on the desired sample dimension; and step 5 if performed thoroughly, takes at least 1 week. Often, even if the stoichiometry is deemed acceptable and larger dimensioned samples are prepared, the PLM, while (qualitatively) transparent, does not yield lasing action. Clearly, a better diagnostic methodology for assessing the quality of PLMs is needed (even if the analysis technique yields qualitative information).

Optical transparency, especially in the case of polycrystalline laser materials (PLMs), is one of (if not) the most often used to determine the quality of optical and laser materials. The methodology of determining the bulk scatter in polycrystalline materials in the literature is inconsistent and sometimes vague. One metric used to quantify optical transparency is bulk scattering (designated as a scattering coefficient) with the goal being to achieve the lowest possible bulk scattering. The most important aspect for qualifying PLMs is the optical quality of the materials as measured by the loss of energy of an electromagnetic (EM) wave as it propagates through the PLM. The loss of energy is due to bulk scattering caused by the inclusion of scattering centers.

The requirements for transparency for polycrystalline ceramics used in applications such as lighting, transparent armor for vehicles, domes and windows on missiles (typically in the mid-IR 3 - 7 µm spectral range) are much more relaxed than the transparency requirements for PLMs [86]. Often the transparency is determined by simply being able to "look" through the material (even in the mid-IR spectrum with an IR camera) [35]. Sometimes a single point measurement is performed by collecting all the scattered light and comparing to the net transmission. Virtually

51

every research or commercial entity attempting to fabricate transparent PLMs also utilizes the same qualitative methodology when analyzing the PLMs they fabricate.

While the methodology for the fabrication of transparent polycrystalline ceramics (i.e., housing for large flood lamps) has been established since the 1940s, such is not the case when it comes to reproducibly fabricating laser quality transparent polycrystalline ceramics (undoped or doped). Since the first demonstration in 1995 of lasing action in polycrystalline ceramic Nd:YAG, the process for fabrication of high optical quality PLM remains highly specialized and for the most part still a "black art". Optical transparency is not only the measure of the quality of PLM, it is also the feedback mechanism that allows for modification of the processing steps used in fabrication of PLMs. There is a need for optical metrology, to determine the quality of the polycrystalline materials (PLMs) being fabricated.

Transparency in solids has not been defined in definitive terms [87, 88]. The quality of a substance being transparent is called 'Diaphaneity', and is commonly used for precious gems to define their opacity or assessing the transparency of the mineral by comparing similar thicknesses. Diaphaneity is rated below five main categories, namely: Transparent (Tp), Semitransparent (S-Tp), Translucent (Tl), Semi-Translucent (S-Tl), and Opaque (Op), under which there are several other sub-categories [89].

The objective of this dissertation was to develop new methodology for characterizing bulk scatter in transparent PLMs. This chapter details the different experimental methods utilized to investigate bulk scattering as a function of material type (single crystal vs. polycrystalline), effects of dopant concentration and path length in PLM. The material types were single crystal and polycrystalline Erbium (Er) or Neodymium (Nd) doped YAG or Y_2O_3.

To investigate effect of scattering as a function of sample thickness, two samples (one single crystal and one polycrystalline) were cut into progressively shorter lengths by half. Six samples were created from a 50 mm long rod of single crystal 0.9% Nd:YAG and designated as: R1 (0.75 mm), R2 (1.25 mm), R3 (2.75 mm), R4 (5.5 mm), R5 (11 mm), and R6 (22 mm) (Figure 4.1). Six samples were cut from a 5 x 4 x 45 mm^3 block of 0.9% Nd:YAG PLM and designated as: B1 (0.53 mm), B2 (1.33 mm), B3 (2.71 mm), B4 (8.55 mm), B5 (10.87 mm), and B6 (22.1 mm) (Figure 4.2). The 12 samples (single crystal and PLM 0.9% Nd:YAG) were collectively referred to as the *cutback samples*. All input and exit faces of the 12 samples were polished to a mirror finish to minimize surface scattering and measure only the bulk scatter component.
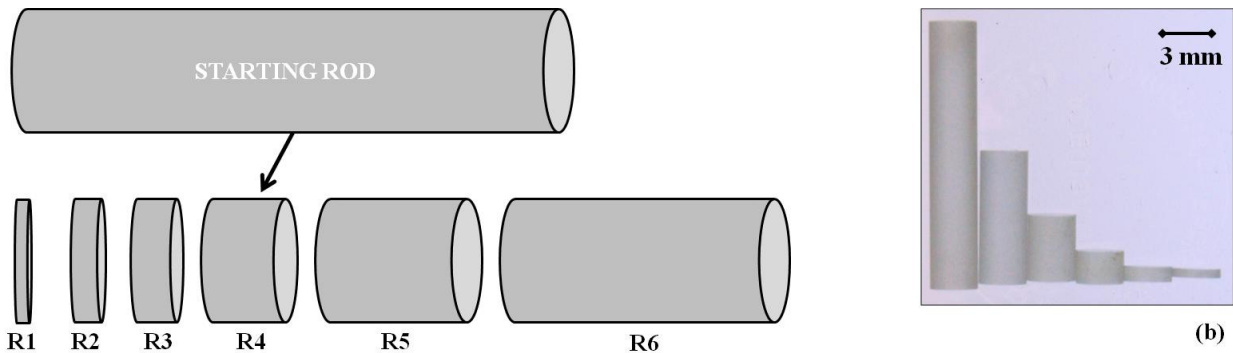
Figure 4.1: Single crystal 0.9% Nd:YAG cutback samples. Inset on the right shows the image of the samples.
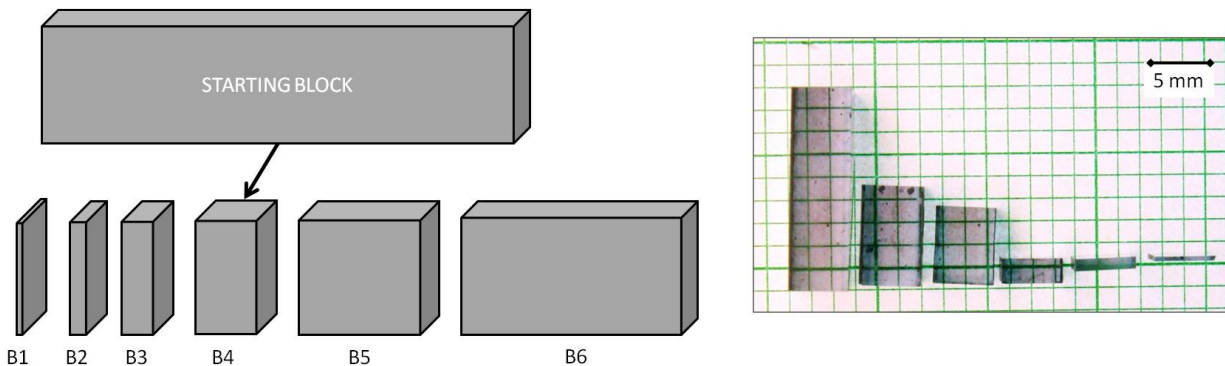
Figure 4.2: PLM 0.9% Nd:YAG cutback samples. Inset on right shows the image of the samples.

The polishing of the sample surfaces was done by a commercial company specializing in the polishing of laser gain media using proprietary techniques. Additionally, all 12 samples were batch polished at the same time and under the same conditions to minimize any possible variation in the surface polishing. Surface micro roughness scans were performed using an Atomic Force Microscope (AFM). The AFM (Quesant Q-scope 250) was operated with the cantilever in contact mode at a resonant frequency of 144.6 kHz. AFM scans of a 40 μm x 40 μm area were taken at multiple locations on the polished surfaces. From these scans, the Root Mean Square (RMS) surface height roughness value (in nm) provides the surface roughness metric. All polished samples exhibited RMS values below 10 nm and were deemed to be satisfactory to minimize surface scattering (Figure 4.3).

To protect the surface from dust contamination, the samples were kept in clean membrane boxes when not being utilized. Purified and filtered air was used to remove any loose particles present on the surface before cleaning. Before testing any sample, the surfaces were cleaned by methanol by the drop and drag method, to remove contaminants, particles and oil residue which would contribute to enhancing the measured bulk scatter signal.
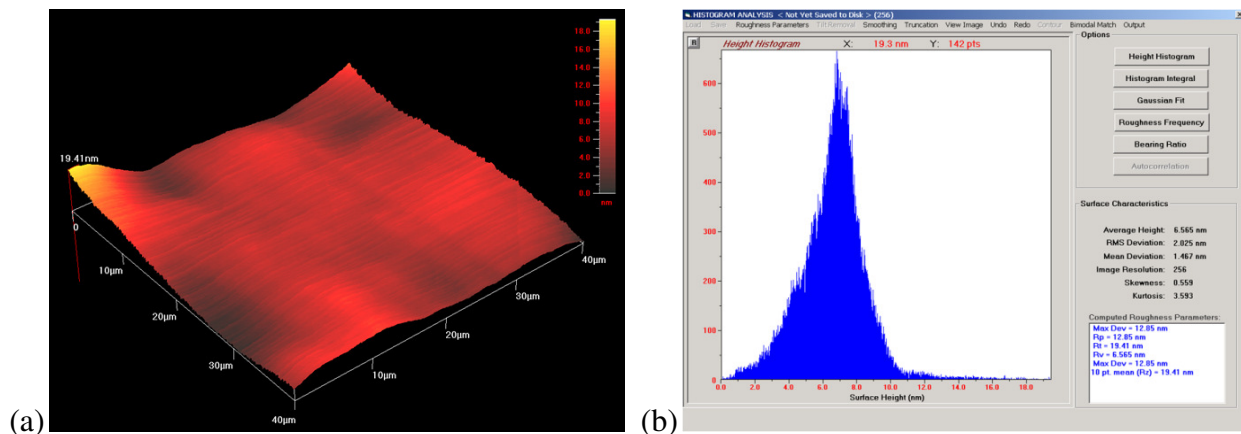
Figure 4.3: (a) A 40 μm x 40 μm surface area AFM scan of the polished surface of the 0.9% Nd:YAG polycrystalline ceramic sample (B2). (b) The average height was 6.5 nm with an RMS deviation of 2.2 nm.

Characterization of bulk scattering is not a single measurement, and one single method cannot provide adequate information on the quality of the material. Four methods and procedure have been developed which are more suitable and relevant for characterizing bulk scattering in these materials. Characterization of bulk scattering in PLMs is the collective assessment using these four methods. This chapter has four main sections, one for each of the characterization method. Each section describes the details of the experimental setup and design involved for each. Following it is the procedure for obtaining the data, analyzing the obtained information and interpreting the results. Finally, a discussion on the sensitivity of the method and limitation in identifying bulk scattering is mentioned.

Section 4.1 talks about *Optical Photography*. A modification of the most popular method of determining optical quality by a simple visual inspection of the materials is presented. The sample is placed at different heights above a standard resolution chart uniformly illuminated from below. A single set of uniformly spaced black resolution lines on the chart, are imaged through the sample. The reduction in contrast between the black lines and background, indicates the presence of scatter in the sample.

Section 4.2 explains the method of determining the *Transmitted Beam Wavefront Profile* (TBWP), which is used to image the distortions in the transverse intensity profile of a laser beam. The laser beam 'wavefront' and the corresponding intensity distribution is distorted, as the beam travels through the length of the sample. The extent of distortion are a direct result of bulk scattering present in the sample. This distortion is not evident from the measurements performed using optical photography.

This dissertation proposes that the distortion of the laser beam as it propagates through the media is a type of loss manifested through the non-uniform distribution of refractive index causing bulk scattering. It is this distortion of the beam wave front, which prevents the gain in a laser resonator cavity. This simple method is extremely fast and very efficient to determine bulk scattering in samples. The measurements were performed using laser beams in the visible and IR wavelengths, and characterization using visible beams was found to be more sensitive with better spatial high resolution.

Section 4.3 uses the *Angle Resolved Scattering* method to determine the spatial distribution of the scattered light as it propagates through the sample. Bulk scattering leads to the redistribution of energy away from the specular beam direction, into all other angles in space about the sample. This spatial distribution of the scattered energy is measured point by point using a rotating axis spectro-goniometer setup, and used to compare different samples.

Finally, Section 4.4 introduces the application of *Schlieren Imaging* to map the variations in the refractive index across the volume of solid sample. Schlieren imaging has been mostly used for imaging the density variations in rarified gases and liquids, but not for thick transparent polycrystalline ceramics. A modified version of the white light Schlieren imaging using a knife-edge as a filter is presented. This modified setup used a shaped light source, which is a conjugate of the knife-edge filter. Bulk scattering is due to the variation of the dielectric constant, which is manifested as varying refractive indices in different regions of the sample. Imaging the variation of refractive index allows us to view the source of bulk scattering in the samples. Analysis of the Schlieren images allows us to map the change in refractive index and compare different samples from analyzing the images. The method allows us to quickly image refractive index variations on samples with large dimension.

56

4.1   Optical Photography

A widely used method for evaluating transparency in transparent substrates is to image patterns on a standardized resolution chart (USAF-1951 test pattern) while looking through the test sample (Figure 4.4 (a)). This technique was established for evaluating commercial grade lenses and optical elements where the substrate material is already deemed to be of very high quality in terms of transparency. The technique is primarily used to determine the resolution limit of the lens or optical element.

The resolution limit is determined on the basis of visual assessment as to which line pairs on the chart can be best resolved as the spacing between the test sample and the paper containing the line pattern is increased. As a starting point, the USAF-1951 test pattern (or a picture with high levels of black and white details and contrast) is imaged while looking through the sample in question that is placed on top of the test pattern. The process is repeated with increasing distance between the test pattern and the sample in question.

By making the sample sufficiently thin (< 1 mm thick), it is possible to "see" the pattern underneath, even if the sample is translucent and exhibits a combination of surface and bulk scattering. However, if there is even a few millimeters separation introduced between the translucent sample and the surface of the paper containing the pattern, the pattern becomes blurry and/or unrecognizable.

The blurring of the pattern is often described in terms of Contrast Modulation (M) which provides a measure of the degradation and loss of resolution of the pattern [86]. Contrast modulation is determined by looking at a pattern which consists of black bars on a white background as shown in Figure 4.4 (a).
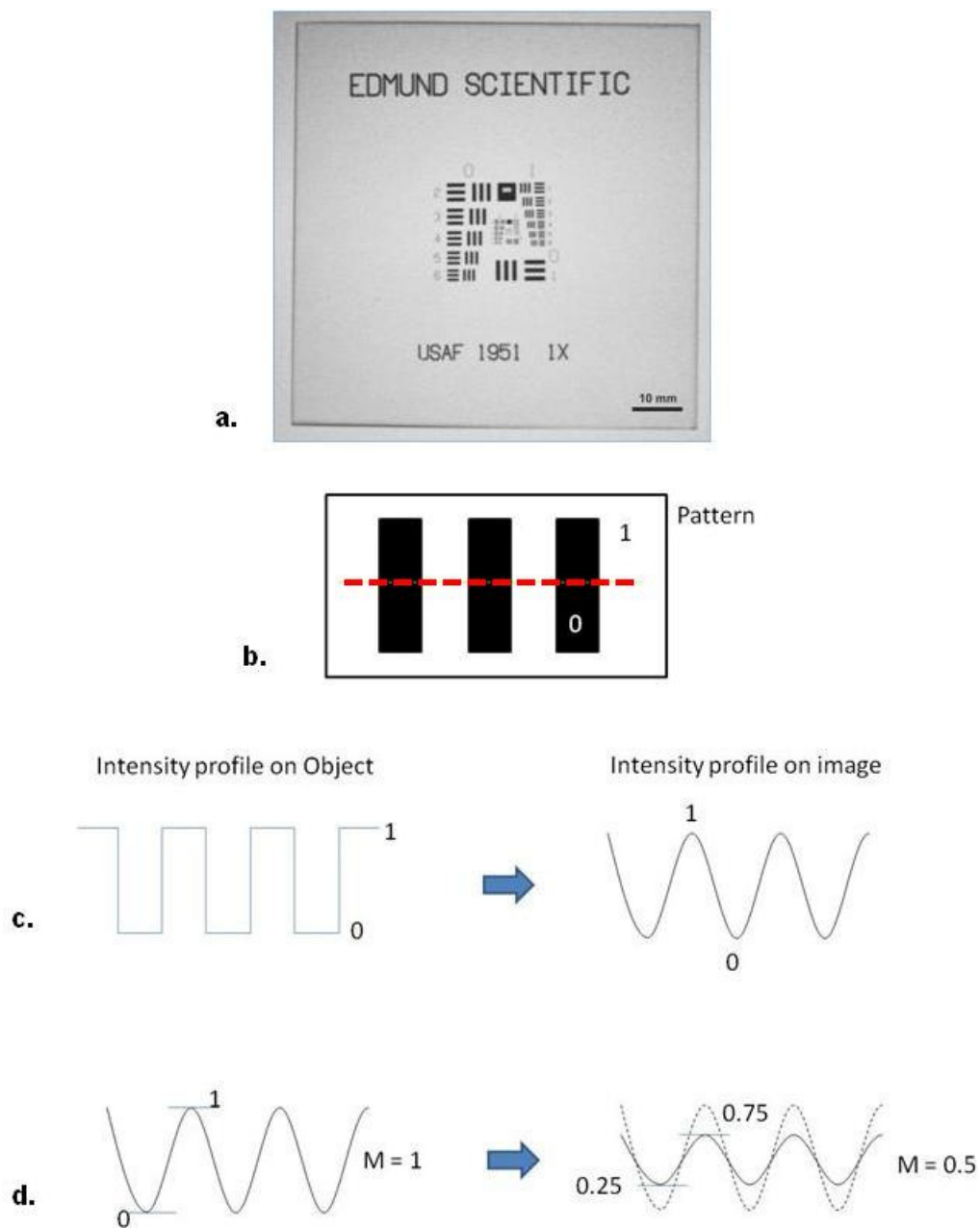
Figure 4.4: (a) USAF-1951 test pattern and the calculation of the contrast modulation. (b) Pattern on the resolution slide, (c) Line Intensity profile of the pattern and its corresponding profile on the image (d) lower value of the modulation corrosponding to a reduction of intensity on the image.

The plot of a line profile of the test pattern is called the spatial frequency as shown in Figure 4.4 (b). The contrast modulation is defined in terms of the intensity values from the plot as:

$$M = \frac{I_{max} - I_{min}}{I_{max} + I_{min}} \qquad (50)$$

where I_{max} is the maximum intensity, and I_{min} is the minimum intensity measured from the imaged intensity profile of the pattern. When the test pattern is imaged through a sample with any separation between the sample and the test pattern, the lines may exhibit a roll-off at the edge corresponding to blurring of the image due to diffraction. Diffraction, inherent to the wave nature of light, and the finite size of the optical elements dictate the resolution and the fundamental optical limit on the image quality of the pattern.

From Eq. 50, it is evident that the value of the contrast modulation depends on both the contrast as well as the brightness of the image. A modulation contrast value of unity (i.e., $I_{max} = 1$ and $I_{min} = 0$) represents a perfect transfer of contrast from the test pattern to the image. A modulation contrast value of zero (i.e., $I_{max} = I_{min}$) is obtained when there is no variation in the contrast, and it is not possible to differentiate between the black and white regions of the pattern. A modulation contrast value of zero is also used as the definition of "resolution", or the limit of operation for the optical element under test.

The aim of using optical photography in the present study was to determine if optical photography (imaging through PLMs instead of lens substrates and calculating the contrast modulation value) can be utilized to quickly and quantitatively characterize bulk scatter in PLMs. The use of optical photography for evaluating PLMs has not been attempted prior to this study. The only documented use of optical photography for evaluating polycrystalline materials

was in 1979 when the method was first used to study thin samples of polycrystalline alumina developed for use in high pressure sodium lamps (and not laser quality transparent PLM) [35].

The specific metrics used to evaluate optical substrates in conventional optical photography are the degradation in the sharpness and the reduction in the contrast of the line pattern in the USAF-1951 resolution chart. For the present study the same metrics were used to study PLM samples (polished to mitigate surface scatter), except the degradation in the sharpness and the reduction in contrast were interpreted as indicative of the presence bulk scatter only.

4.1.1   Materials and Methods

A USAF-1951 resolution target (Figure 4.5 (a)), also called a test target or a resolution chart was established in accordance with the American military-standard (MIL-STD-150A) to evaluate the optical performance of lenses and optical instruments [87]. The USAF-1951 test target (Figure 4.5 (b)) consists of several 'groups' of black and white line pattern arranged in decreasing size and labeled consecutively from 1 (the largest) to 6 (the smallest). Odd and even numbered groups are placed on the right and left side, respectively. Every 'group' consists of 6 'elements' which are further comprised of 3 horizontal and 3 vertical lines of the same length. The size of the individual elements and the structure of the test targets are standardized.

The length and spacing of the lines are also arranged in decreasing size. The size of the lines is reduced in discrete steps of $2^{-1/6}$ or 0.8909 from one element to the next element and from one group to the next group. The resolution is consecutively increased from one element to next element by the factor $2^{1/6}$. Figure 4.6 shows the setup used to image the resolution chart through the samples. A replica of the USAF 1951 1x standard resolution chart (Edmund Optics Inc.) was used as the imaging pattern [90].

60
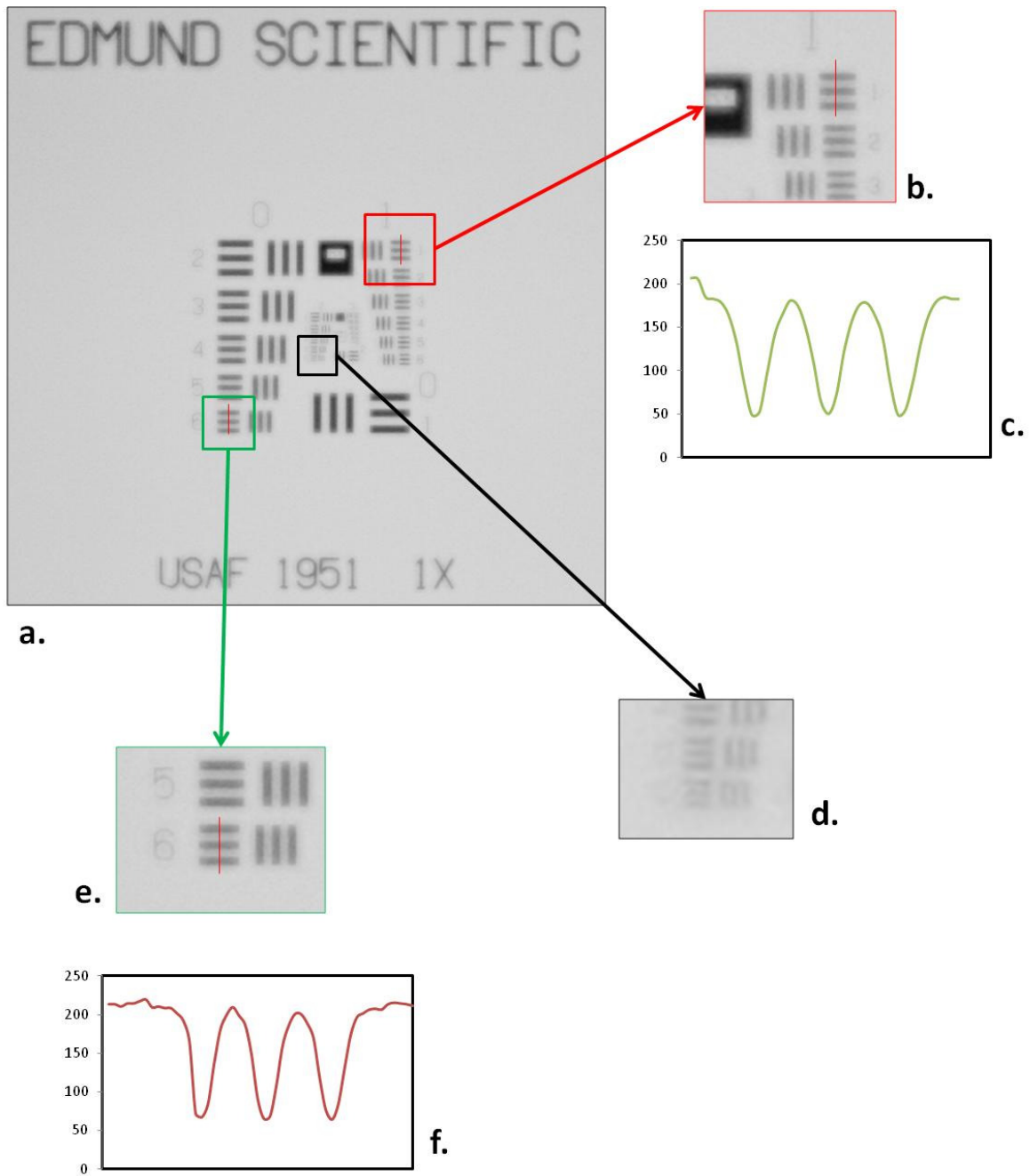
Figure 4.5: (a) USAF-1951 Resolution Chart; (b) the group 1, element 1 (2 line pairs / mm) resolution lines as imaged through the test sample; (c) the intensity profile of the line pattern; (d) the group 0, element 6 (1.78 line pairs / mm) resolution lines as imaged through the test sample; (e) the intensity profile of the line pattern; and (f) The resolution limit of the digital camera allowed imaging of lines at group 2, element 6 (7.13 line pairs / mm).

The transmissive replica pattern was created using a metal film deposited on a clear glass substrate. The resolution chart, with elements labeled from 0 to 6, was illuminated uniformly from below. The resolution chart was imaged through all the test samples at seven different heights (0 mm, 5 mm, 10 mm, 20 mm, 25 mm, 40 mm, and 50 mm) above the resolution chart. The legibility of the resolution lines on the chart was strongly related to the separation distance between the sample and the resolution pattern.
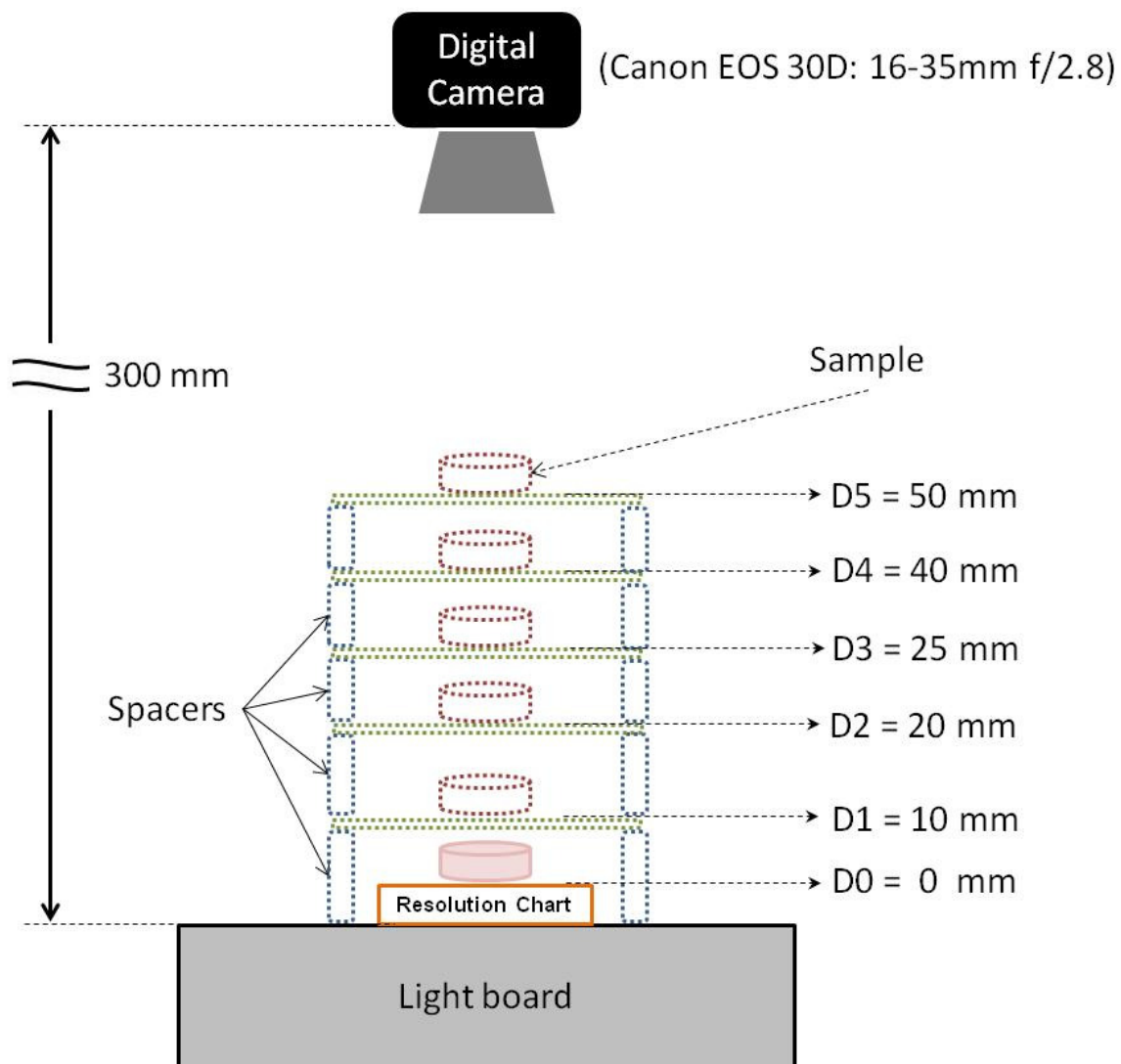
Figure 4.6: Setup for imaging the USAF-1951 resolution chart, using a digital camera. The images looking through the PLM samples are taken at seven different heights above the resolution chart.

A high resolution digital camera (Canon®, Model 30D - 10 mega-pixel CCD sensor, f/2.8 lens, ISO-1200, shutter speed (1/8000 sec)) was used to image the line pattern on the resolution chart. The camera distance to the resolution chart was kept constant at 300mm. The same two sets of line patterns were imaged for all the evaluations. The first set, Group 1, element 1 (2 line pairs / mm), was used as the test pattern on which the samples were placed. The second set, Group 0, element 6 (1.78 line pairs / mm), was used as a control pattern to make sure that the images taken by the digital camera were all at the same exposure level and in focus. Prior to evaluating the test samples, a baseline image was taken of the USAF-1951 resolution test chart without any sample.

Even though the resolution chart contained many smaller elements, the smaller elements were not used as they were beyond the resolution limit of the camera (i.e., beyond the camera's ability to distinguish the pattern on the chart). The maximum achievable resolution for the present optical system was determined to be the line set for group 2, element 6 (7.13 line pairs/mm).

The obtained images were converted to grey scale, but were not post processed for changing the intensity or contrast values. A Matlab® program was used to analyze the images and extract the intensity profile for the pattern (group 1, element 1) from the images. The maximum and minimum intensity values from the intensity profile were used to calculate the contrast modulation for each of the images. The modulation contrast was determined for four 5mm thick ceramic samples: R80050 (50% Er:YAG waveguide, Y183 (20% Er:Y_2O_3), Y184 (25% Er:Y_2O_3), and Y185 (50% Er:Y_2O_3). The 50% Er:YAG waveguide consisted of 1 mm thick Er:YAG bonded between 2 mm thick undoped ceramic YAG pieces.

4.1.2   Sample Cases and Results

Figure 4.5 (a) shows the baseline image of the resolution test chart in the absence of any test samples. Figure 4.5 (b-e) shows the two different line patterns and their corresponding intensity profile that were used for baseline and sample evaluation. Figure 4.5 (f) shows the resolution limit of the digital camera using the line pattern from group 2, element 6 (7.13 line pairs / mm).

From the intensity profile of the line pattern images (Figure 4.5 (c) and (e)), the "white" in the image corresponded to an intensity value of approximately 200 and the "black" in the image corresponded to an intensity value of approximately 50. Using Equation 50, the baseline contrast modulation was calculated to be M = 0.5625. The contrast modulation values obtained for all the test samples were compared to M = 0.5625.

Figure 4.7 to 4.10 depict the images obtained looking through samples R080050, Y183, Y184, and Y185. The effect of bulk scattering on the blurring of the image (i.e., the ability to resolve lines) appeared to be negligible when the samples was in direct contact with the resolution chart. Upon visual inspection of the images taken looking through all the samples, the line-pair pattern (group 1, elements 1) is visible at all seven distances.

However, at 40 mm and 50 mm separation distances from the resolution chart, there was a noticeable loss of contrast for Y183, Y184, and Y185. Figure 4.11 shows the summary of the calculated modulation contrast values as a function of distance between the resolution chart and the sample for each of the test samples as well as the baseline (i.e., no sample present). The general trend is that there is a loss of contrast looking through all four PLM samples as the separation between the PLMs and the resolution chart increases.
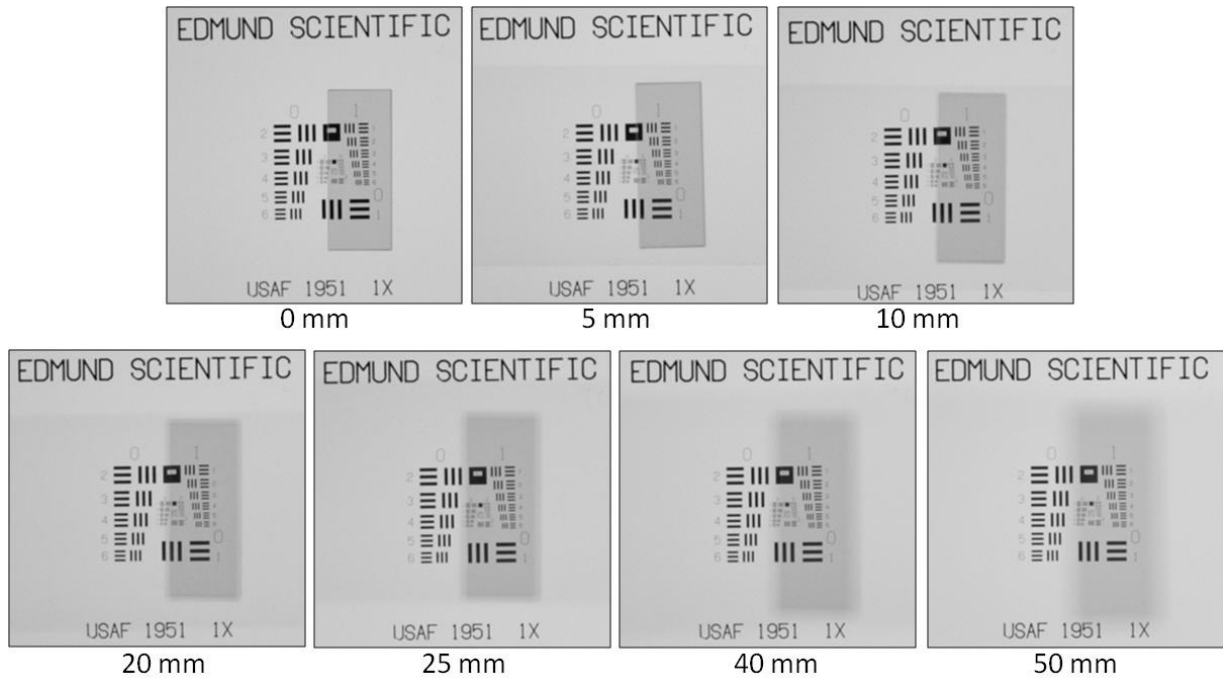
Figure 4.7: Images for sample R80050, at different heights above the resolution chart.
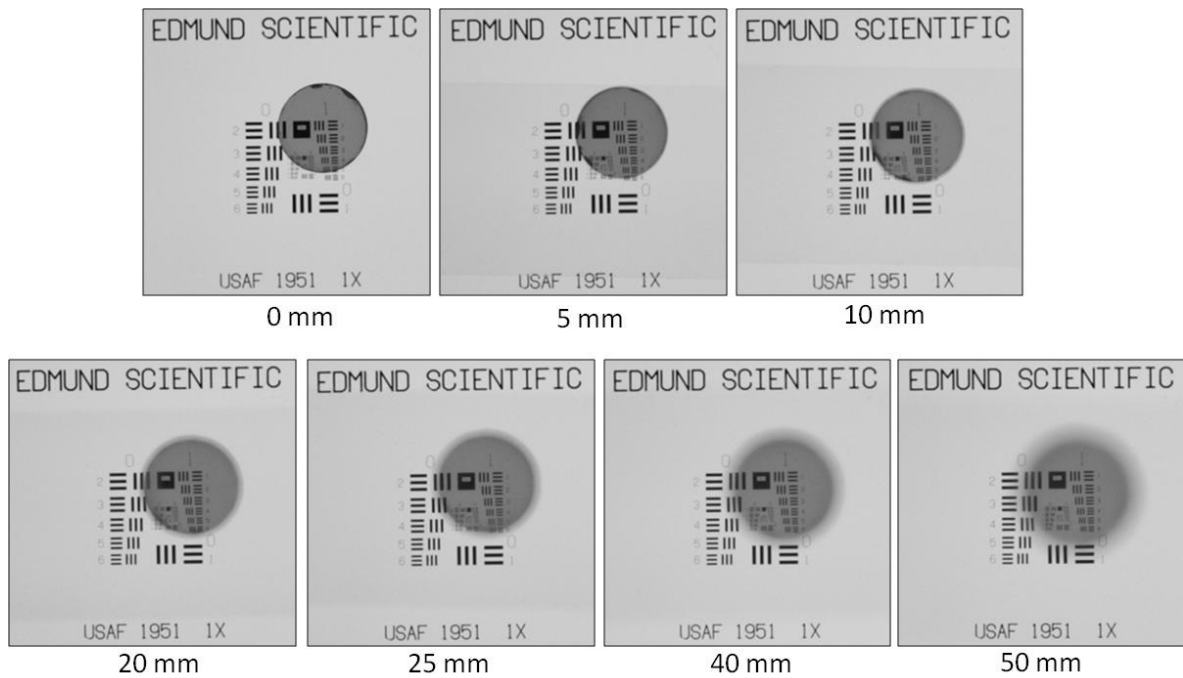
Figure 4.8: Images for sample Y183, at different heights above the resolution chart.
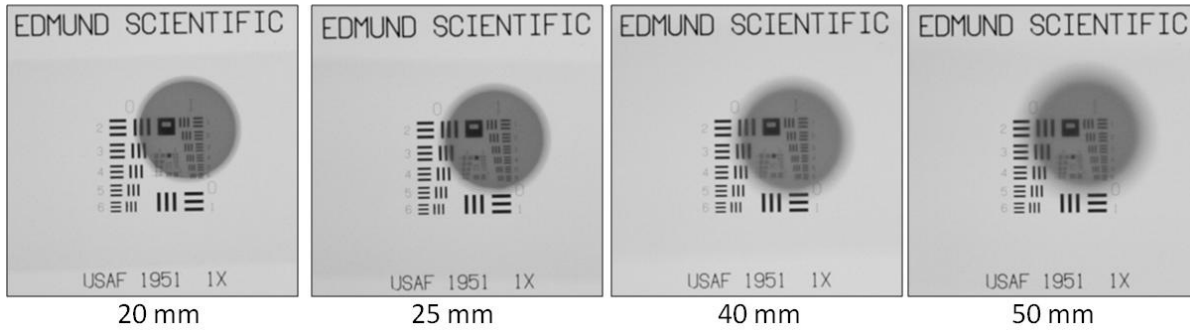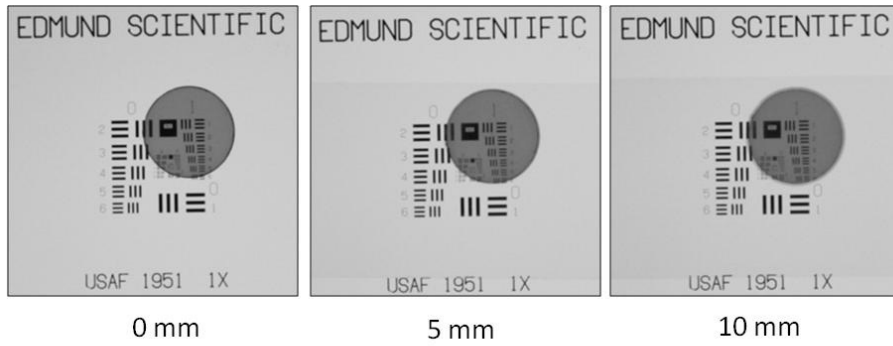
Figure 4.9: Images for sample Y184, at different heights above the resolution chart.
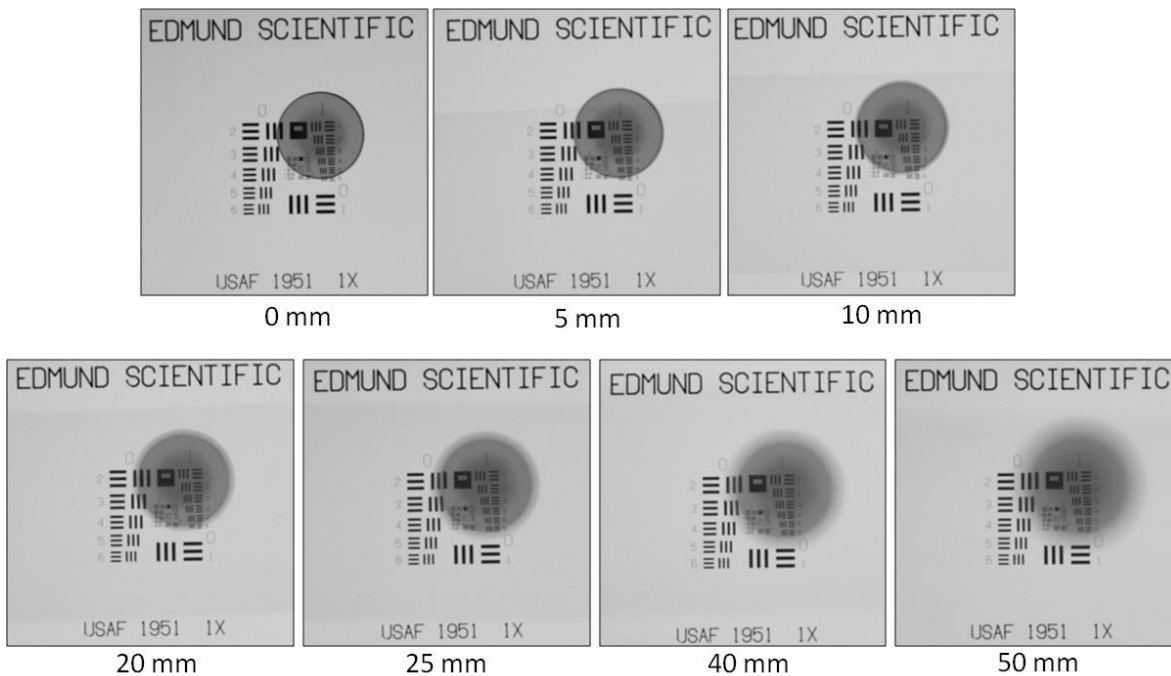
Figure 4.10: Images for sample Y185, at different heights above the resolution chart.

66

When the sample was placed on top of the contrast pattern (i.e., spacing distance = 0 mm), the modulation contrast value for the four PLM test samples ranged between M = 0.36 – 0.5614. The 50% Er:Y_2O_3 (sample Y185) had the worst contrast modulation value (M = 0.36) and the 50% Er:YAG waveguide (sample R080050) had the best contrast modulation value and was virtually identical to the baseline value of M = 0.5624.

For all the four test samples, the modulation contrast values decreased at varying rates with increasing distance from the resolution chart. At 70 mm distance separation, sample R080050 had the least reduction in modulation contrast value (M = 0.47) and sample Y185 had the most reduction in the modulation contrast value (M = 0.12).
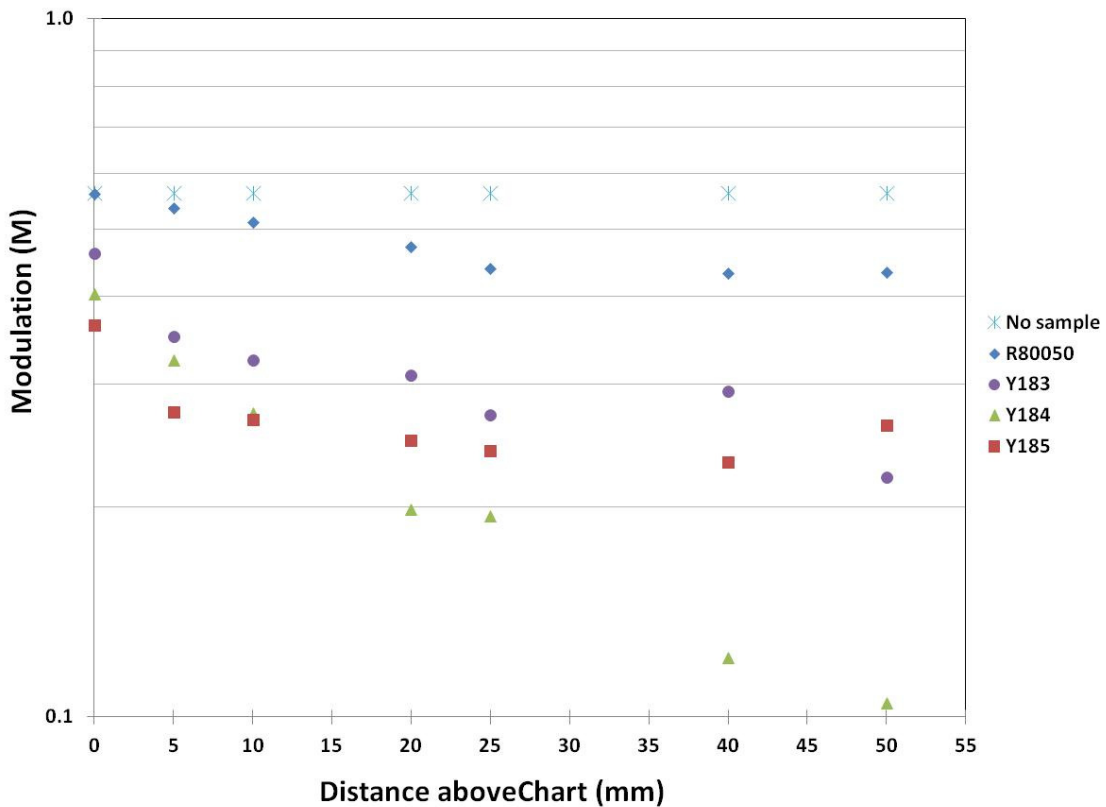
Figure 4.11: Semi-log plot of the contrast modulation for the four polycrystalline samples. The y-axis (contrast modulation) is in log scale. The baseline contrast value without any sample is represented by the black dashed line.

4.1.3   Discussion on Optical Photography

Even though the human eye is very sensitive at discerning contrast in a black and white line pattern, it is not able to accurately quantify a change in the intensity level. The resolution sensitivity of the human eye is approximately 0.7 arc-minute [91]. At this resolution sensitivity, the human eye sight is capable of detecting changes in the ambient light in the room, the color of an object, and the dwell time for staring at an image in order for the brain to register the image of the object.

Hence, even though the human eye can resolve the line pattern by simply "looking" at the pattern, it cannot accurately recognize or quantify the distortion in a transmitted EM wave or the reduction in contrast of the lines in the pattern due to the presence of bulk scattering. The method of optical photography was evaluated as a means to quickly and accurately assess the transparency of PLMs.

Optical photography was shown to be an acceptable method for determining the presence of bulk scattering in PLMs but not accurately quantifying the extent of bulk scattering present. The contrast between the line-pairs in the resolution chart is reduced as the separation between the PLM samples and the resolution chart is increased. This observation is confirmed by the contrast modulation values calculated using the intensity profiles obtained from the images line pattern in the resolution chart taken looking through the PLMs.

Utilizing the contrast modulation values, it is possible to identify a good quality PLM from a poor quality PLM as long as there is a significant difference in the contrast modulation values.

For the high quality polycrystalline transparent ceramic (e.g.,, sample R80050), there is only a decrease in the brightness of the image as the sample is moved away from the resolution chart. The contrast modulation value ($M_{R80050} = 0.562$) obtained when the high quality PLM sample (R80050) is in contact with the resolution chart is similar to the baseline contrast modulation value ($M_{Baseline} = 0.5624$) obtained without any sample. Under same conditions as just mentioned, for poor optical quality PLMs (e.g.,, sample Y185); the modulation value is significantly worst ($M_{Y185} = 0.36$) and decreases much quicker in comparison to the high quality PLM.

The most likely reason the contrast modulation value for the 50% Er:YAG waveguide was so much better than the other three PLMs is that even though the total thickness of the waveguide was 5 mm, the thickness of the doped region was only 1 mm compared to 5 mm as with the other three PLMs. One other cause of the difference in the modulation values is likely to be the difference in host materials (YAG vs. Y_2O_3).

Even though optical photography appeared to be a viable method for identifying the presence of and provide a measure for the bulk scattering in PLMs, as will be shown in subsequent sections that the method is not sensitive enough to quickly and accurately determine if a PLM will be useful for generating a laser. A different and better method is still need for evaluating PLMs.

4.2 Transmitted Beam Wavefront Profile

4.2.1 Introduction

Bulk scattering is one of the many loss mechanisms exhibited in single crystal or polycrystalline laser (gain) material (PLM). For laser oscillations to occur in a laser gain material, the round trip loss needs to be less than the gain of the system. Depending on the quality of the PLM, bulk scattering across the PLM gain material can be severe enough so as to distort the propagating wavefront and altogether prevent laser oscillations from occurring.

To date, bulk scattering characterization in PLMs has been relied on the ability to see a pattern through a polished thin sample that is placed directly on the pattern [35]. Although, the ability to see through a sample is a first order measure of the transparency, it is not an accurate and/or quantitative method for determining whether or not the material in question is of sufficient optical quality to be used for generation of laser radiation.

In addition to bulk scattering, there is also a reduction in transmitted intensity of the light as it passes through a thin sample which is measured using a FTIR (Fourier Transform InfraRed) spectrometer and typically represented by a percent transmittance [85]. While a simple FTIR transmission measurement is a valid and accepted method for determining the total reduction of inline transmission, it does not identify if the intensity reduction is due to absorption, surface or bulk scattering, or a combination of all three effects [92].

There is an unmet need for a fast and accurate method for assessing bulk scattering in PLMs. Transmitted Beam Wavefront Profiling (TBWP) was investigated as a possible method for rapidly and accurately ascertaining bulk scattering in PLMs.

TBWP utilizes degradation in the spatial profile of the transmitted beam intensity in the specular direction. The operational premise was that degradation in transmitted spatial profile is directly proportional to the extent of bulk scattering present in the PLM. A laser quality PLM having no or low scattering will have no or little degradation in the spatial profile of the transmitted beam and a poor quality PLM with significant scattering will cause severe degradation in the spatial profile of the transmitted laser beam. According to the ASTM definition of Haze, the specular direction is defined $< \pm 2.5^{\circ}$ of the forward direction of propagation of the laser beam [93].

Images of the transmitted wavefront profiles were used as a metric to assess: (1) bulk scatter in single crystal and (good and poor quality) PLM samples; (2) the effect of dopant concentration in PLMs of $Er:Y_2O_3$ doped with Erbium concentration ranging from 0.5% to 50%; (3) the effect of sample length using a matching set of different length single crystal and (good and poor quality) PLM 0.9% Nd:YAG samples.

4.2.2 Materials and Methods

Figure 4.12 shows a schematic of the setup used to determine the wavefront distortion in PLMs. To assess the degree of bulk scattering in a sample, the transmitted wavefront spatial profile of a laser beam propagated through the sample is compared to the diffraction limited incident beam (i.e., a laser beam have a perfect or "near perfect" a Gaussian intensity profile). The distortions introduced in the transmitted beam profile are imaged using a beam profiler. The laser source used was a multi-wavelength He-Ne laser (Research Electro-Optics Inc.) emitting a spatially diffraction limited beam at 633 nm, 612 nm, 604 nm, 594 nm, and 543 nm (user selectable) [94]. To isolate the effect due to bulk scattering only, a laser wavelength in the non-absorbing spectral region of the sample was selected.

The diameter of the output beam from the He-Ne laser was approximately 750 µm. Given that the output of the laser at the different wavelength varies and to keep the sensor array in the beam profiler from saturating, a variable attenuator was utilized to keep the laser beam intensity incident onto the sample as constant as possible. Even though the beam quality of the laser beam at the laser exit aperture is specified by manufacturers to be TEM_{00} (i.e., near diffraction limited Gaussian spatial intensity distribution), as the beam propagates further and further away from the laser a degradation in the spatial beam profile is sometimes observed. The degradation in the form of non-uniformities and intensity variations along the periphery of the laser beam is often due to the beam having propagated through an aperture and surface defects on the laser output coupler (the laser optic comprising the laser resonator).
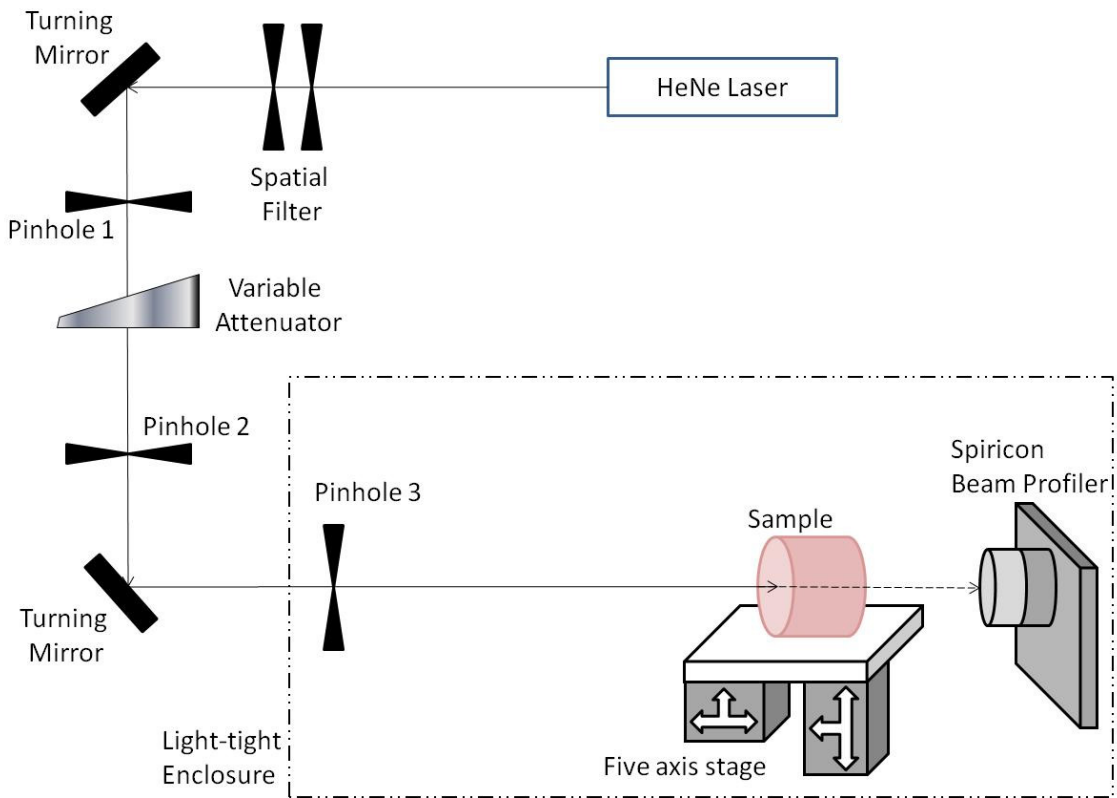
Figure 4.12: Experimental Setup used to image the transmitted beam wave front distortion.

Spatial filtering is a technique routinely utilized in the laser research community to remove the spatial variations and non-uniformities, and yielding a "cleaner" circular shaped beam. Spatial filters are often a pair of pin-holes (100 - 500 µm diameter depending on the incident beam size and power level) separated by a small distance (few cm). The laser beam is propagated through the spatial filter and the undesired structures are blocked from propagating. Additional apertures throughout the beam path can be/are utilized to have only the central diffraction limited beam incident on the sample.

In the setup shown in Figure 4.12, two 500 µm apertures with 1 cm separation were placed 10 cm from the laser exit aperture. Additional 1mm diameter apertures are utilized after each turn mirror and attenuator. The samples are precisely aligned relative to the laser beam using on a 5 axis (x-y-z linear motion, tip-tilt and rotation) stage. To prevent stray light from affecting the measurements, the sample and the laser beam profiler are placed in a light tight box. Furthermore, the samples used for all the measurements are of the same thickness (~ 5 mm), and polished to laser quality surface finish with similar surface micro-roughness as determined using AFM. Each sample, with polished surfaces normal to the incident beam, is aligned 1 - 2 degrees off normal to prevent retro-reflection from the sample surface directly back into the laser.

The beam transmitted through the sample is imaged by a beam profiler (Spiricon Laser Beam Analyzer Model LBA-USB/USB-SP). The beam profiler camera (USB L-230) uses a CCD sensor with a spectral response from 190 nm to 1320 nm [95]. The beam profiler creates high-speed, high-resolution, false color beam intensity profiles which can be represented in both 2-D and 3-D images, with a color-coded intensity scale from zero value (dark purple, no intensity) to 4095 (white, saturated). The pixel spacing on the detector is of 4.40 x 4.40 µm-square, and produces a 1616 x 1216 resolution image. Two neutral density (ND-5) filters are

used to attenuate the incident intensity on to the sensor and prevent the sensor from being saturated from the laser beam.

The baseline consists of laser beam wavefront profiles taken without any sample present at the beginning and after evaluating the test samples. The second set of baseline profiles are taken to insure that there were no changes in the beam wavefront profile quality. The samples were evaluated by taking transmitted wavefront profiles at multiple locations on the sample. In efforts to quantify the degradation of the transmitted wavefront profile, the full width half maximum diameter of the line profiles across the X- and Y-axis through the middle of the image captured by the beam profiler were calculated.

MATLAB® software was used to obtain the line profiles from the images captured by the beam profiler. Finally, the QuickGraph© software was used to fit a Gaussian distribution to the line profiles [96]. The FWHM values are averaged for the X-axis and Y-axis, and are represented as the number of pixels.

4.2.3   Sample Cases and Results

The images of the reference beam profiles (Figure 4.13) show that the incident laser beam is diffraction limited with no irregularity to the Gaussian intensity distribution. Figure 4.14 shows the 2-D beam profiles of the transmitted wavefront across the different test samples. The transmitted wavefront images taken at multiple locations through a single crystal 50% Er:YAG and polycrystalline 0.5% Er:Y_2O_3 samples (Figure 4.14 (a) and (b)) show little or no degradation in the transmitted beam quality. There was a noticeable reduction in the peak intensity of the transmitted beam.
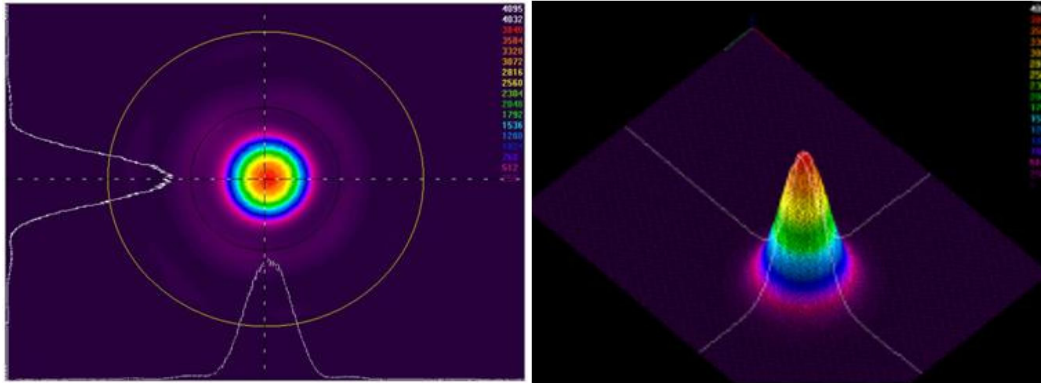
Figure 4.13: The spatial profile (2-D (left), 3-D (right)) image of the incident laser beam from the He-Ne gas laser ($\lambda = 632$ nm, without sample present).
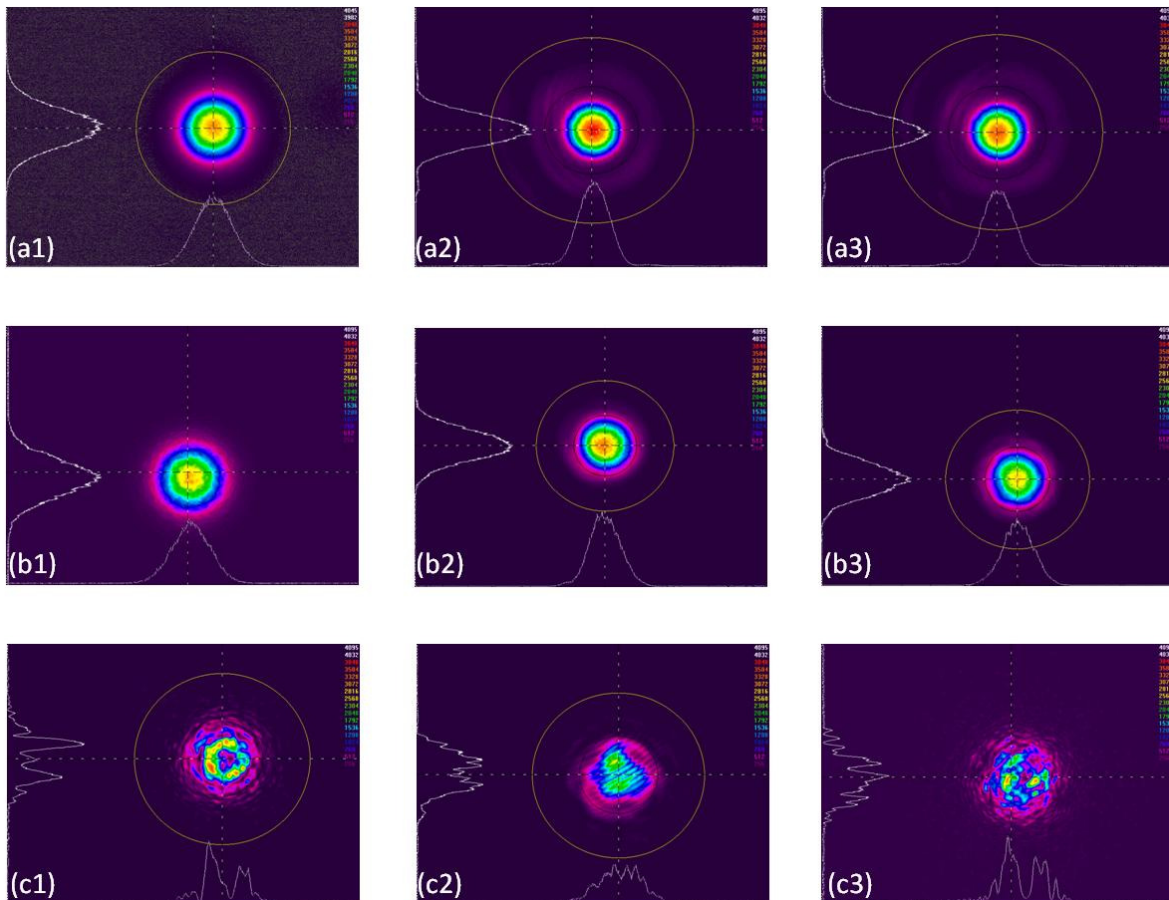
Figure 4.14: Transmitted beam wavefront profile at different locations on the same sample, through a single crystal 50% Er:YAG (a1 – a3); a high quality PLM 0.5% Er:Y_2O_3 sample (R80098) (b1 – b3); and a poor quality PLM 20% Er:Y_2O_3 sample (Y183) (c1 – c3).

Visually, in the case of the single crystal 50% Er:YAG, and the PLM 0.5% Er:Y_2O_3 sample, the absence of haze in the bulk of the sample when held up to a light source is indicative of the absence of bulk scatter. The transmitted beam profile across a PLM, 20% Er:Y_2O_3 (Figure 4.14 (c), Sample Y183) shows significant degradation in the transmitted wavefront. The incident Gaussian profile was broken apart into randomly shaped and distributed beamlets. Visually, the presence of haze within the sample, when held up to a light source, is indicative of high degree of bulk scatter in the sample.

Figure 4.15 shows the 2-D beam profiles of the transmitted wavefront through Er:Y_2O_3 samples as a function of erbium concentration with Erbium concentration ranging from 0.5% to 50%. The transmitted wavefront was degraded starting with the 0.5% Er:Y_2O_3 sample and became progressively worse as the erbium concentration increased to 50%. At 50% erbium concentration, the transmitted wavefront had no resemblance to the starting diffraction limited Gaussian profile.

(Y989) 0.25% Er: Y_2O_3 (Y990) 0.5% Er: Y_2O_3 (Y991) 1% Er: Y_2O_3 (Y992) 2% Er: Y_2O_3

(Y993) 5% Er: Y_2O_3 (Y994) 10% Er: Y_2O_3 (Y995) 25% Er: Y_2O_3 (Y996) 50% Er: Y_2O_3
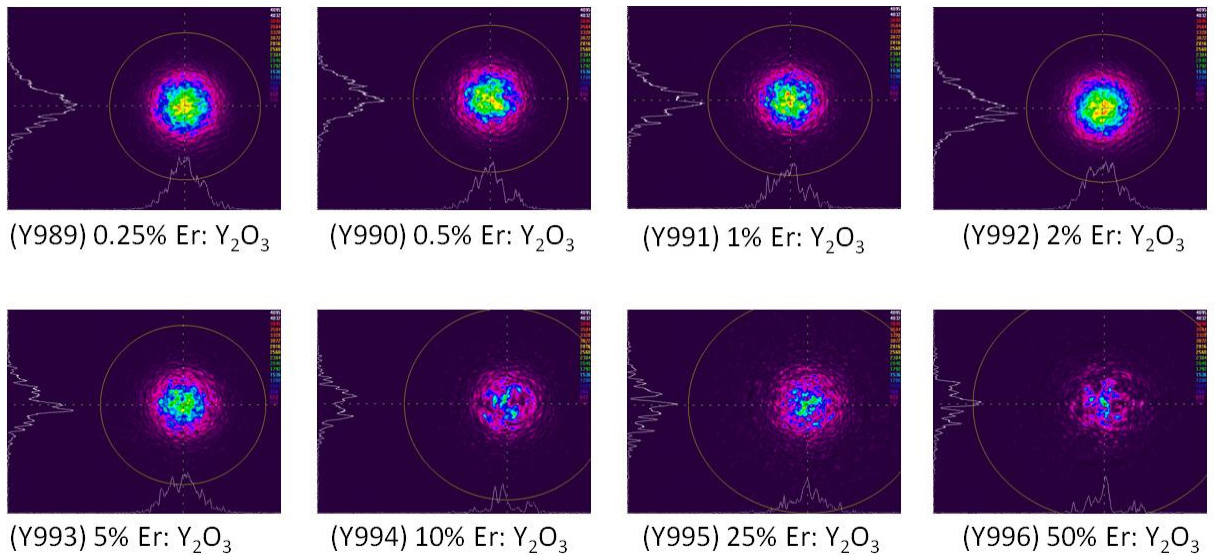
Figure 4.15: Transmitted wavefront images across Er:Y_2O_3 with different concentrations of Erbium. All measurements were made using a 632 nm He-Ne laser.

Figures 4.16 and 4.17 show the 2-D beam profiles of the transmitted wavefront after the beam has propagated across different thickness of a single crystal and PLM 0.9% Nd:YAG, respectively. In the case of the single crystal 0.9% Nd:YAG samples, no degradation in the transmitted wavefront is observed regardless of the sample lengths.

In the case of the PLM 0.9% Nd:YAG samples, the thinnest sample (t = 0.53mm) showed perhaps the best transmitted wavefront profile, with some degradation to the diffraction limited Gaussian profile that was incident onto the sample. All other sample thicknesses showed progressively increasing degradation in the beam quality.

Visually, the single crystal samples did not exhibit any bulk scattering as indicated by the absence of any haziness in the samples, whereas the PLM 0.9% Nd:YAG sample showed considerable scattering as indicated by the presence of haziness which became progressively worse with increasing sample length. The above qualitative assessment is supported, in principle, by the graph of the FWHM line profile taken from the transmitted wavefront profile as a function of sample thickness (Figure 4.18). The FWHM value of the reference beam (without any sample) was 70.

In case of the single crystal samples, the distortions to the wavefront were minor with the FWHM remaining fairly constant (FWHM = 71 ~ 73) as a function of sample length. In the case of the PLM 0.9% Nd:YAG sample, the distortions in the transmitted wavefront profile are minor for the thinnest sample (t = 0.53mm) but quite severe for the longest sample (t = 22.1mm). The FWHM value increased dramatically as a function of sample length starting with FWHM of 71 for the thinnest sample and to FWHM of 86 for the longest sample.
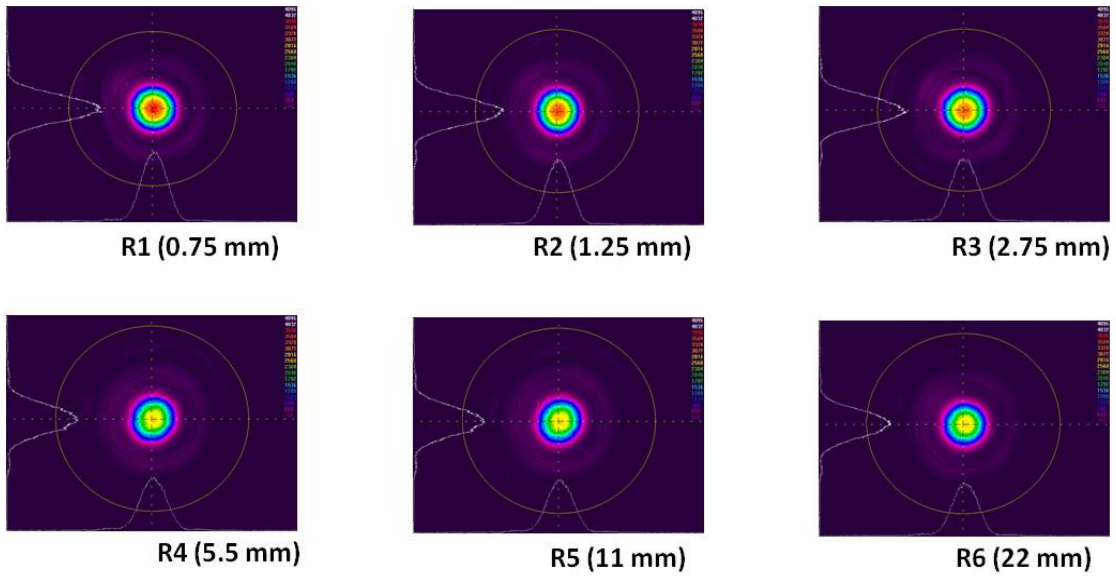
Figure 4.16: Transmitted wavefront profiles across different lengths of single crystal 0.9% Nd:YAG samples (cutback set).
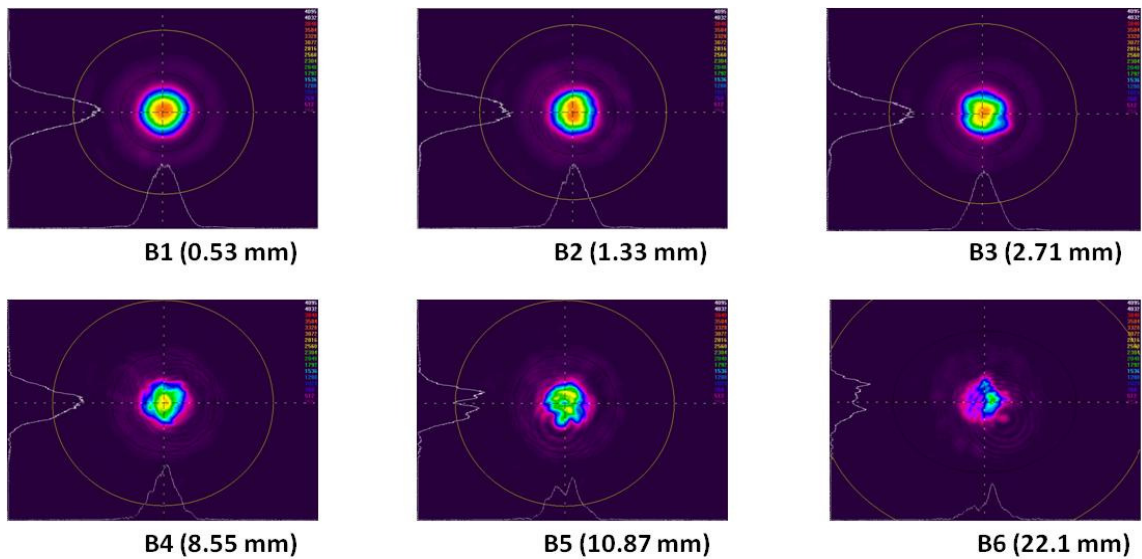
Figure 4.17: Transmitted wavefront profiles through different lengths of PLM 0.9% Nd:YAG samples (cutback set).
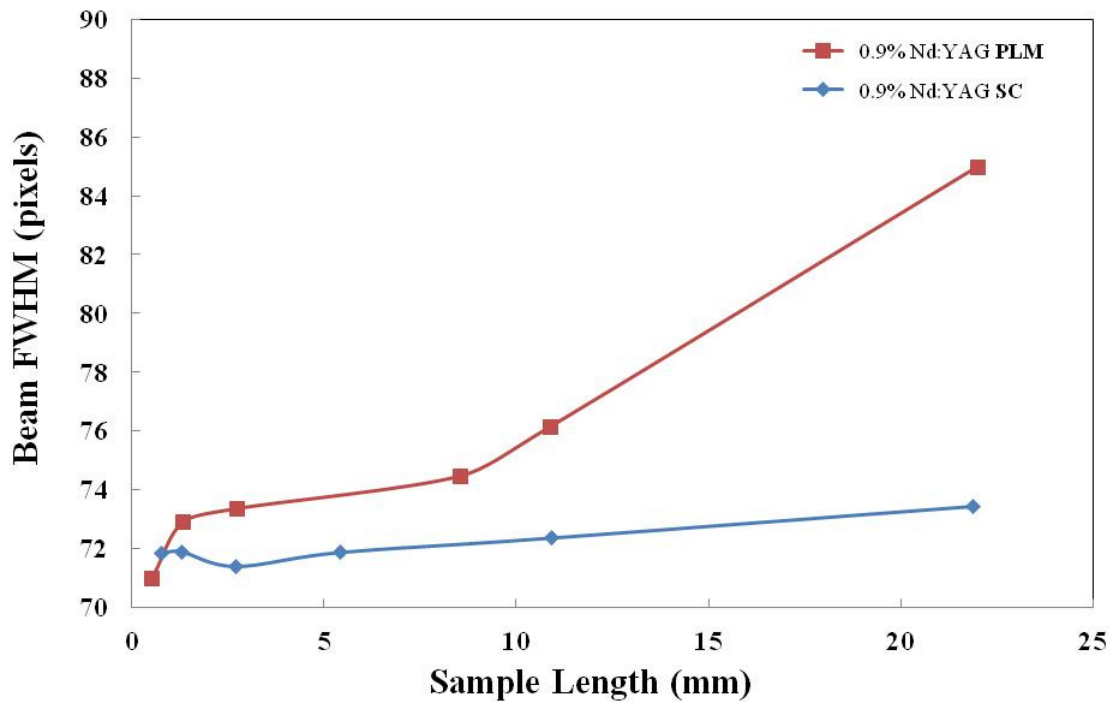
Figure 4.18: FWHM sizes for transmitted wavefront profiles of a 632 nm laser beam propagating through single crystal and PLM 0.9% Nd:YAG samples.

4.2.4   Discussion on Transmitted Beam Wavefront Profile

Bulk scattering has been identified as a loss mechanism for an EM wave propagating through a single crystal or polycrystalline sample. Depending on the severity of the bulk scattering for a laser gain material, bulk scattering is manifested by lower laser output power or even the absence of laser oscillations. While the ability to "see" a pattern through a sample has been used as a first order metric to measure the transparency of the sample, the method is far from an accurate and/or quantitative method for determining whether or not the material in question is of sufficient optical quality to be used for generation of laser radiation. Nor is the first order method able to distinguish if the scatter is due to a surface or bulk, or a combination of both effects. Thus there is a need for a fast and accurate method for assessing bulk scattering in PLMs.

79

Transmitted Beam Wavefront Profiling (TBWP) was investigated as a possible method for rapidly and accurately ascertaining bulk scattering in PLMs. The operational premise of TBWP was that degradation in the spatial profile of the transmitted beam is directly proportional to the extent of bulk scattering present in the PLM. A laser quality PLM having no or low scattering will have no or little degradation in the spatial profile of the transmitted beam and a poor quality PLM with significant scattering will cause severe degradation in the spatial profile of the transmitted laser beam.

Transmitted Beam Wavefront Profiling (TBWP) allows the direct imaging of the distortions introduced by bulk scattering in a PLM sample. The distortions observed are a direct manifestation of the presence of refractive index inhomogeneities in the PLM sample. As the incident laser bean falls on the sample, different regions of the incident beam experience different refractive index profiles as it propagates through the PLM. This inhomogeneity in the refractive index of the sample, cause different regions of the incident beam to deflect away from the initial propagation direction.

With every refractive index variation encountered, different regions of the incident beam experience minute deflections from their path, due to refraction. This causes a breakup of the incident laser beam and the single beam effectively appears as multiple beamlets (Figure 4.20). With each deflection, each of the beamlets travels a different effective path length through the PLM sample, which eventually results in different phase for as they exit through the PLM sample. As they emerge out of the PLM sample, each of the individual beamlets has a different propagation direction (due to multiple deflections) and phase. At the imaging plane, the interference and superposition of the individual beamlets results in a complex and random distribution intensity distribution. This random intensity distribution is the distortion in the

transmitted beam, and is different for different locations of the PLM sample. The TBWP technique was shown to be faster and significantly more sensitive technique for characterizing bulk scatter in PLM over the currently used method of optical photography which relies upon the ability to "see" a resolution pattern through the PLM. The TBWP technique was especially useful in clearly showing the presence of scatter sufficient to render the PLM sample as being non-laser quality but otherwise would have been labeled as being laser quality transparent PLM.

The transmitted beam wavefront profiles (TBWP) for the single crystal 50% Er:YAG and the high quality PLM 0.5% Er:Y_2O_3 samples (Figure 4.14 (a1 - a3), (b1 – b3)) are indicative of high degree of uniformity in the refractive index across, and thus the absence of bulk scatter in both types of samples. The reduction in the transmitted intensity is due to the Fresnel reflection losses from the front and the back faces of the sample since the sample are not anti-reflection coated. In the case of a PLM 20% Er:Y_2O_3 (Y183) sample, although the resolution pattern was clearly visible, some degradation in contrast was observed looking through the sample (Figure 4.8). However, TBWP technique showed for sample Y183 (Figure 4.14 (c1 – c3)) the presence of scatter severe enough that the PLM could not be used to generate laser radiation, and is discussed in more detail in Chapter 5 (Figure 5.8, and 5.9)

The TBWP technique was also shown to be useful to characterize the degree of scattering as a function of dopant concentration in the PLM and path length of the PLM. Specifically, transmitted wavefront profiles were evaluated for (1) Er:Y_2O_3 with the Erbium concentration ranging between 0.5% to 50% atomic weight percent; (2) single crystal 0.9% Nd:YAG of path lengths from 1 mm to 22 mm; and (3) and PLM 0.9% Nd:YAG sample of path lengths from 1 mm to 22 mm. Using the current method of evaluating scatter by looking at a pattern through the PLM, all eight concentrations of polycrystalline Er:Y_2O_3 samples as well as all five different

path lengths of the single crystal and polycrystalline 0.9% Nd:YAG samples would have been qualified as being laser quality transparent with very low-to-low scatter. However, using the TBWP technique, for evaluating the effect of doping, the profiles in Figure 4.16 show the presence of significant levels of scattering starting with the 0.5% Er:Y_2O_3 sample and becoming progressively worse with increasing Erbium concentration.

As a function of path length, the TBWP technique showed no scattering in the single crystal 0.9% Nd:YAG. However, in the case of the PLM 0.9% Nd:YAG, TBWP showed the presence of scatter starting with sample thickness of just over 1mm and becoming progressively worse with increasing thickness. The difference in the ability to detect minute levels of scatter in a single crystal or a PLM using TBWP method, whether as a function of material type (single crystal or polycrystalline), path length, or dopant concentration, is primarily due to the type of the illumination source utilized. The optical photography technique utilizes a white light source and relies on contrast resolution as a metric for qualifying the degree of scatter (and thus quality of the sample). The TBWP utilizes a laser beam which has high temporal and spatial coherence.

It has been mentioned that bulk scattering is primarily due to the presence of random distribution of the refractive index in the bulk of the PLM (i.e., $\Delta n/\Delta x$). The interaction of an incident plane wave with the non-uniform refractive index in the PLM results in formation of beamlets that travel in different directions and have different phases (Figure 4.19). It is the interference of the beamlets that is captured and displayed by the beam profiler as random intensity distributions. Since a white light source does not have high temporal or spatial coherence, no interference pattern is captured by the beam profiler. The fact that a white light source does not have a high temporal and spatial coherence is also why some contrast through even a bad quality PLM will be observed.

Summarizing, it is this difference in the temporal and spatial coherence length between a laser and a white light source that allows for the effect of bulk scattering to be observed on the CCD array of the beam profiler. One important aspect of TBWP imaging is that the effects being imaged are for a single pass through the material. In the case of a laser resonator, the laser beam makes hundreds of round trips through the material before emerging out of the cavity. Hence, any degradation observed in the beam is greatly amplified and results in loss leading to laser oscillations not being generated.
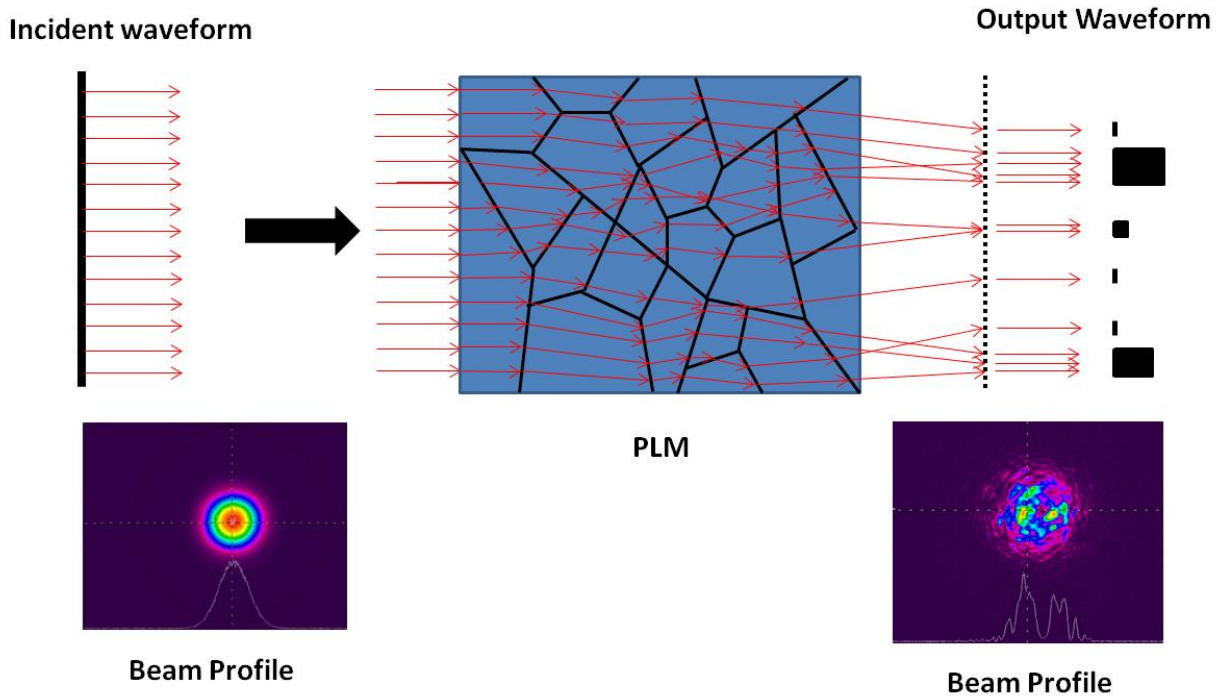
Figure 4.19: Distortion introduced to the incident laser beam, as it propagates through the PLM. The dark lines shown inside the PLM body are representative of local refractive index inhomogeneities and discontinuities, as observed by the incident laser beam. The incident laser beam has a uniform circular shape and a Gaussian intensity distribution. After passing through the PLM sample, the transmitted beam has a distorted shape due to bulk scattering.

4.3 Angle Resolved Scattering

4.3 Introduction

Angle Resolved Scattering (ARS) or Goniospectrophotometry performs measurements of scattered light at all possible angles about a sample, mapping the intensity for both forward scatter and back scatter regions. This technique employs the detection of scattered light at discrete angles, measured by a single detector moved over the whole range. The method was first shown by Stover, and the goniometer is sometimes also called a Stover Scatterometer [30].

Haze is defined under the ASTM standard (E2175-01) as "the percent of total transmitted light, which in passing through the specimen, deviates from the incident beam through forward scatter by more than 0.044 radians or 2.5^{o} on the average" [97]. Haze is the result of light scattering through a transparent material resulting in poor visibility and loss of contrast. But, haze, represented as a percentage of transmitted light, does not describe the angular distribution of the scattered light, and also disregards the amount of light that is backscattered, absorbed or re-emitted by the sample [97].

As was shown with the transmitted beam wavefront distortion measurements, bulk scatter is identified to be a distortion introduced to the incident beam as the beam travels through the material. The transmitted beam wavefront distortion measurement is used to quantify the effects of bulk scatter on the main beam within a $< 5^{o}$ ($+/-2.5^{o}$) cone angle of the main beam axis. This method does not give any information about spread of the beam and is also not useful for comparing samples which show similar patterns for wavefront distortions, for the direct beam. Figure 4.20 depicts the terminology and methodology used in ARS. The near-field region is usually distances of $1/2\pi$ times the wavelength (0.159 x λ) from the source.

84

The radiative near-field (Fresnel region) covers the remainder of the near-field region, from $\lambda/2\pi$ out to λ (one full wavelength), beyond which it is considered as the far field region [98]. A collimated beam of coherent light (Figure 4.21 (a)) is directed normally on to the sample surface. The path of the incident laser beam is in the direction from the 180° marker to the 0° marker. Most of the incident beam is transmitted through the sample along the same direction as the incident beam.

A linearly polarized laser beam was used, and no attempts were made to determine the polarization state of the scattered light about the sample. The transmitted beam consists of energy which is not deflected by more than 2.5^o from the optical axis of incident beam direction (Figure 4.21 (b)). The distortion of the wavefront due to scattering of the transmitted beam in the forward direction (Figure 4.21 (c)) is imaged using the procedure in section 4.2.
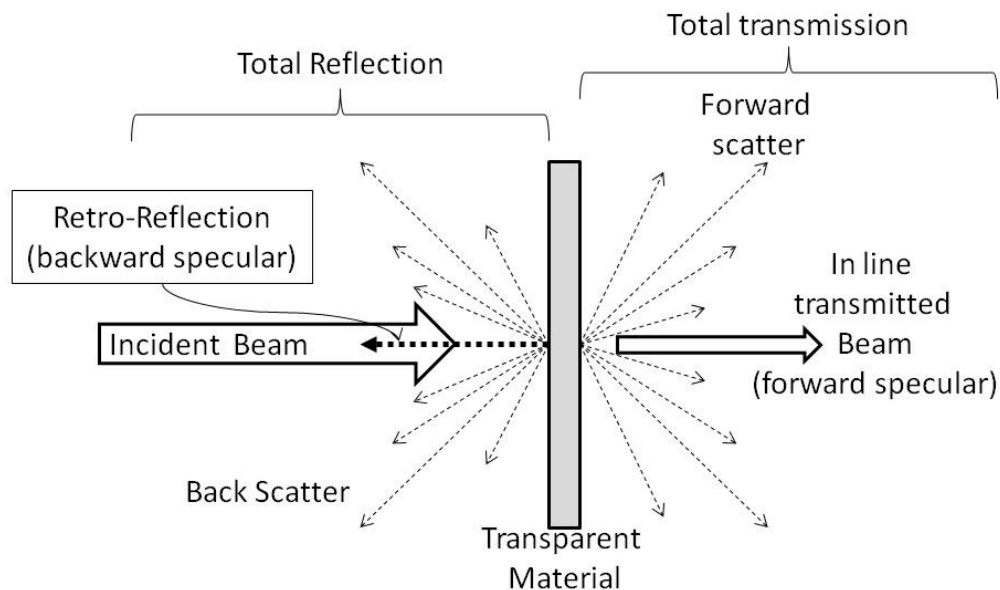
Figure 4.20: Illustration of the interaction of light with an optically transparent polycrystalline ceramic.

A portion of the incident light onto the sample surface due to Fresnel reflection is retro-reflected back at a very shallow angle (< 0.1°) along the incident beam direction, and directed into a beam dump. This prevents the retro-reflected beam from modifying the measurement of the scattered intensities in the forward and backward directions. The total value of the reflected intensity, from the front and back faces of the sample is calculated using the Fresnel equation. A small portion of the incident light is scattered in all directions around the sample. This scattered light intensity is measured point-by-point, and represented as a 2-D polar map.

A map of the scattered intensity distribution in all angles is shown in Figure 4.21 (d). The map shows two distinct regions, one comprising intensity distribution of the forward scattering direction, and the other in the backscatter direction. The intensity distribution patterns are smooth and not oscillatory as predicted by single particle scattering simulations using the Mie scattering theory [99]. The sharpness of the forward and the backward peak in the scatter plots indicates that the scattering is predominantly due to large particles (d > λ, where λ is the probe laser wavelength) [113]. The intensity in the pedestals for the forward scatter and backward scatter lobes are dependent on the degree of scatter in the sample. The two main requirements for performing such a comparison are: (i) the samples have to be of the same thickness, and (ii) the surfaces of the samples should be mirror polished and flat parallel (< 0.1 ° angle between them) to prevent deflection of the specular beam from the normal and creation of multiple beams from retro-reflections.

The 'severity' or degree (amount) of bulk scattering present in a particular sample is evident in the intensity distribution. The intensity distribution for only the forward scattering lobe is used for comparison [114]. The statistical properties of the laser speckle field created when light is scattered by a medium with random fluctuations in the refractive index have been

extensively investigated [100]. The intensity distribution of the speckled field is due to the random interference and superposition of the scattered elementary waves. Each of the wave element experience a random phase shift as it propagates through the material having this random refractive index variation [101]. Different regions of the incident plane wave, from a light source, are refracted differently when passing through an inhomogeneous medium. This is due to the difference in path length (light travel time) through the medium, which is related to the distribution of the refractive index in the media. The correlation between the intensity distributions in the far field of the scattered light does not give any information on the statistical properties (size and number) of the scatterers [102, 103]. This resultant speckle from multiple incoherent sources, in the near-field is dominated by the closest source, but in the far field, all the sources contribute equally to the speckle pattern and appear coherent in far field [103].
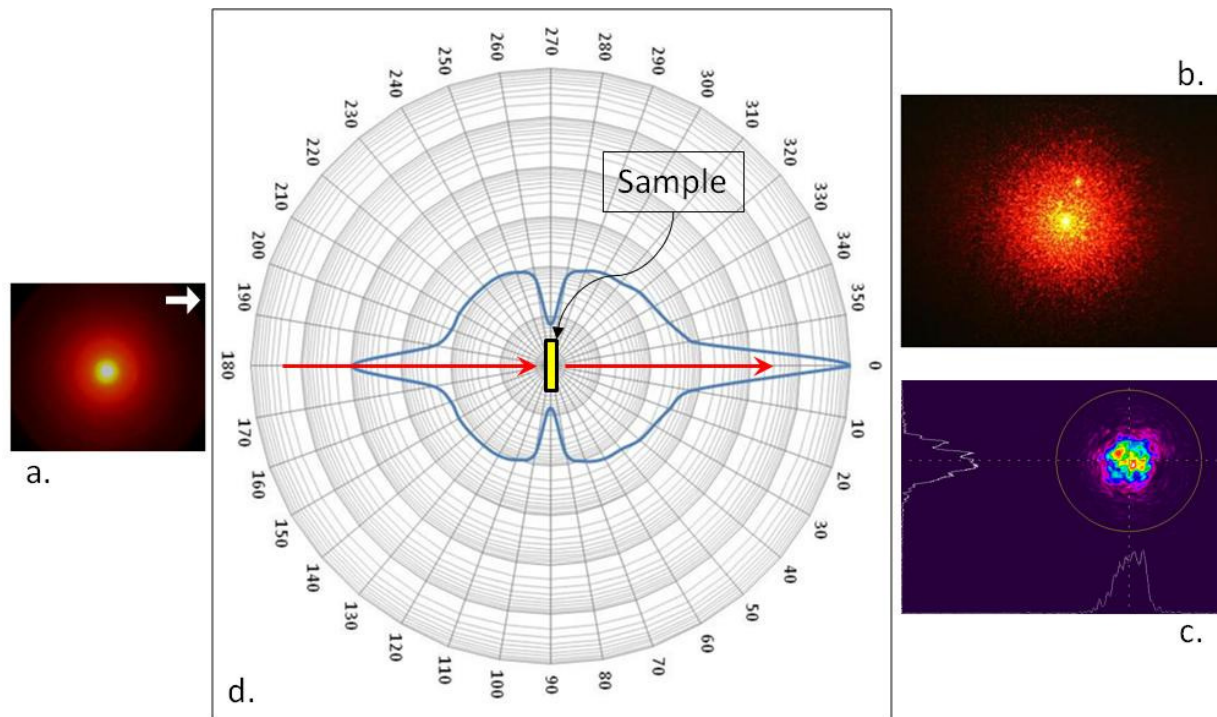
Figure 4.21: (a) Transmitted Beam before and (b) after going through the polycrystalline ceramic sample showing bulk scattering (Far Field Image), and (c) its Transmitted Beam Wavefront Distortion image. (d) The ARS intensity map for the scattered intensity in-plane about the sample.

The dynamic properties of the scattering are related to the time correlation for the resulting speckle pattern, which forms the basis of experimental techniques of intensity fluctuation spectroscopy and dynamic scattering [104]. The classical light scattering experiments for studying particles in solutions, measured the scattered light using a single detector rotated in an arc about the illuminated samples, and have become the basis of the modern static and dynamic light scattering methods used in biology [105 - 109]. Sibley studied the angular light scattering in single crystals of alkali halides, and noted that it would be possible to determine the poor regions in a given sample, as the angular spread of the scattered light and its intensity was directly influenced by it [110].

The angular spread of the scattered intensity was also explored by Peelen, to compare scattering characteristics for translucent alumina [35]. There were no observable oscillations in the scatter profiles for their samples. Schroeder et.al used a He-Ne laser line at 632.8 nm to investigate single crystal and semitransparent polycrystalline alumina (PCA or lucalox®) of different thickness [111]. They investigated the forward scattering in the angular range of $< \pm 10^{\circ}$ of the in-line transmitted beam, in the forward scattering region. They noted that the light scattered from the inhomogeneities in the material broadened the angular scatter profile.

McNamara investigated the presence of micro-voids in CVD (Chemical Vapor Deposition) grown polycrystalline diamond films, wherein it was observed that the thickness of the samples had a large effect on the scattering profile [112]. More recently, van Bruggen et.al noted that, even though the angular scattering profiles for both the small grain and large grain size PCA had a central sharp peak in the forward specular direction, the shapes of the profiles were different. The shape of the scatter profile (curvature) in the forward scatter for the large grain PCA was observed to be convex, while for the small grain ceramic was concave [113].

88

4.3.2 Materials and Methods

The setup used for the ARS measurements is shown in Figure 4.22. A tunable helium - neon (He-Ne) laser (REO Multi-Line Helium Neon Laser), selected to operate at 590 nm, was used as the plane wave light source to illuminate the sample. The wavelength selected from the tunable laser was such that it has no absorption for the samples being investigated. This removed the possibility of any absorption and emission processes which would affect the scatter measurements.

The He-Ne laser source was placed at a separate location, away from the goniometer and detector assembly to avoid stray light and interference. The laser beam was directed to the sample stage using silver mirrors. The laser was sent through a spatial filter to 'clean-up' the beam shape, and remove any higher order spatial modes and distortions from the oscillator. A mechanical blade chopper, operating at a frequency of 35 Hz was used to modulate the laser beam, and also provide the reference signal to synchronize the lock-in amplifier.

The geometry of the ARS measurement setup is shown in Figure 4.23. The entire goniometer setup was placed in a light tight box, and the measurements made in a darkened room. A mechanical rotating arm Spectrometer Goniometer from Kruss Optronic, was used in this setup. The goniometer had a 185 mm long rotation arm, with an amplified silicon detector (DET 110, Thorlabs) mounted on the end of it. The arm was moved manually, to the desired angular position, allowing the detector to measure the scattered signal about the sample (Figure 4.22). The sample was placed on the center stage of the goniometer, which had a 3-axis tripod stage. This allowed the sample faces to be aligned normal to the beam.
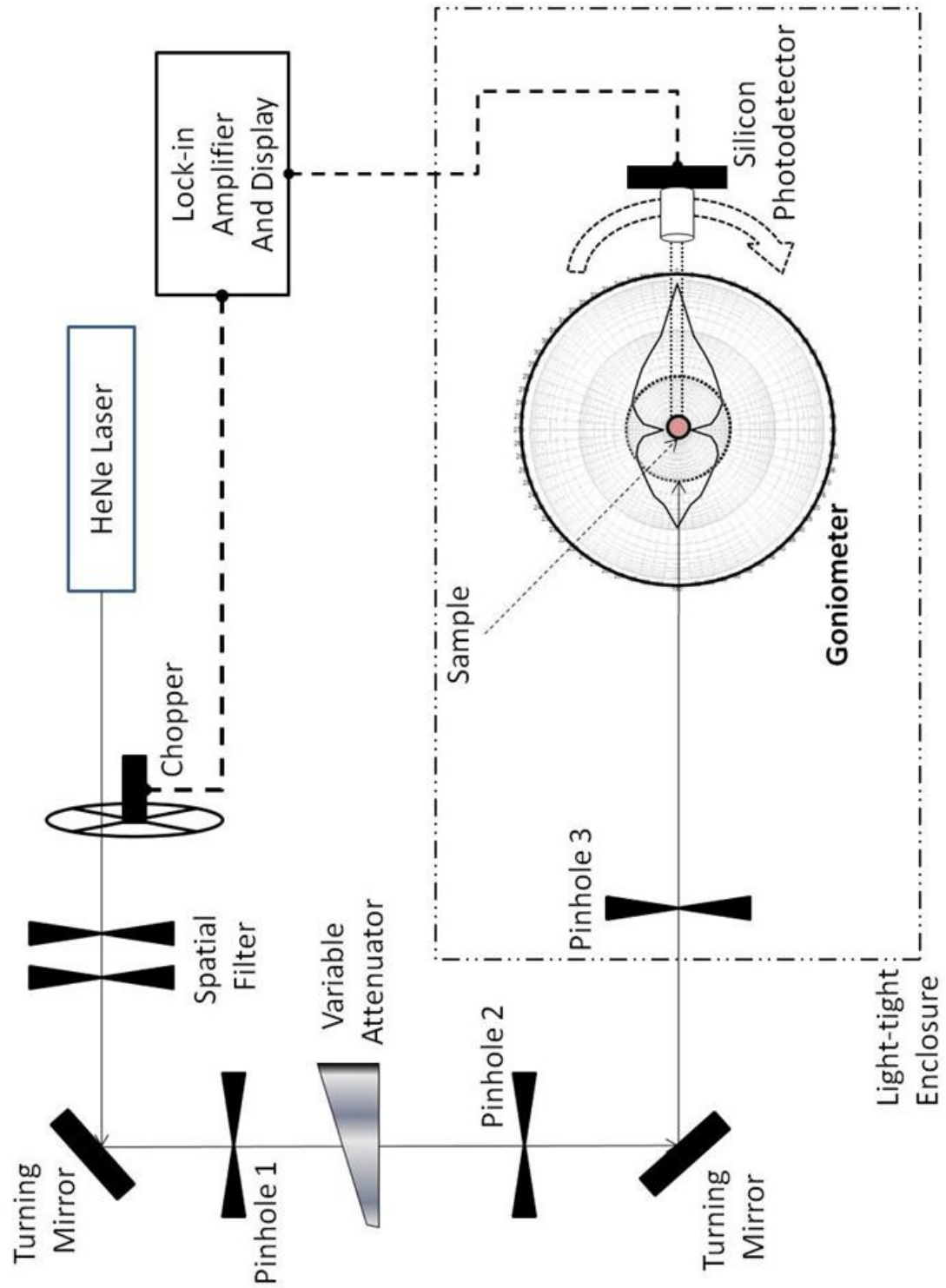
Figure 4.22: Schematic diagram of the Angle Resolved Scattering (ARS) instrument setup.

For the precise determination of angular position, the goniometer had a graduated disc with a 360° scale having divisions of 0.5°. The measurements were performed on both sides of the sample. Because of the finite size of the detector, the range was limited to ±175°, shown in Figure 4.23.

The active area of the photo detector was a square of 12.96 mm² area. The detector area became the aperture stop for the setup. Two pinholes of 2 mm diameter were placed as field stops in front of the photodetector, one 10 mm away and the other at 20 mm, as shown in Figure 4.24. The pinholes were used to reduce the stray light from to the detector. This also reduced the effective aperture of the detector to 9 mm², subtending an acceptance angle of < 1°. This defined the minimum angular step size on the goniometer, which could be used for mapping the scattered intensity around the sample.
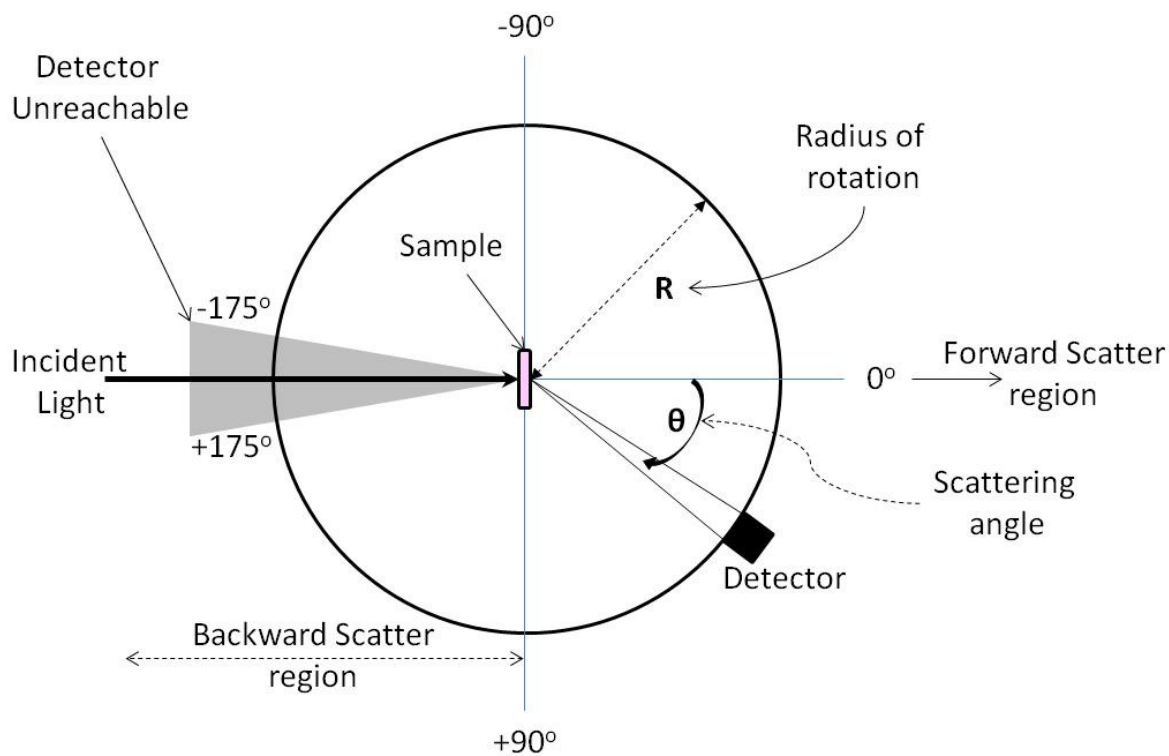
Figure 4.23: Geometry of the Angle Resolved Scattering setup

A Lock-In Amplifier (DSP SR850) from Stanford Research was used to read the signal from the silicon photodetector. Lock-in amplifiers are used to detect and measure very small AC signals. Lock-in amplifiers also increase the signal to noise ratio for the detector and prevent it from responding to stray light. The amplifier uses phase-sensitive detection to detect the signal at a specific reference frequency and phase, which is provided by the mechanical chopper.
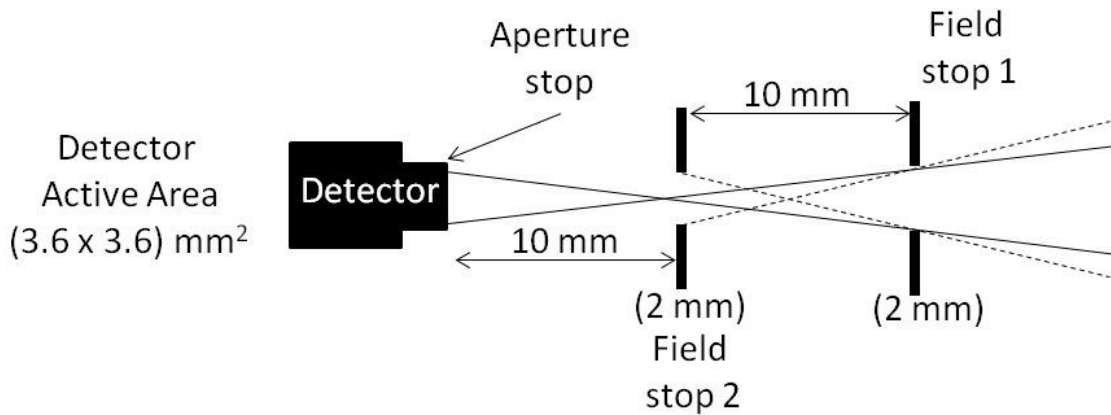
Figure 4.24: Geometry for the detector's acceptance angle
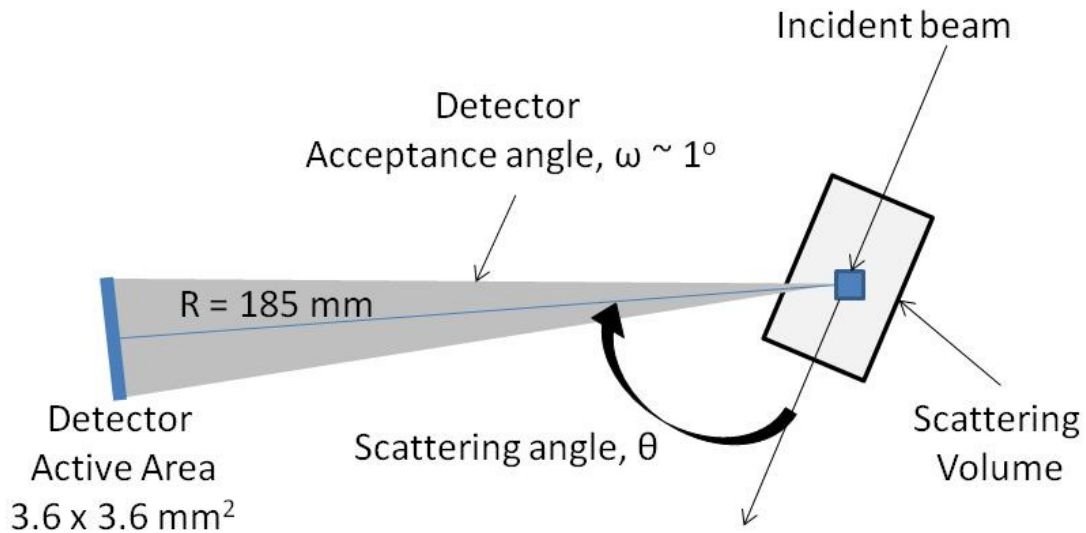
Figure 4.25: Detector setup, with field stops to minimize stray light.

The modulated laser beam allows the lock-in amplifier to measure the signal from the detector at the reference modulation frequency only. Any noise signal present at other than the reference frequency, is rejected and does not affect the measurement. The SR850 locking amplifier also has a digital phase sensitive detector, which prevents DC output errors caused by large noise signals. This allows the detection of signals from the mV to the nV range.

The incident laser beam was less than 2 mm in diameter, and the angular profile of the direct beam and the corresponding wavefront image of the direct beam are shown in Figure 4.26 (a) and (b) respectively. From the linear plot, we can see that the angular width of the beam is 2.5^o, from its peak value (at 0°) to 0.001% of the maximum value, representing 99.9% of the beam energy. The absolute scattering intensity values were not used to represent the data. Instead, the intensities in the angular pattern were expressed as a fraction of the signal recorded at the 0° scattering angle (forward specular beam). The measurements, presented after normalizing the distribution to the maximum intensity at 0°, allow the direct comparison of the scatter patterns between different samples. This also removes the variations introduced by the apparatus during the measurement process.

4.3.3 Sample Cases and Results

The scatter pattern of the undoped PLM Y_2O_3 sample (Z-203-7) is shown along with the map of the direct beam (Figure 4.26 (a)), showing the spread of the beam energy away from the 2.5^o angles from the specular beam direction (ASTM E2175-01). Figure 4.26 (c) shows the polar scatter map of two polycrystalline samples along with their TBWP images. The undoped Y_2O_3 sample (Z-203-7) does not show bulk scattering, and this is also evident from the transmitted beam wavefront image. The angle resolved scatter map for Z-302-7 shows a prominent forward peak.

93
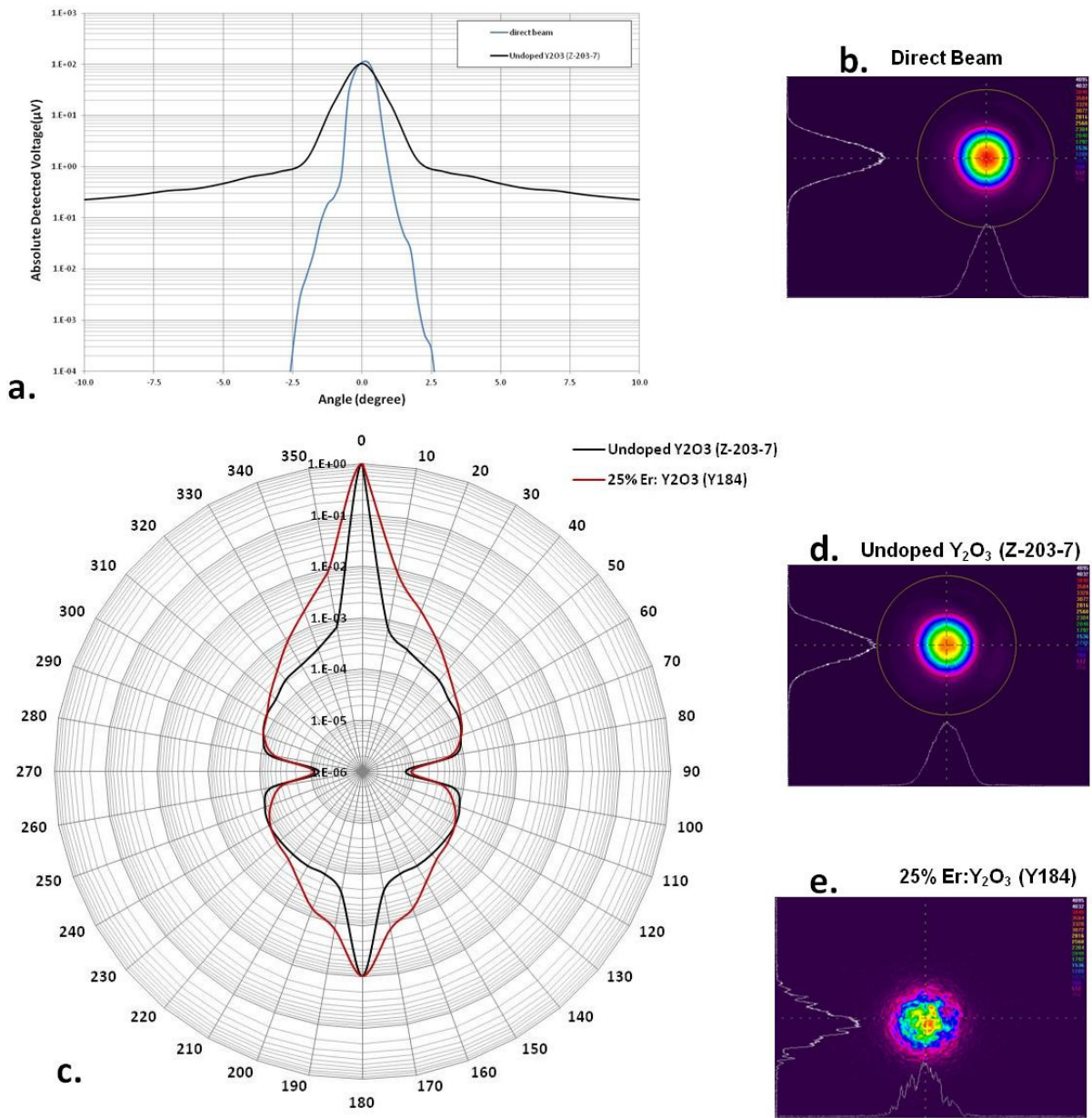
Figure 4.26: (a) Overlay of the scatter pattern of the sample Z-203-7 with the direct beam, (b) Transmitted beam wavefront image of the direct beam, (c) Comparison between the scatter profiles for two polycrystalline Ceramic: a low scattering sample Z-203-7 (undoped Y_2O_3) and a highly scattering sample (Y184, 25% $Er:Y_2O_3$). The respective wavefront distortions are shown on the right (d), (e).

The second sample, Y184 (25% Er:Y_2O_3) is of very poor optical quality, exhibiting bulk scattering. This is clearly observed from the distortions in the transmitted beam wavefront image. The angle resolved intensity map, further supports this observation. The scattered intensity is more in all angles away from the specular directions. This fits the ASTM (E2175-01) definition of haze, as mentioned before [97].

The normalized scatter intensity in the forward scatter region, obtained from angle resolved measurements are used to compare different samples. The scattered intensity in the backward lobe is not used, as a nonlinear phenomenon of the enhancement of backscatter intensity based on Anderson localization has been demonstrated in polycrystalline samples with bulk scattering [114]. This makes it difficult to isolate the reflected component from the backscattered component in the normal incidence geometry.
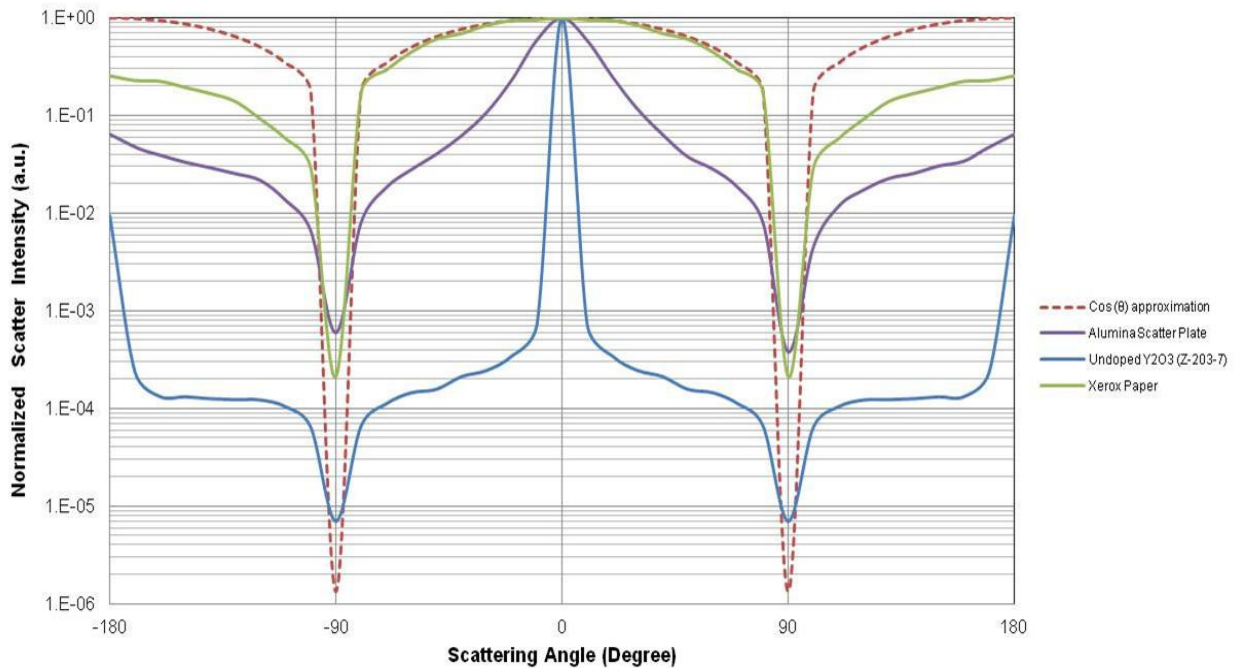
Figure 4.27: Intensity distribution pattern of a glass scatter plate, overlaid with the fit cos(θ) approximation. The scatter distribution of the sample Z-203-7 (Undoped Y_2O_3) is also plotted.

The cumulative scattered intensity is calculated from the normalized scattered intensity in the forward scattering region angles of 0° to 90°. The total scattered energy in both the forward and backscatter directions, represents the redistribution of energy from the incident beam, due to scattering from the sample. The distribution of scattered light intensity takes the energy from the narrow angular region and distributes it in all the 360° angles. This distribution is also symmetric on both sides of the specular beam, in the forward and the back scatter lobes. Hence, using the normalized intensity distribution on one side of the specular beam, between the ranges of 0° to 90° (Figure 4.29), we can calculate the cumulative scattered intensity in the forward direction.
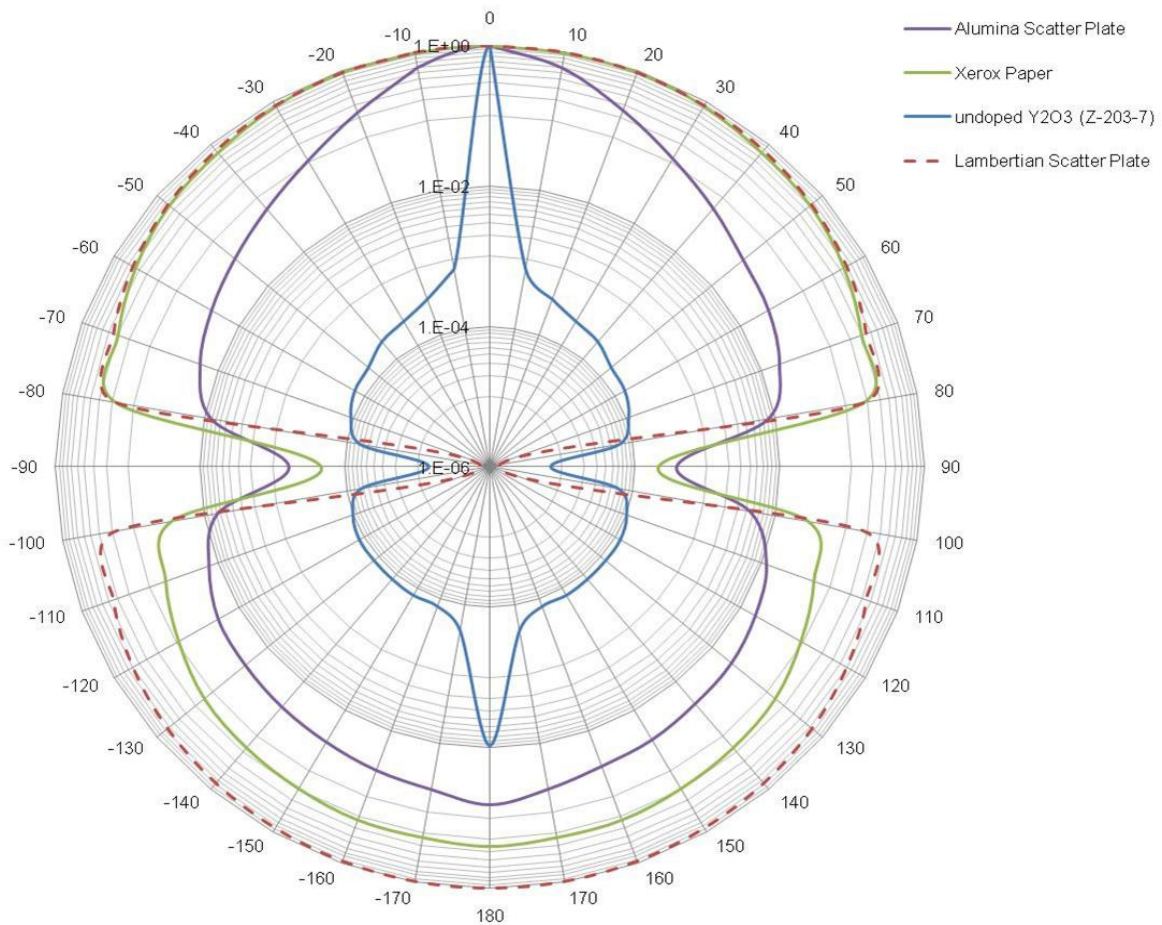
Figure 4.28: Polar plot representation for the data in Figure 4.27

This methodology is demonstrated, using a standard acid-free white paper (Xerox premier A4 printer copier paper, 60 grams), and an alumina diffuser plate, and comparing with the ideal case of a 'Lambertian' scatter. A 'Lambertian' scatter spreads the incident energy according to the Lambert's cosine law, which states that the radiant intensity ($I.d\Omega$) observed from an ideal diffuse reflector or diffused radiator of area dA, is directly proportional to the cosine of the angle (θ) between the observer's line of sight and the surface normal: $I.d\Omega.d$A.Cos(θ) [115].

The scatter pattern obtained from the alumina scatter plate is shown in Figure 4.27. A fit representing the ideal case of the Lambert's cosine law is also plotted in the same figure. It can be seen in Figure 4.28, that the intensity distribution from the alumina scatter plate lies between the Cos(θ) approximation. The scatter pattern of the Xerox paper is very close to the ideal case. The cumulative scattered intensity represents the area under the curve, and is represented as a percentage of the total area under the curve. The cumulative scattered intensity for the glass scatter plate is shown in Figure 4.30.

The cumulative scattered intensity plot can be understood using two (theoretical) ideal cases: one of a perfectly isotropic scatter system (Lambertian Scatter plate), and the other of a system with no scattering. By looking in the forward scatter region and calculating the cumulative scattered intensity, it is possible to compare samples that have similar transmitted beam wavefront distortion. This plot describes the total energy conservation associated with the scattering process. This gives us the working space, for comparing different samples and, determining the extent of scattering being observed for the samples.
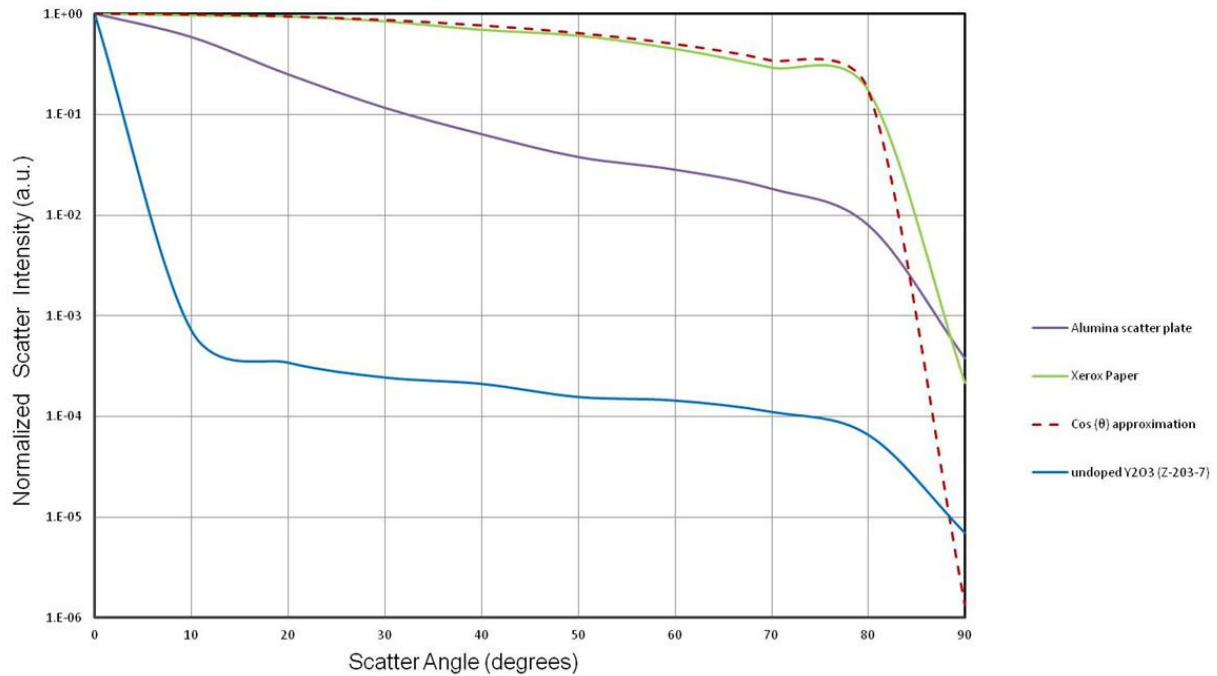
Figure 4.29: Intensity distribution pattern between angle ranges of 0° to 90° for a glass scatter plate, overlaid with the fit Cos(θ) approximation. The scatter distribution of the sample Z-203-7 (Undoped Y_2O_3) is also plotted.
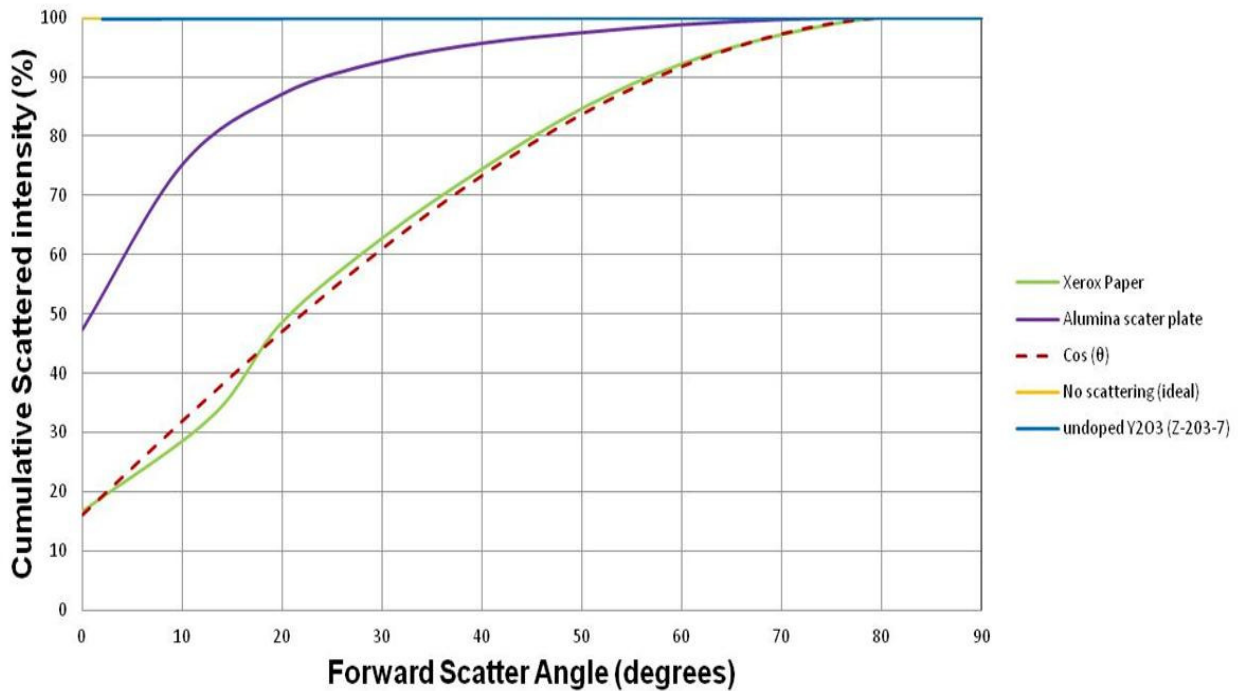
Figure 4.30: Cumulative scattered intensity for the glass scatter plate, along with the integrated value for the Cos(θ) fit. The magnified view of the cumulative scattered intensity for Z-203-7 is shown on the right.

In the case of the ideal isotropic scatter distribution, the scattered intensity is equal for all angles; hence the cumulative scattered intensity is represented as a linear line, with a constant slope of 1. For the second ideal case of no scattering, all the intensity is at $0°$, hence the cumulative scattered intensity is a linear line parallel to the x-axis with a slope of zero and an intercept at 100%, as shown in Figure 4.30.

This creates the operating region for the analysis of the scatter distributions for different samples. In the case of the glass scatter plate, the cumulative intensity is close to the ideal isotropic scatter case, where as for the undoped Y_2O_3 polycrystalline sample (Z-203-7), the distribution is closer to that of the no-scattering region.

This ideology is now applied to two sample sets of PLM materials. The first sample set is of two identical polycrystalline samples from the 'cutback samples' as described in section 4.2. The second set is of three Er:Y_2O_3 samples with different erbium concentrations. For the first set, two PLM 0.9% Nd:YAG samples of different length: B3 (2.73 mm), and B6 (22 mm) were studied. The angle resolved scatter pattern for the two samples is shown in Figure 4.31. The scatter pattern for the thicker sample (B6), shows a larger spread of intensity on either side of the specular beam direction, compared to the thinner sample (B3).

This points to a cumulative effect of more bulk scattering in the longer sample, compared to the thinner sample. The same is also reflected in the transmitted beam wavefront images for the samples. The sample with a longer path length (B6), introduces more distortions, compared to the thinner sample (B3) which has a smaller path length. The normalized intensity distribution for the samples B3 and B6 are shown on a polar plot (Figure 4.32).

99
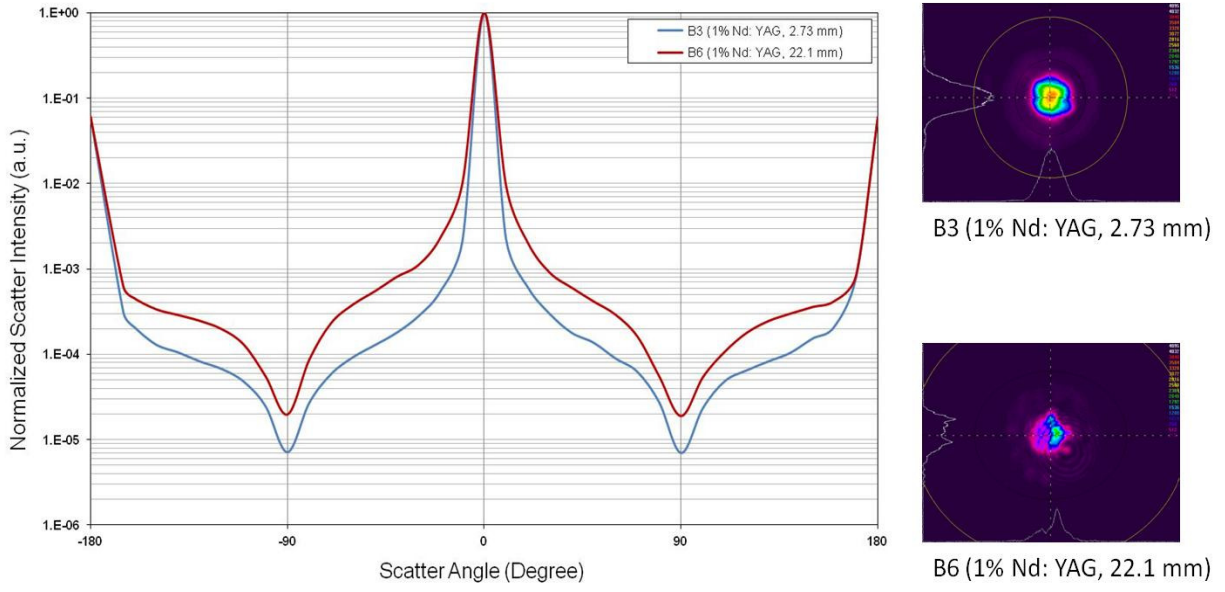
Figure 4.31: Scatter distribution for samples B3 and B6 on linear scale. The corresponding beam wavefront images are shown on the right
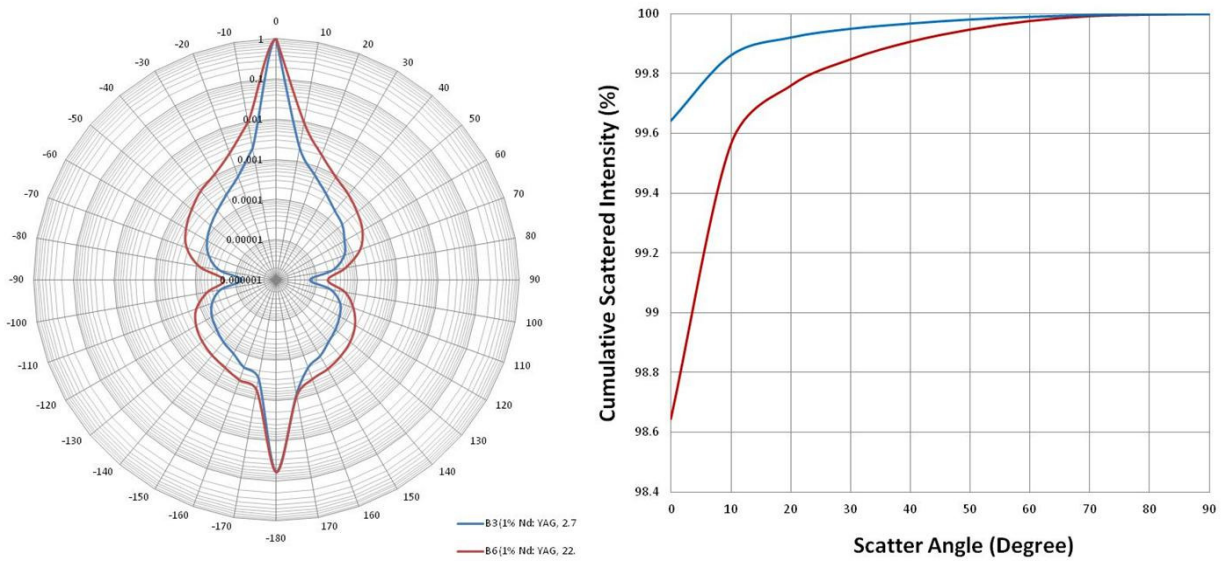
Figure 4.32: (a) Angular scatter distribution for samples B3 and B6, on a polar map. (b) The cumulative scattered intensity in the forward scatter region is shown on the right.

Comparing the distribution of intensity for both the samples, we observe that between the angles of 10° to 170°, the longer sample (B6) has a higher scattered intensity than the thinner sample (B3). The Plot of the cumulative scattered intensity (Figure 4.32 (b)) for the forward scatter beam between the angles of 0° to 90° for the two 0.9% Nd:YAG samples (B3 and B6), shows the same effect, where sample B6 has a higher scattered intensity distribution compared to sample B3.

The second sample set consisted of three polycrystalline samples with different concentrations of erbium: 0.5% $Er:Y_2O_3$ (Y990-2), 5% $Er:Y_2O_3$ (Y993-2) and 50% $Er:Y_2O_3$ (Y996-2). The thickness of all the three samples was 4 mm, hence the optical path lengths for the laser beam through the three samples was the same. The angle resolved scatter distribution and the transmitted beam wavefront profiles for these three samples are shown in Figure 4.33.

It can be seen that the wavefront images for the three samples are very similar, but the angle resolved measurements show the variations in the spatial distribution of the scattered intensity for the three samples, as shown in Figure 4.34.

The scattered intensity for the beam in the forward scatter direction between the angles of 10° to 90° is used to calculate the cumulative intensity distribution for the three samples. From this, we are able to identify that the sample Y993-2 (5% $Er:Y_2O_3$) is the worst among the three, and the sample Y996-2 (50% $Er:Y_2O_3$) has the least scattered intensity away from the specular beam.
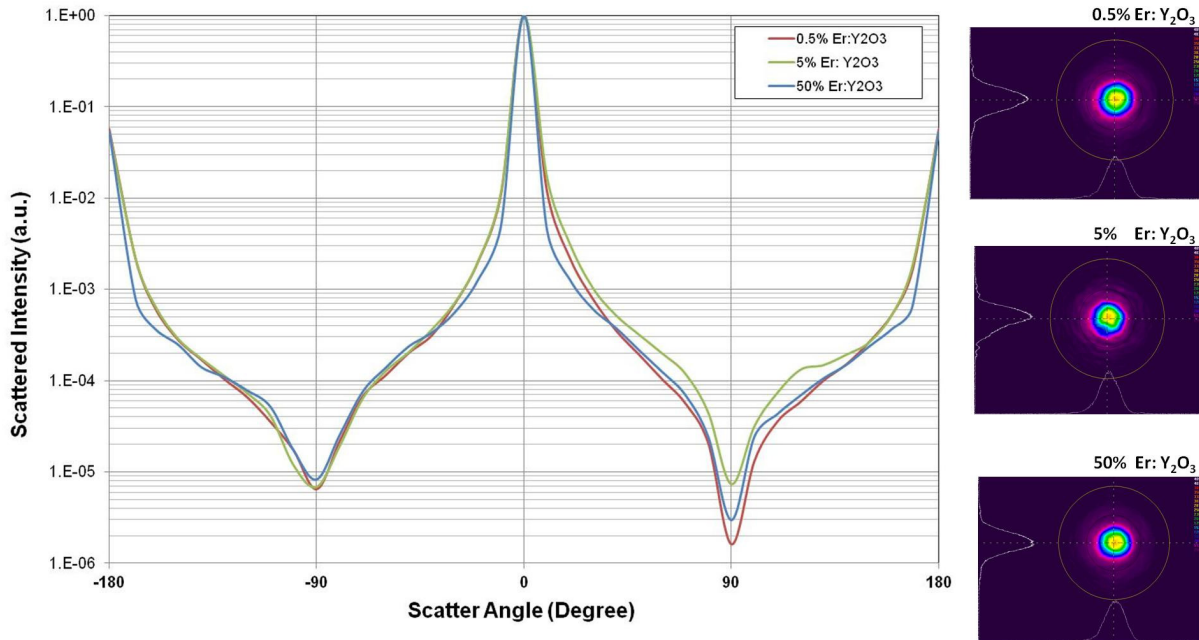
Figure 4.33: Scatter distribution for the three erbium doped yttria samples on a linear scale. The corresponding beam wavefront images are shown on the right.
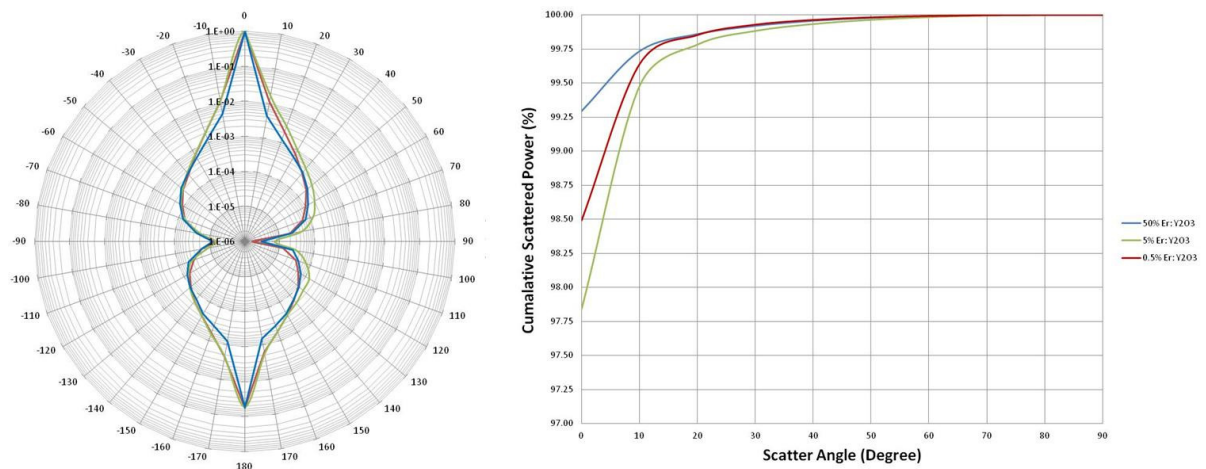
Figure 4.34: (a) Angular scatter distribution for the three erbium doped yttria samples on a polar plot. (b) The cumulative scattered intensity in the forward scatter region is shown on the right.

4.3.3 Discussion on Angle Resolved Scattering

Bulk scattering leads to the distortion of the transmitted beam along the specular direction. This distortion, which can be imaged in the forward direction, using the methodology described in the previous section (4.2), shows the effect of bulk scattering in the specular directions. In 'poor' samples, the distortions due to bulk scattering in the transmitted beam are clearly indicative of the severity of the refractive index inhomogeneities, and can be easily identified. For better quality laser materials, it is difficult to identify and compare samples, which show very little distortion in the transmitted beam profile.

The Angle Resolved Scattering (ARS) measurements map the scattered light about a sample. The intensity of the scattered light in turn represents the presence of bulk scattering in the sample, and is used to compare the different samples. The ARS measurement presented in this section is based on a rotating goniometer. The samples are illuminated using a laser beam, normal to the sample surface and the scattered light is measured.

To compare different samples, the scattered intensity is mapped on a polar plot which is further used to calculate the cumulative scattered intensity for comparison. Comparison among (more than two) a high quality and poor quality polycrystalline PLM samples highlight the applicability of the technique. Two different lengths of a poor quality Nd:YAG samples were compared to highlight the effect of length on bulk scattering, where the longer sample showed a broader spread of scattered light away from the specular direction. Finally, this method was applied to compare three high quality PLM Er:Y_2O_3 samples, which showed similar transmitted beam profiles, to identify which sample had least bulk scattering.

4.4   Schlieren Imaging

4.4.1   Introduction

For single crystal laser materials, the inhomogeneities introduced during the Czochralski growth of the solid material from the melt, are usually attributed to variation in composition, density, and mechanical stresses created as the melt solidifies to create the single crystal (Figure 1.1 (a), (b) and (c)). For a PLM, the source of bulk scattering is the variation in the refractive index attributed to the presence of scattering centers like pores, voids, disordered and secondary phase at the grain boundaries. Bulk scattering is manifested by a reduction of the inline transmission and distortions to the propagating wave front (section 4.3).

In the present effort, the methods used to investigate bulk scattering in PLMs are based on inference where the effects of bulk scattering in the material are detected by imaging resolution lines on a test pattern (section 4.1), recording the beam distortion as the laser beam propagates through the material (section 4.2), and mapping the spatial distribution of scattered intensity (section 4.3). In addition, all these methods probe a very small section of the sample at a time. Analyzing an entire sample by raster-scanning is logistically difficult in terms of handling the large amounts of data that would be generated (and subsequently would have to be interpreted), time consuming and costly.

To date, there is no reported technique that can directly, quickly and cost effectively image the variations in the refractive index on the scale of an entire sample (especially if the sample is more than a few square millimeters in size). Schlieren imaging, a technique which inherently *requires* variations in the refractive index (albeit small variations) in order to visualize an effect, is one method that was thought to be suitable for addressing the above stated problem.

104

4.4.2 Schlieren Imaging Theory

Schlieren (from German; singular "Schliere", meaning "streak") is defined as gradient disturbances or inhomogeneities in the refractive index distribution in (most commonly inhomogeneous) transparent media, which may or may not be visible to the human eye [116 - 119]. Historically, Schlieren imaging has been applied towards imaging small refractive index variations in various types of materials, like biological samples [116], transparent liquids [120] and rarified gases [119]. Shadowgraphs were the first method developed to image the non-uniformities in the transparent materials and most commonly to image the variations in rarified gases.

Schlieren were first observed by Robert Hooke in 1665, using a large convex lens and two candles to project a parallel beam of light [117, 118]. Using one of the candles to serve as a light source, a shadow or Schliere of the warm air rising from the second candle was projected on a screen. Shadowgraphy used the interference effects between the optical path differences to create light and dark variations on a screen.

The conventional Schlieren system is credited mostly to German physicist, August Toepler, which was designed to detect defects in glass for making lenses [120, 122]. In Toeplers' Schlieren system, a point light source was used to illuminate the test object containing the Schliere. The light source projected the shadow of the test object with varying density on to a screen. The refractive index variations were imaged as shadows in the transmitted light. The light rays from the point source are refracted while passing through the test object and deflected from their natural path. Shadows are created on the screen, where the rays are deflected, and all other positions appear brighter. This creates a pattern of variations in illumination or contrast on the recording plane [120, 122].

The white light Schlieren imaging (or phase contrast imaging) was more recently used by Alfred Vogel for imaging the density variations at the liquid-vapor interface to study tissue-ablation dynamics using a pulsed laser [121]. The white light Schlieren imaging that Vogel examined, used a collimated light source to illuminate the object, and an edge filter as the Schlieren filter, which makes it possible to image the spatial variations in the refractive index which are the cause of bulk scattering loss in a transparent material over the entire cross-sectional area of the sample. Figure 4.35 shows the basic setup utilized for the white light Schlieren imaging. An image of the sample is formed using a converging lens, which is also called the primary imaging lens or Schlieren lens. This image is located at the conjugate distance to the lens according to the thin lens equation:

$$\frac{1}{f} = \frac{1}{d_o} + \frac{1}{d_i} \tag{51}$$

Where f is the focal length of the imaging lens, d_o is the distance from the object to the lens and d_i is the distance from the image (of the object) to the lens.
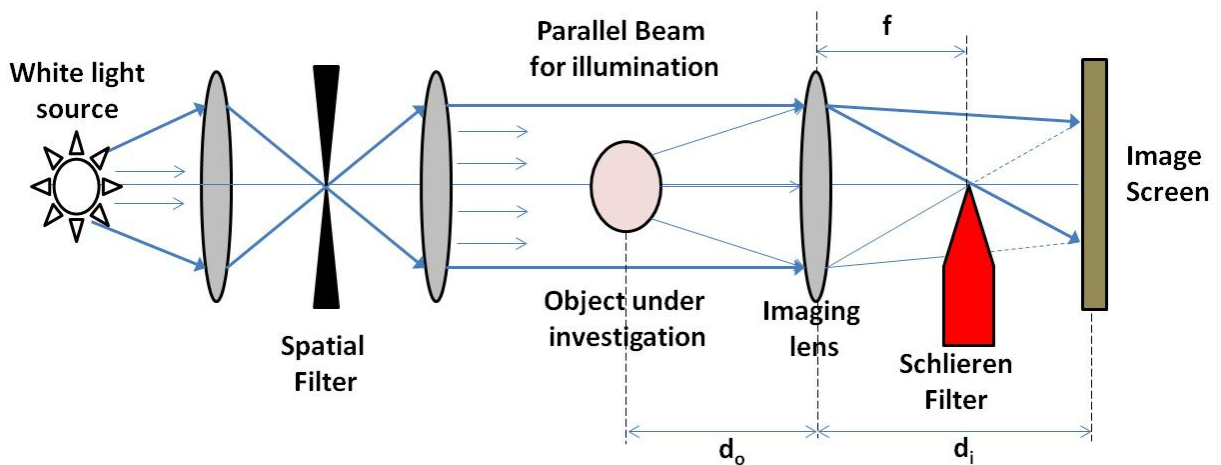
Figure 4.35: Schematic of the white light Schlieren imaging apparatus

The viewing screen is located at a conjugate distance from the plane of the Schlieren lens. A knife-edge located at the focal length of the lens, is positioned so as to partially block some of the light from reaching the imaging screen. The knife-edge cutoff is varied from 0% to 100 %, which leads to a reduction in the illumination of the image gradually from 100% to 0%.

The knife-edge technique produces information on the sign of the phase gradients (deflection of light). Deflection in the upward direction increases illumination, because more light passes the filter, and deflection in the opposite direction results in darkening. The objects under investigation thus appear to have an orange-peel texture or a relief-like appearance, in the Schlieren image. This reflects the variations in the refractive indices in the object, which is easily interpretable.

The change in brightness is proportional to the amount of deflection and inversely proportional to the width of the illumination slit. Thus an extended light source yields a large dynamic range while a small slit results in high sensitivity (at the cost of dynamic range). Usually, the knife-edge blocks more than half of the non-deflected light, and a large cutoff (> 80%) increase in the sensitivity of the knife-edge technique, but deteriorates the image resolution.

4.4.3 Materials and Methods

The white light Schlieren setup shown in Figure 4.36 is a modified version of the setup used by Vogel [121] in that the setup used to evaluate PLMs was simpler and faster to use and had the advantage of being able to image _any_ size sample limited by the field of view, in a single image capture. Since surface contaminants and bulk inhomogeneities both show up as index variations in Schlieren images, some attention to detail for sample surface preparation is

required. As such, the sample surfaces that the Schlieren image was taken across were polished to laser quality finish to remove any contribution from surface defects. To remove any dust, oils and residues from the surfaces, the samples were cleaned with solvents (acetone, methanol, IPA). Any major surface scratches and large defects are projected as dark shadows with no contrast in the image. It is also possible to adjust the focus of the imaging lenses to change the depth of focus as a means to minimize the effect of both surface scratches and contaminants.

The entire Schlieren Imaging setup (Figure 4.36) was enclosed in a light tight box to minimize the background stray light. The light source, spatial filters and the Schlieren filter used in the present setup were line shapes. The Schlieren images obtained from the setup in Figure 4.36 show the variations in the refractive index across the bulk of the transparent polycrystalline ceramic laser gain media.

The samples were illuminated using a high pressure W-halogen filament bulb (Figure 4.36(a)), operated at 12V DC at 5A current. The bulb was chosen such that the filament was in the shape of a line, and imaged as a line profile in the far field. The collimator lens (L1) was a commercial SLR (Canon 50 mm (1:1.4)) achromatic lens, 32 mm in diameter and placed 128 mm from the light bulb (Figure 4.36(b)).

A spatial filter, in the form of a 1 cm wide variable-width slit aperture, was placed at distance of 100 mm from the collimator lens (Figure 4.36(c)). It was important to match the shape of the filament to the spatial filter to obtain linear control over brightness. The slit aperture of the spatial filter was oriented to be parallel to the long axis of the bulb filament and was controlled by a micrometer. The width of the slit was used to vary the brightness of the light source so as to get the desired level of illumination at the final imaging plane.
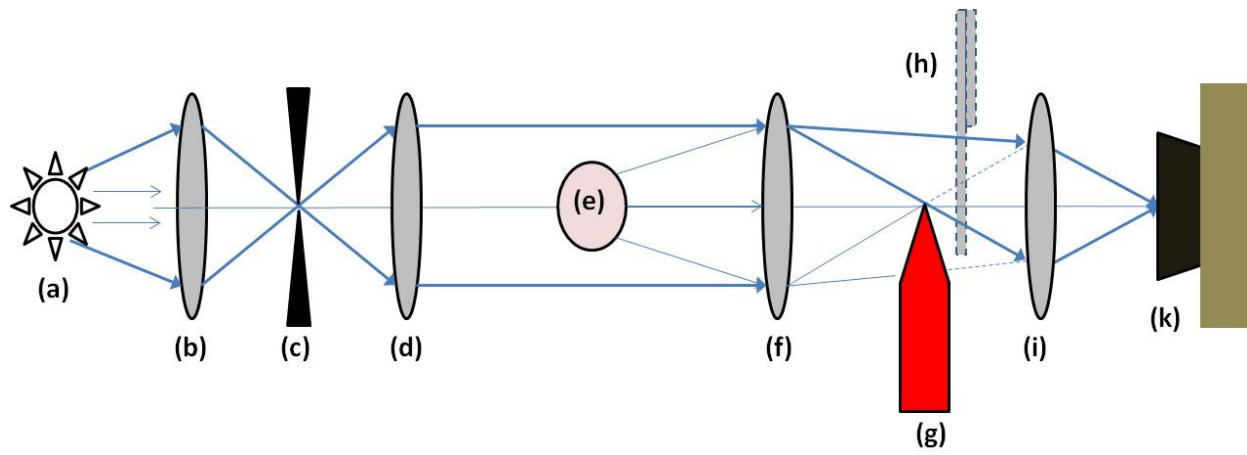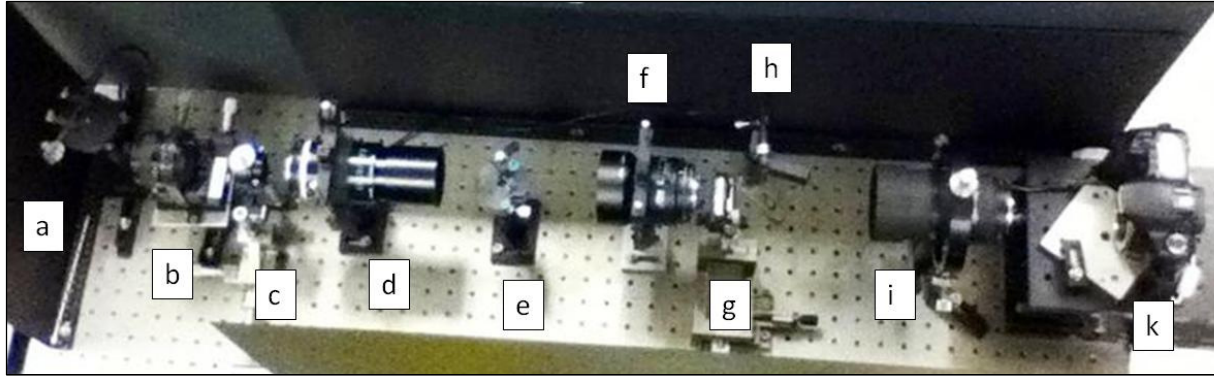
Figure 4.36: (top) Photo of the white light Schlieren apparatus. (Bottom) Schematic of the white light Schlieren imaging apparatus. (a) Light source, (b) collimator lens (L1), (c) Spatial Filter, (d) condenser lens (L2), (e) Object under Investigation, (f) primary focusing lens (L3), (g) Schlieren Filter, (h) Silicon Photo detector, (i) secondary imaging lens (L4), (k) Digital camera.

A Nikon 105 mm (1:4)) SLR achromatic lens was used as the condenser lens (L2), and positioned at 100 mm from the exit aperture of the spatial filter (Figure 4.36 (d)). The condenser lens L2 was used to project a collimated (parallel) beam to illuminate the sample, which was placed at a distance of 180 mm from the lens L2. The samples, (Figure 4.36 (e)) were placed on a 5-axis stage, which allowed the alignment and rotation, to keep them normal to the collimated beam from the condenser lens L2. A Nikon 85 mm (1:1.8) SLR lens (Figure 4.36 (f)), was used as the primary focusing lens (L3).

The primary focusing lens (L3) was used to create an image of the sample, at an adjustable distance between 75 mm – 85 mm depending on the dimensions of the sample being imaged. The Schlieren filter (Figure 4.36 (g)), was placed at the focus of the primary focusing lens L3. A straight edge filter was used in this setup as the Schlieren filter. A 2-inch wide steel blade, with a sharp edge was used as the edge filter to block the beam. The blade was inspected to be free of any chips and damage and also straightness of the edge. The filter was mounted on a 3-axis stage, to allow repeatable placement of the blade at the location of the image at the focal point of the condenser lens L3. A large area (10 mm x 10 mm) silicon photodiode sensor was placed at 50 mm from the focus of the condenser lens. The photodiode was used to measure the intensity of light, and determine the cutoff being introduced by the Schlieren filter. By measuring the intensity of the light, the percentage of the light blocked by the Schlieren filter was calculated.

A Nikon 105 mm (1:2) SLR lens was used as the secondary imaging lens (L4). The secondary lens was placed at 230 mm from the Schlieren filter. It was used to create the final image of the sample on to the detector. The detector used was a standard Canon 30D DSLR (digital single lens reflex) camera. The digital camera had a 14 megapixel CCD sensor, with a UV-IR filter to image only in the visible spectrum. The camera was connected to a computer, so the images taken could be viewed on a large screen while adjustments were made to the setup prior to taking the images. Sample images, obtained from the described setup, comparing Schlieren images and beam profiles for, a high quality single crystal and high quality PLM and a poor quality PLM sample are shown in Figure 4.37 to Figure 4.39. The bright field image, look the same for all the three samples, but the Schlieren images bring out the refractive index inhomogeneities in the poor sample.
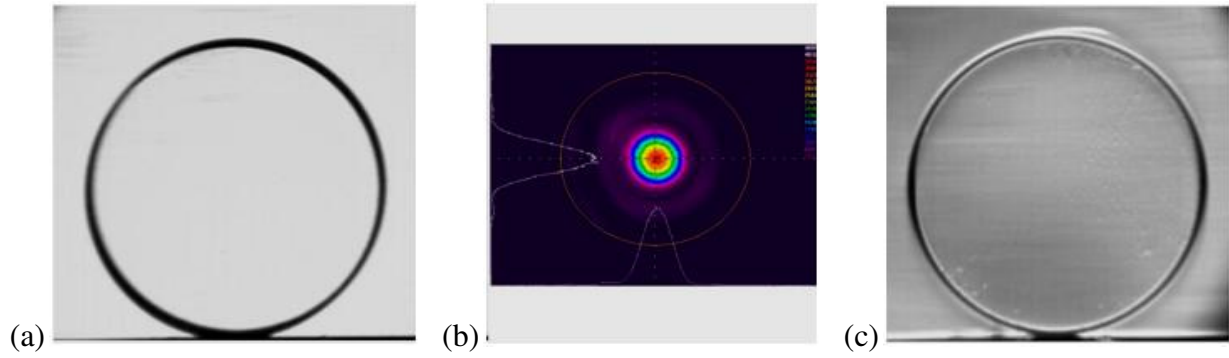
Figure 4.37: High quality single crystal YAG sample (a) The bright field image (b) Transmitted Beam Wavefront Profile through the sample, and (c) Schlieren image
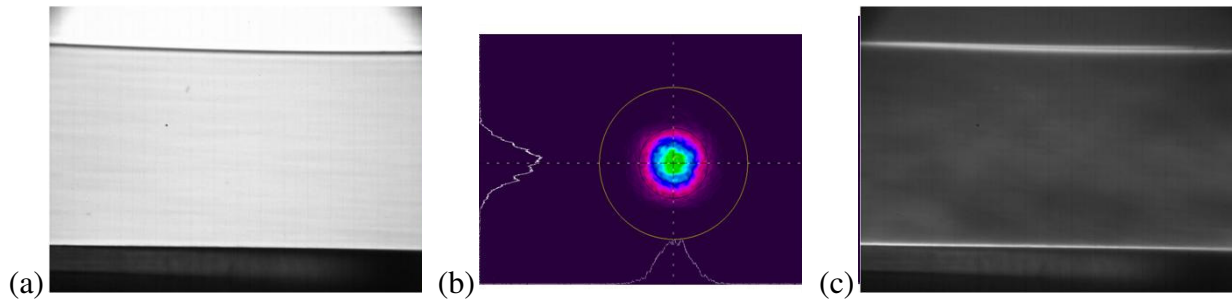
Figure 4.38: High quality polycrystalline sample (R80085) (a) The bright field image. (b) Transmitted Beam Wavefront Profile through the sample, and (c) Schlieren image. The curvature in the edge of the sample is an artifact from the camera lens.
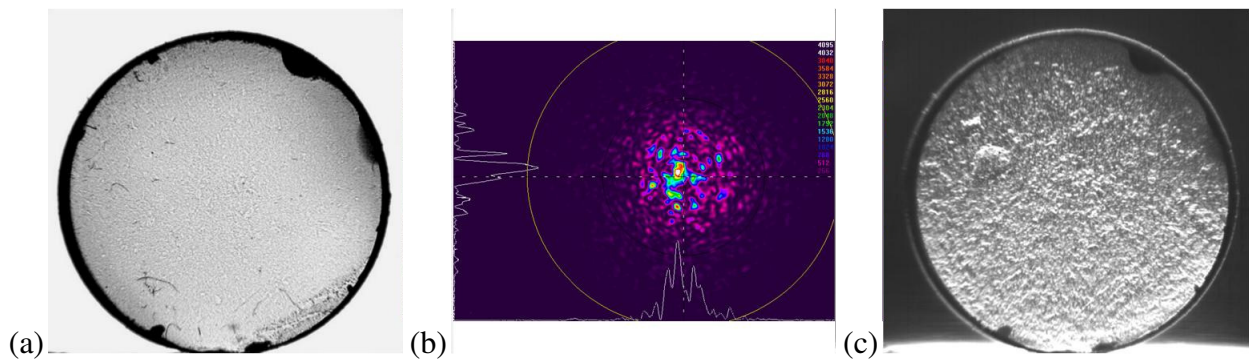
Figure 4.39: Poor quality polycrystalline sample (sample Y183) (a) The bright field image, (b) Transmitted Beam Wavefront Profile through the sample, and (c) Schlieren image.

4.4.4 Schlieren Imaging Methodology

The method of recording the Schlieren images of the PLM samples is a 4 step process.

1. Recording the bright field image of the sample (0% cutoff).

2. Recording the dark field image of the sample (100% cutoff)

3. Schlieren image of the sample taken at the same cutoff positions for comparison. The optimum cutoff point depends on the extent of inhomogeneities present in the given sample.

4. Background image recorded, by taking the sample out of the beam and keeping the imaging conditions constant. The background image is further used in image processing for subtraction to define the image zero level.

In the first step, the samples is imaged in bright field, where "bright field" image is referred to imaging the sample with the camera and the Schlieren filter not blocking the light and is completely out of the beam path. The silicon photo detector is used to determine the intensity of the light being blocked by the Schlieren filter. The bright field intensity is used as the 100% point, to measure the cutoff for obtaining the Schlieren image for the given sample.

Next, the Schlieren filter is moved in to completely block the beam and create a shadow on the detector. This blocked location for the Schlieren filter is taken as the 0% point. Ideally, at this point the signal intensity on the silicon detector should be zero, but in many cases, due to some light leakage and ambient light, the intensity is higher than zero. The distances on the micrometer between the 100% and 0% points are dependent on the light intensity measured by the silicon photo detector are calibrated for each sample.

Once the 100% and 0% positions for a given sample are determined, the Schlieren cutoff position for the filter can be determined. To obtain the Schlieren image of the sample, the Schlieren filter is moved into the beam slowly, while continuously monitoring the image on the camera. This usually also requires adjustment of the position of Schlieren filter to a new focal point. This is to compensate for the path difference introduced in the beam by the sample's refractive index. For each sample, the image is optimized to achieve a high contrast by adjusting the cut-in position of the Schlieren filter.

As the response of the human eye is logarithmic, the process of determining the optimized image by visual inspection is usually inconsistent. To avoid this non-linearity in response, the photodetector is used to determine the cutoff position. The brightness change in the image is proportional to the amount of deflection caused due to the refractive index variations, and the amount of light blocked by the Schlieren filter.

The Schlieren filter is gradually moved into the beam (increasing the cutoff), until only the deflected parts of the beam are being imaged. At the desired contrast, which varies with different samples, the Schlieren images are recorded. Most of the Schlieren images are obtained at the 75% or higher values of cutoff. For poorer samples, this number is closer to 70 %, while for good samples the cutoff number is close to 90 %.

This sequence, along with an approximate knife-edge cutoff amount, is depicted in Figure 4.40, by imaging a poor quality transparent polycrystalline ceramic Y_2O_3 sample. The Schlieren image is selected at a suitable position between 70% to 85% of the cutoff position for the Schlieren filter (75% is selected as optimum).
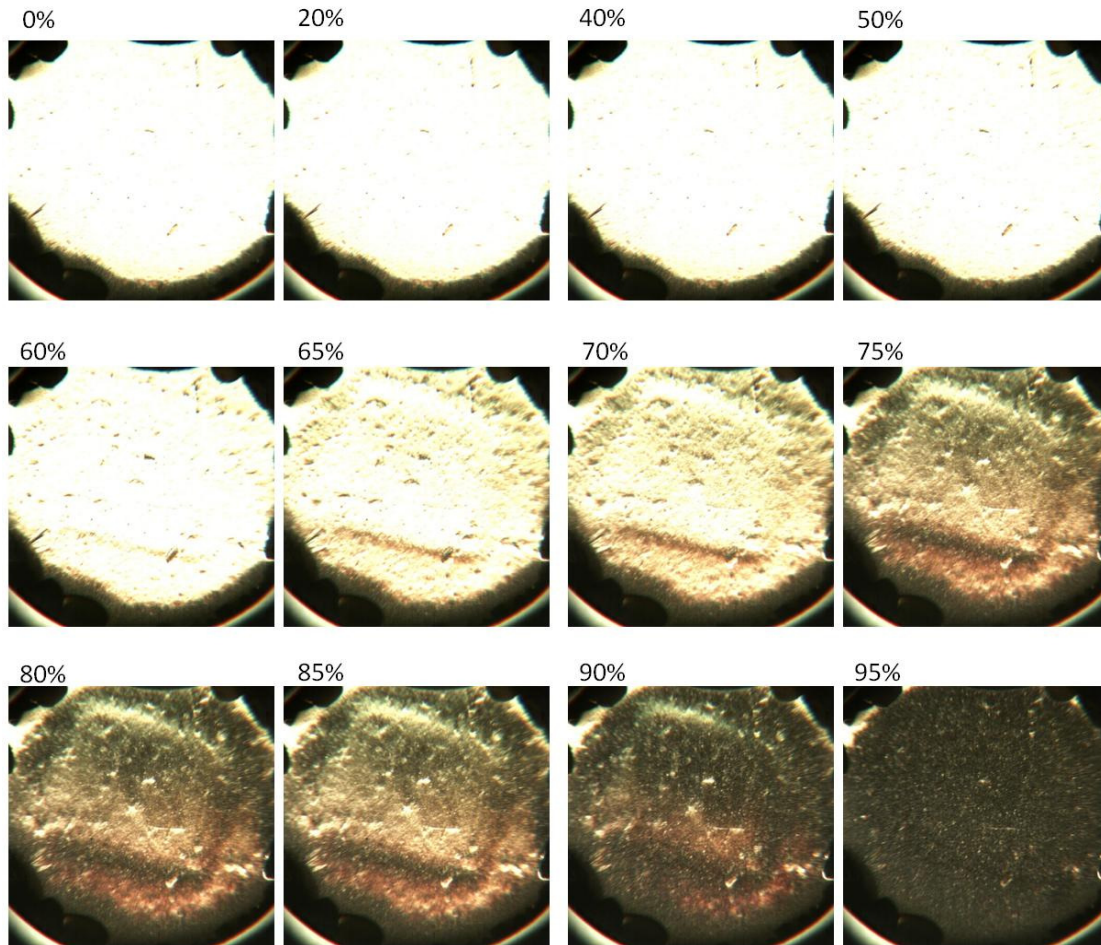
Figure 4.40: Sequence of Schlieren images taken at increasing cutoff positions of the filter. The cutoff is indicated by the percentage of light being blocked. The optimum Schlieren image is taken at around the 75% cutoff position.

4.4.5   Schlieren Image Analysis

Lightness (sometimes called value or tone) is a property of a color, or a dimension of a color space, that is defined in a way to reflect the subjective brightness perception of a color for humans along a lightness–darkness axis [123, 124]. An image histogram is a type of histogram that acts as a graphical representation of the tonal distribution in a digital image. The histogram plots the number of pixels in the image (vertical axis) with a particular brightness value (horizontal axis) [124].

The following is the methodology used for analysis of the Schlieren images obtained for the PLM samples. First, the Schlieren image of the PLM sample is taken at a given cutoff point. Next, the background is subtracted from it to just represent only the image of the sample, showing the refractive index variations. The image is not modified in any image processing software. All images are taken by the camera at [+0] image saturation level, from the range of [-3, under-exposed] to [+3, over-exposed]. The image is then converted from RGB to 24 bit grayscale. The hue (color) and saturation information is eliminated while retaining the luminance or tone (from the weighted average of the three color channels) for intensity analysis [124].

The image as taken by the camera is in 24 bit grayscale, as MATLAB can only process 16 bit grey scale images, hence there is a loss of resolution during the conversion from one format to another. The 2-D Schlieren (16 bit grey-scale) image is used to create a false-color projection of the refractive index. This image is further used to extract a histogram of the intensity variations across the whole 2-D image. This histogram shows the distribution in the variations in the value of the pixels in the image. For a homogeneous sample, with small refractive index variations, the histogram has a very narrow distribution, whereas for a sample with large refractive index variations, the distribution has a larger spread. The intensity histogram shows the distribution of the pixel intensity values or the luminance for a grey scale image. For a given image, it plots the tonal distribution in the image as a number of pixels on the vertical axis, against the intensity values on the horizontal axis.

The MATLAB command, imhist(i) displays a histogram for the image "i" above a grayscale color bar. The number of bins in the histogram is specified by the image type. For "i" being a 8-bit grayscale image, imhist() uses a default value of 256 bins. For the 16-bit grey-scale

115

image, the histogram plots the number of pixels for the tonal value, ranging from 0 to 255. In the tonal distribution of the image, black color is represented by a value of 0, white color by 255, and the values in between represents the grey-scale color. The horizontal axis of the graph represents the tonal variations, while the vertical axis represents the number of pixels in that particular tone [124]. By examining the histogram for a specific Schlieren image, a viewer is able to judge the entire tonal distribution at a glance.

The left side of the horizontal axis represents the black and dark areas, the middle represents medium grey and the right hand side represents light and pure white areas. The vertical axis represents the size of the area that is captured in each one of these zones. Thus, the histogram for a very dark image will have the majority of its data points on the left side of the center (128) of the graph. Conversely, the histogram for a very bright image with few dark areas and/or shadows will have most of its data points on the right side and center of the graph. The Schlieren image is a representation or a map of the variation in the refractive index in the sample. The idea of the Schlieren image analysis is to ascertain the quality (good vs. poor) of the transparent PC laser material, by imaging the distribution of the refractive index across the sample.

4.4.6 Sample Cases and Results

Case 1-a: High Quality Sample

A good quality sample (Single crystal undoped YAG) has a uniform distribution of refractive index across the whole sample. The bright field and the Schlieren images are shown in Figure 4.41 (a) and (b), respectively. The bright field image shows no distortions or intensity variation across the sample (Figure 4.41 (a)). The Schlieren image has a grey tone, with a uniform distribution of intensity across the samples' dimensions (Figure 4.41 (b))

The Schlieren image shows no intensity variations or intensity contrast, and no localized defects are observed in any location in the body of the single crystal sample. From the Schlieren image, a section of the image, represented by the red square, was used to perform image analysis using the process described in section 4.4.5. From the analysis of the Schlieren image, a false color image, highlighting the variation in the image tone was plotted (Figure 4.41 (d)). Furthermore, an intensity histogram of the normalized Schlieren image was plotted, shown in Figure 4.41 (e). The intensity histogram plots the distribution of the pixels in the selected image, according to their tonal value.
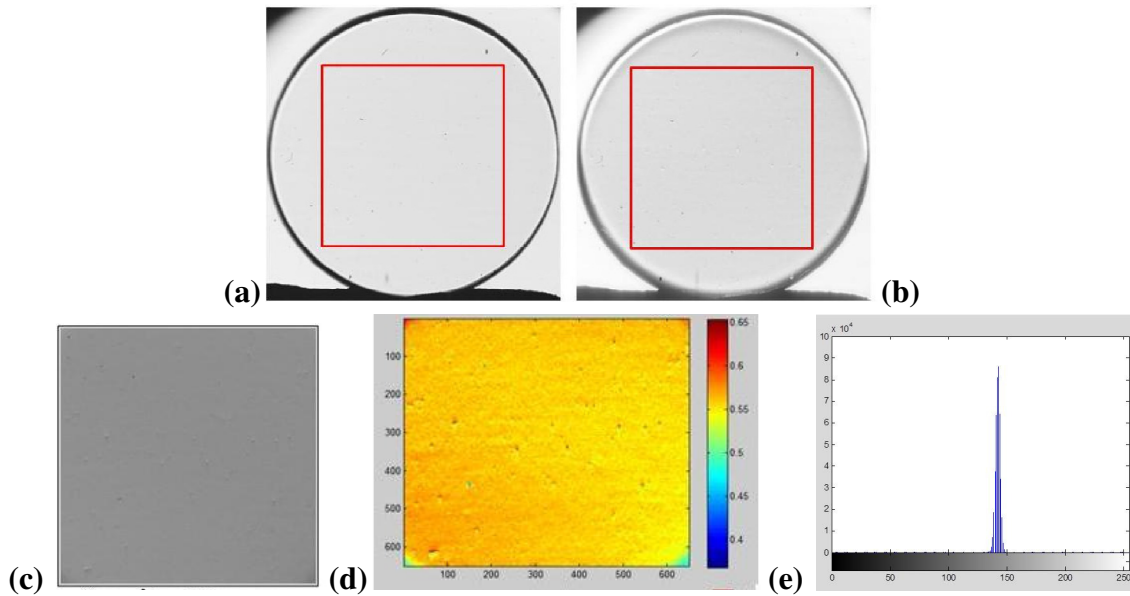
Figure 4.41: Single crystal Undoped YAG as an example of a good sample with no inhomogeneities (a) Bright Field image (b) Schlieren Image (75%) cutoff (c) normalized image (d) False-color intensity variation (e) Intensity Histogram representing the tonal distribution

The Schlieren image has a uniform distribution of intensity, which gives the image a smooth appearance (Figure 4.41 (b)). This uniform intensity in the Schlieren image points to a uniform distribution of refractive index in the body of the sample. The intensity histogram shows a sharp and narrow peak (~ 87,000) and FWHM value (< 5) representing a small variation in the intensity values for the pixels in the image. From the histogram of the normalized Schlieren image, it is observed that maximum number of pixels is around the intensity value of 140.

Case 1-b: Low Quality Sample

The Schlieren imaging technique is applied to analyze a poor quality sample (20% Er:Y_2O_3), having large refractive index variations across the whole sample. The bright field and the Schlieren images are shown in Figure 4.42 (a) and (b), respectively. The refractive index variations in the bulk of the poor quality sample are evident from the non-uniform intensity distribution in the bright-field image of the sample (Figure 4.42 (a)).

The bright field image also has a darker contrast compared to the background, and shows localized distortions and intensity variation across the sample (Figure 4.42 (a)). The intensity contrast in the bright field image is from large defects present in the body of the PLM sample. These defects create a dark shadow, in the transmitted light as can be seen in Figure 4.42 (a).

The Schlieren image has a grey tone, with a non-uniform distribution of intensity, which gives the image a textured (orange peel) appearance (Figure 4.42 (b)). This non-uniform intensity variation in the Schlieren image highlights the variation of refractive index in the body of the sample. From the Schlieren image, a section of the image, represented by the red square, was used to perform image analysis using the process described in section 4.4.5. From the

analysis of the Schlieren image, a false color image highlighting the variation in the image tone was plotted (Figure 4.42 (d)).

Furthermore, an intensity histogram of the normalized Schlieren image was plotted, shown in Figure 4.42 (e). The intensity histogram shows a lower peak (~ 3,700) and FWHM value (< 55) representing a large variation in the intensity values for the pixels in the image. The broad histogram of the normalized Schlieren image points to a large distribution of refractive index variation in the bulk of the poor quality sample.
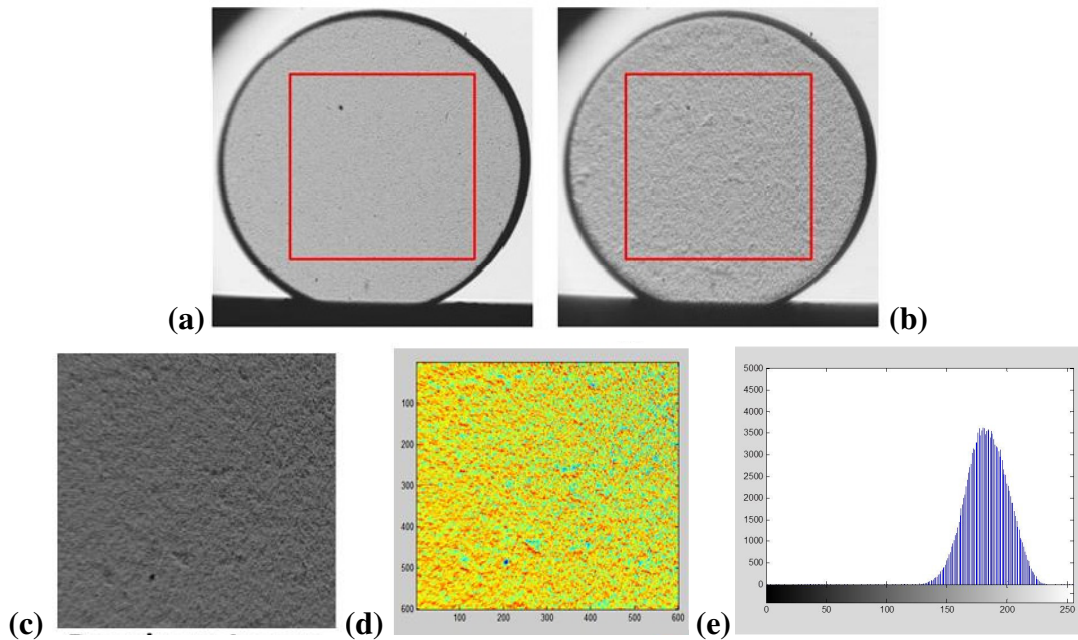
Figure 4.42: A poor quality PLM sample with significant inhomogeneities in refractive index across the whole sample volume. (a) Bright Field image (b) Schlieren Image (75%) cutoff (c) normalized image (d) False-color intensity variation (e) Intensity Histogram representing the tonal distribution.

Case 2: 0.9% Nd:YAG Laser gain media

In this section, the effect of increasing length on characterization of bulk scattering using Schlieren imaging is explored. Comparison of between high quality single crystal and poor quality PLM demonstrated using the cutback samples. Schlieren images of single crystal and PLM samples of 0.9% Nd:YAG laser gain media of different length sections are compared for this analysis. The Schlieren images are further related to Transmitted Beam Wavefront Profile, to emphasize the ambiguity and misinterpretation that occurs when analyzing thin samples. All the Schlieren images, for both the single crystal and PLM samples, were taken at identical conditions, with the Schlieren filter at 75% cutoff position. This measurement provided a direct comparison to highlight the effect of the length of sample has on bulk scattering.

The Schlieren images for the samples (single crystal and PLM) and a histogram of the intensity distribution in the images is plotted for analysis. From the trends in the FWHM and the peak values of the histogram plot of intensity distribution, the dependence of length on bulk scattering in the PLM samples is determined.

(A) Single Crystal 0.9% Nd:YAG samples

To create a baseline, six single crystal 0.9% Nd:YAG samples (cutback samples) of different lengths (R1- 0.75 mm, R2- 1.25 mm, R3- 2.75 mm, R4- 5.5 mm, R5- 11 mm, R6- 22 mm) were imaged. Figure 4.43 (b) shown the Schlieren image (taken at 75% cutoff position) of bulk through the length (22 mm) of the longest single crystal 0.9% Nd:YAG rod (sample R6). As all the six single crystal 0.9% Nd:YAG samples were identical and did not exhibit measureable refractive index inhomogeneity, nor was bulk scattering observed for any sample lengths. This was also supported by the Transmitted Beam Wavefront Profiles for all the single crystal samples which did not show any distortions to the transmitted laser beam (from section 4.3 - Figure 4.16).
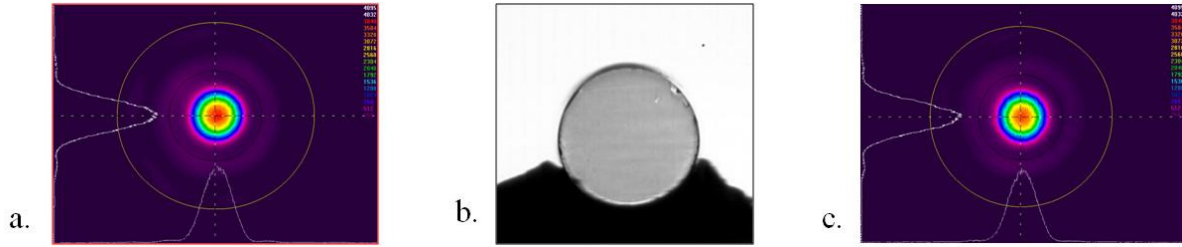
Figure 4.43: (a) Incident laser beam profile (b) Schlieren image, and (c) transmitted beam wavefront profile through a 0.9% Nd YAG laser rod of 22 mm length.

The Transmitted Beam Wavefront Profile shows negligible distortion to the incident laser beam (Figure 4.43 (a)), after passing through 22 millimeters of the single crystal sample R6 (Figure 4.43 (c)). From the analysis of the Schlieren image and from the plot of the intensity histogram, the peak values of the histogram and the FWHM were obtained, and are plotted in Figure 4.11 and Figure 4.12 respectively. This very high peak value and narrow FWHM is representative of a uniform intensity Schlieren image, and which in-turn points to a very uniform refractive index distribution in the body of the single crystal sample (R6).

(B) Polycrystalline 0.9% Nd:YAG samples

The six 0.9% Nd:YAG samples (cutback samples) imaged here were cut from a larger sample, hence all the samples were identical, only the physical lengths were different. All six PLM 0.9% Nd:YAG samples (B1 - 0.53 mm, B2 - 1.33 mm, B3 - 2.71 mm, B4 - 8.55 mm, B5 - 10.87 mm, B6 - 22.1 mm) were imaged at the same Schlieren filter cutoff positions for comparison with the single crystal samples (R1 – R6). The thin PLM sample (B1, length = 0.53 mm) appears as good as the single crystal material. The presence of bulk scattering is not readily observed in the images obtained from the Transmitted Beam Wavefront Profile, as can be seen in Figure 4.19. From the Schlieren Images of the PLM samples, it is possible to readily identify

large defects (~ mm) localized through the sample, which are not easily observed when beam profiling is done using a small (~ 300 µm) laser probe beam.

With increasing length of the PLM samples, the refractive index inhomogeneity present in the sample becomes more evident. This is also observed in the images obtained from the Transmitted Beam Wavefront Profiling, discussed previously in section 4.2. The FWHM and the peak values of the intensity distribution histogram for the Schlieren images of the PLM samples are measured and plotted in Figure 4.45. The plot shows the decrease in the peak value of the histogram and increase in the FWHM as the sample length is increased. This points to cumulative effect of bulk scattering as the length of the sample is increased.

In the case of the thinnest PLM sample (B1 – 0.53 mm), with smaller bulk volume, the laser beam has a least effective interaction length with the samples' bulk. Due to the small interaction length, the distortions to the transmitted beam are minimized, and the sample appears as good as a single crystal. This can be observed from the transmitted beam wavefront profiles shown in Figure 4.43 (c) for the single crystal and Figure 4.44 (a) for PLM sample B1.

Looking at the Schlieren image for the PLM sample (B1), we observe small areas in the sample where distortions are visible and at a few locations small defects are also identified (Figure 4.44 (a)). These defects and distortions in sample B1 are not readily identified, just by looking through the sample or performing a beam profile at one location in the sample. From the Schlieren image analysis, it is also observed that the peak value of the intensity histogram and FWHM for the PLM sample B1 is similar to that of the single crystal sample R6.

As the sample lengths of the PLM is increased, the cumulative effect of increased path length on bulk scattering, becomes more evident in the Schlieren images as well as for the

transmitted beam profile shown in Figure 4.44 (b) through Figure 4.44 (f). In the case of longer samples, the Schlieren images show pronounced inhomogeneities in the refractive index across the bulk.

Observing the Schlieren images for the two longest samples (B5, and B6), it can be noted that the intensity distribution across the sample is not uniform, and there are areas which appear much brighter than other, resulting in strong contrast in the image. Some of the large-scale defects present in the body of the samples result in a shadow, and appear black areas.

From the analysis of the Schlieren images of all the samples, and plotting the intensity histograms, a trend is obtained for both the peak values of the histogram and the FWHM values. The peak values of the intensity histograms are plotted in Figure 4.45, and the FWHM values of the intensity histograms are plotted in Figure 4.46.

Next, with the increase in the sample lengths of the PLMs, the peak values of the intensity histogram decrease, while the FWHM values increase. Comparing the single crystal (R6) and PLM sample (B6), both of which are of approximately the same lengths, the difference in both the peak intensity values and the FWHM can be seen from the graphs in Figure 4.11 and Figure 4.12.

Hence, just by analyzing the thin samples of a PLM, it is difficult to identify bulk scattering suggests that the quality of the material is good for application towards generating lasers. The sensitivity of Schlieren imaging to identify minute refractive index variations promotes the identification of bulk scattering and defects present in the body of even thin samples of poor quality materials, which otherwise would be accepted as good.
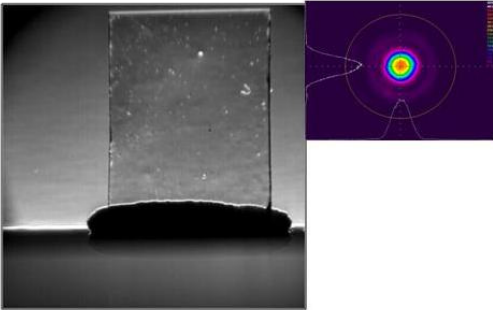
(a). Sample B1 (0.53 mm)
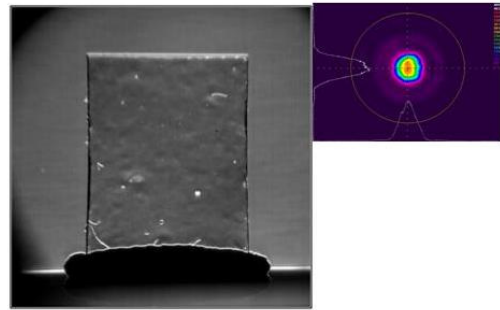
(b). Sample B2 (1.33 mm)
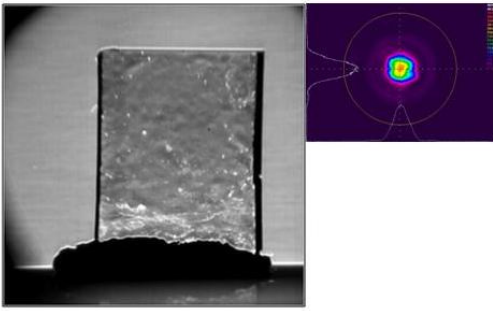
(c). Sample B3(2.71 mm)
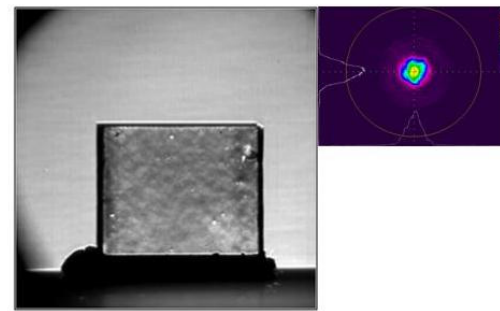
(d). Sample B4 (8.55 mm)
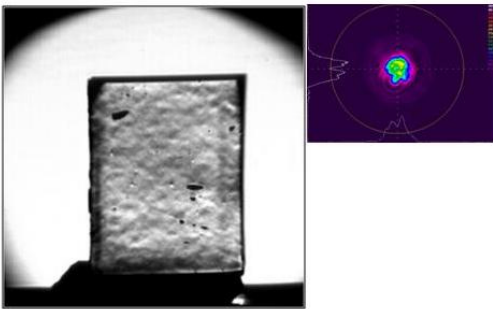
(e). Sample B5 (10.87 mm)
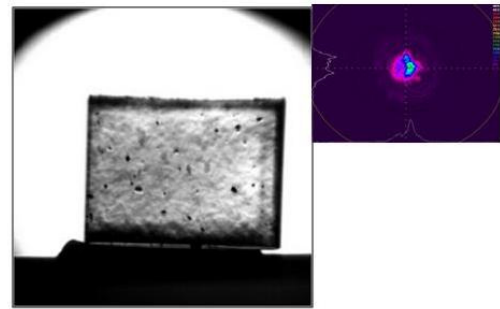
(f). Sample B6 (22.1 mm)

Figure 4.44: Schlieren and Transmitted Beam Wavefront Profile through PLM 0.9% Nd:YAG samples (cutback samples) of increasing lengths: (a) 0.53mm, (b) 1.33 mm, (c) 2.71 mm, (d) 8.55 mm, (e) 10.87 mm, (f) 22.1 mm
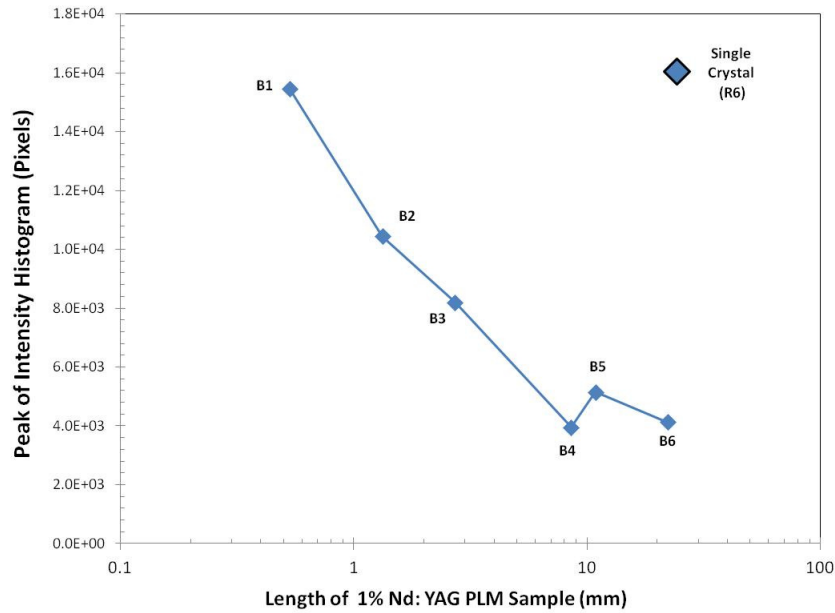
Figure 4.45: Change in the peak value of the intensity histogram (obtained from the image analysis of the Schlieren images), for PLM 0.9% Nd:YAG samples (cutback samples) of increasing lengths. The peak value for the longest single crystal sample (R6) is also plotted for comparison
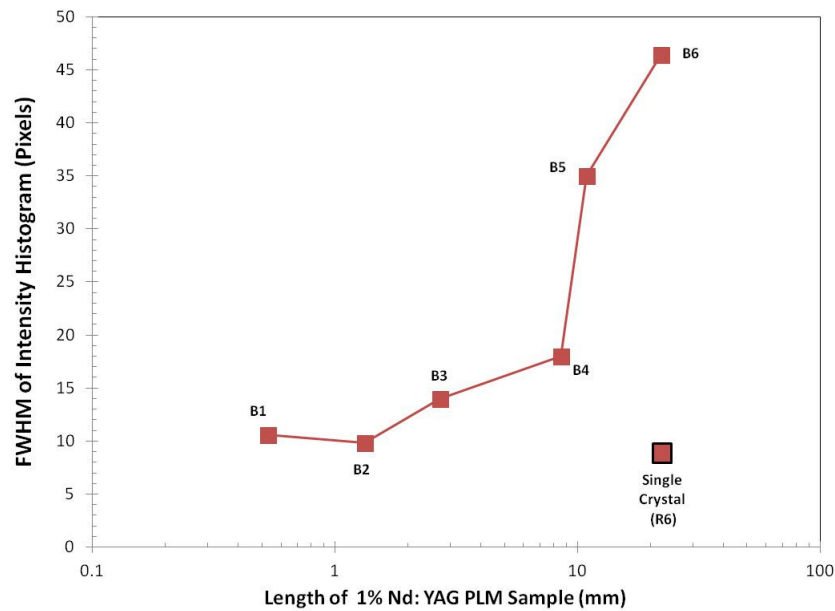
Figure 4.46: Change in the FWHM of the intensity histogram (obtained from the image analysis of the Schlieren images), for PLM 0.9% Nd:YAG samples (cutback samples) of increasing lengths. FWHM value for the longest single crystal sample (R6) is also plotted for comparison

4.4.7 Discussion on Schlieren Imaging

White light Schlieren is used to image the spatial distribution of refractive index in the PLM sample. The PLM sample is illuminated using a white light source, and the transmitted light is imaged. A knife–edge filter is inserted, either below or above the optical axis to block >50% of the transmitted light. The presence of refractive index variations in the PLM sample causes the incident white light to deflect from its normal path.

The deflection of light due to the change of refractive index is both below and above the optic axis, and depends on the gradient of refractive index. As at least half of the optical axis is blocked by the filter, only the deflected light which passes above the filter creates a brighter area, and the blocked light results in a dark area on the image.

This creates a contrast on the image, which reflects directly the variation (slope) of refractive index in the PLM sample. By placing the knife-edge on the other side of the optic axis, the contrast on the image is reversed. As the white light source (halogen lamp) has a broad spectra range (Visible to Infrared), and very small spatial and temporal coherence, no interference effects are observed.

One of the main advantages of the present setup is that by changing the focal length of the imaging lens, the location of the in-focus imaging plane can be moved to observe the Schlieren image at any given depth in a sample. This allows for identification of localized defects present at different depths inside the sample.

4.5   Conclusions

Since the first demonstration in 1995 of lasing action in polycrystalline ceramic laser gain media (Nd:YAG), the prospects of being able to fabricate polycrystalline laser media (PLM) with customized doping profiles, multiple dopants, and dimensions inconceivable using current technology has redefined and re-energized laser gain material development. Over the past few years, the laser community has established that single crystal and (good quality) polycrystalline laser material are identical in every respect except how they are made (CZ growth or polycrystalline fabrication).

Despite all the progress in fabricating and subsequently using large dimension PLMs to demonstrate generation of power levels beyond 100kW, there still does not exist a reliable and fast diagnostic methodology for assessing the quality of PLMs. The most common (and often misleading) method to ascertain transparency has been to place the sample under investigation over an image or pattern, and see through it by the naked eye to detect bulk scatter. This has been known to produce many false positive readings – crystals that do not actually exhibit bulk scatter by that insensitive technique are often thought to be good candidates for laser media.

Bulk scattering as a metric for quantifying optical transparency is an often used technique for determining the quality of optical and/or laser materials with the goal being to achieve the lowest possible bulk scattering. Optical transparency is not only the measure of the quality of PLM, it is also the feedback mechanism that allows for modification of the processing steps used in fabrication of PLMs with the aim of removing the scattering centers.

The objective of this dissertation was to develop new methodology for the characterization of bulk scatter in transparent PLMs. This chapter details the different

127

experimental methods utilized to investigate bulk scattering as a function of material type (single crystal vs. polycrystalline or PLM), effects of dopant concentration and path length in PLMs. Bulk scattering in PLMs (or any transparent material) is due to the spatial variation in the refractive index across the PLMs and leads to a reduction in the transmitted intensity and introduces spatial and temporal distortions to the transmitted wavefront.

Transmitted Beam Wavefront Profiling (TBWP) allowed for the direct imaging of the distortions introduced by bulk scattering in a PLM sample. TBWP was found to be a simple, fast and accurate method for detecting the presence of and extent of bulk scatter in a PLM. The distortions observed in the transmitted wavefront are a direct manifestation of the presence of refractive index inhomogeneities in the PLM sample. A diffraction limited laser beam incident on a PLM is severely distorted due to bulk scattering as it propagates through the PLM.

The incident laser beam encounters modulations to the refractive index as it propagates through the PLM. The inhomogeneity in the refractive index of the sample causes a single laser beam with a Gaussian profile to break into multiple beamlets, each of which has a non-Gaussian intensity distribution. The individual beamlets are deflected every time they experience a refractive index variation. This also causes beamlets to undergo different effective path lengths through the sample and different phases as they exit the PLM sample.

As the distorted beam emerges out of the PLM sample, the individual beamlets in the exiting beam has a different propagation direction (due to multiple deflections) and a random phase. At the imaging plane, the interference and superposition of the individual beamlets results in a complex intensity distribution. This intensity distribution is the distortion in the transmitted beam and is different at different locations of the PLM sample

Finally, white light Schlieren imaging is used to directly record the spatial distribution of refractive index in the PLM sample. The PLM sample is illuminated using a white light source, and the transmitted light is imaged. A knife–edge filter is inserted, either below or above the optical axis to block > 50 % of the transmitted light.

The presence of refractive index variations in the PLM sample causes the incident white light to deflect from its normal path. The deflection of light due to the change of refractive index is both below and above the optic axis, and depends on the gradient of refractive index. As half of the optical axis is blocked by the filter, only the deflected light which passes above the filter creates a brighter area, and the blocked light results in a dark area on the image. This creates a contrast on the image, which reflects directly the variation (slope) of refractive index in the PLM sample. By placing the knife-edge on the other side of the optic axis, the contrast on the image is reversed.

As the white light source (halogen lamp) has a broad spectra range (Visible to Infrared), and very small spatial and temporal coherence, no interference effects are observed. Additionally, by changing the focal length of the imaging lens, the location of the in-focus imaging plane can be moved to observe the Schlieren image at any given depth in a sample. This allows for identification of localized defects present at different depths inside the sample.

Chapter 5

Laser Oscillations

5.1   Introduction

Bulk scattering loss in single crystalline or polycrystalline laser gain media has a significant impact on the performance characteristics of solid state lasers. Within the laser community, it has been established that single crystal and polycrystalline laser gain media can exhibit lasing behavior. The previous chapter detailed the techniques investigated for rapid, accurate, and reliable means to characterize bulk scatter in single and polycrystalline laser gain media. The combination of wavefront beam profiling and Schlieren imaging was shown to yield the most accurate visualization of the presence of bulk scatter in the two types of laser gain media.

The current chapter reports on the results of investigation where the original intent was to demonstrate that there is no difference in the laser performance when using a single crystal or a high quality PLM as the gain media. The laser performance parameters were those of relevance to the laser engineer / scientist such as the lasing threshold, total output power, optical-to-optical slope efficiency, and spatial beam quality. The first experiment was to compare the performance of a single crystal and a polycrystalline 50% Er:YAG in a flash-lamp pumped laser setup. As per the vendor, the polycrystalline Er:YAG rod that was procured was quoted to be 'as good as' the single crystal Er:YAG and expected to yield same laser performance. Such was not the case. As an opportunity to validate the diagnostic techniques detailed in the previous chapter, the polycrystalline Er:YAG rod was evaluated and determined to be of inferior quality. The second experiment using a DPSS (Diode Pumped Solid State) laser architecture was used to compare

single crystal and polycrystalline Nd:YAG laser gain media, but this time with confirmation that the PLM was indeed high quality on par with single crystal laser gain media. Using lessons learned in the first two experiments, and using the DPSS architecture of the second experiment, a third experiment was made which attempted to produce laser oscillations in the mid-IR (~3 µm) wavelength region using a 20% $Er:Y_2O_3$ which was assumed to be good based on a simple visual inspection.

5.2   Materials and Methods

5.2.1   Flash-lamp Pumped 50% Er:YAG Laser

Figure 5.1 depicts the experimental setup utilized for comparing laser performance of single crystal and polycrystalline 50% Er:YAG laser rods under flash-lamp excitation. The laser rods were fabricated to be 5mm diameter and 110 mm in length. The rod ends were laser quality polished flat and parallel to one another and were not AR (anti-reflection) coated. The barrels of the rods were fine ground (~ 10 µm surface roughness). The polycrystalline laser rod was fabricated by World Labs Co., Nagoya, Japan. The single crystal rod was CZ grown and fabricated by Northrop-Grumman, Synoptic Inc., Charlotte, NC.

The laser resonator consisted of flat high reflector (HR) and flat output coupler (OC) separated by 30 cm. The HR and OC reflectivities were R > 99.5 % and R ~ 85 %, respectively. The rod and the flash-lamp were housed inside a close coupled pump chamber located in the middle of the resonator cavity. The flash-lamp was filled with xenon gas to 450 Torr. The lamp housing was made from cerium doped quartz. The cerium acts as cutoff filter for radiation below ~ 350 nm from being incident onto the Er:YAG rod and thereby preventing solarization (photo-darkening due to F-centers or color-centers which are formed in the glass as a result of the UV radiation from the flash lamps) in the Er:YAG rod.

131

The emission spectrum from the flash-lamp is centered at approximately 900 nm (FWHM ~ 400 nm) and red-shifts slightly with increasing drive voltage across the lamp. The tube housing the Er:YAG rod and the lamp within the pump chamber is surrounded by packed $BaSO_4$ powder which acts as a diffuse scattering surface of the lamp emission. The pump chamber housing the Er:YAG rod and the flash-lamp is water cooled. The Er:YAG rod is pumped along the length of the laser rod. The flash-lamp was driven via a 2.5 kW pulse forming network (Model 882/883, Analog Modules Inc., Kissimee, FL). The duration of the flash-lamp excitation pulse was ~ 350 µsec.

The laser was operated at 4 Hz repetition rate. The flash-lamp driver voltage was varied from 800 V to 1500 V in increments of 20 V. The electrical input energy to the flash-lamp (calculated using the equation, $E_{in} = \frac{1}{2}CV^2$ where C is the capacitance (200 µF)) was varied over the range of 40 J to 250 J (the power supply maximum). The output energy per pulse from the laser was measured using a thermopile detector coupled to a digital readout ((Model 50A-BB, NOVA II display, Ophire Inc.).
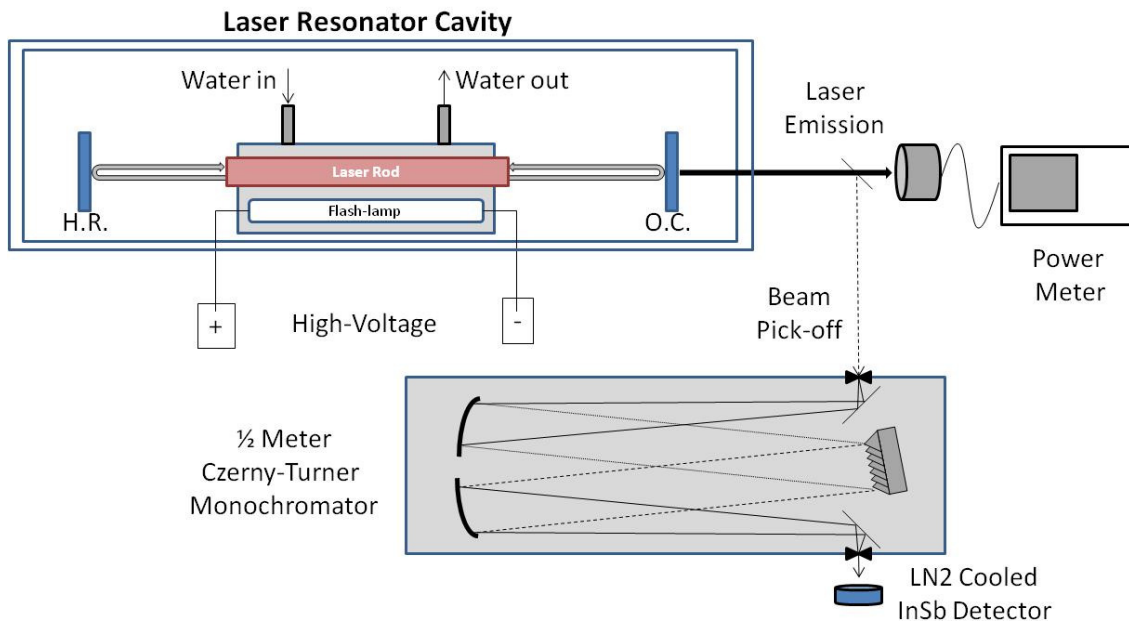
Figure 5.1: Setup for flash-lamp pumped Er:YAG laser.

A thermopile sensor has a series of bimetallic junctions. The laser pulse incident on the detector creates localized heating of the surface, causing an increase in the temperature. This temperature difference between the junctions on the thermopile sensor leads to a voltage difference which is converted and energy equivalent using a calibration traceable to a NIST standard.

Results of Laser Oscillation Experiments: Flash-lamp Pumped 50% Er:YAG

Figure 5.2 shows the results of the output energy as a function of the input electrical energy for the single crystal and polycrystalline 50% Er:YAG laser rods. The threshold for onset of lasing action is almost 50% higher in the case of the polycrystalline Er:YAG (~ 60 J vs. 40 J in the case of the single crystal Er:YAG). The polycrystalline Er:YAG has almost a 4x lower maximum output compared to the single crystal Er:YAG (0.6 J vs. 2.4 J in the case of single crystal Er:YAG) .
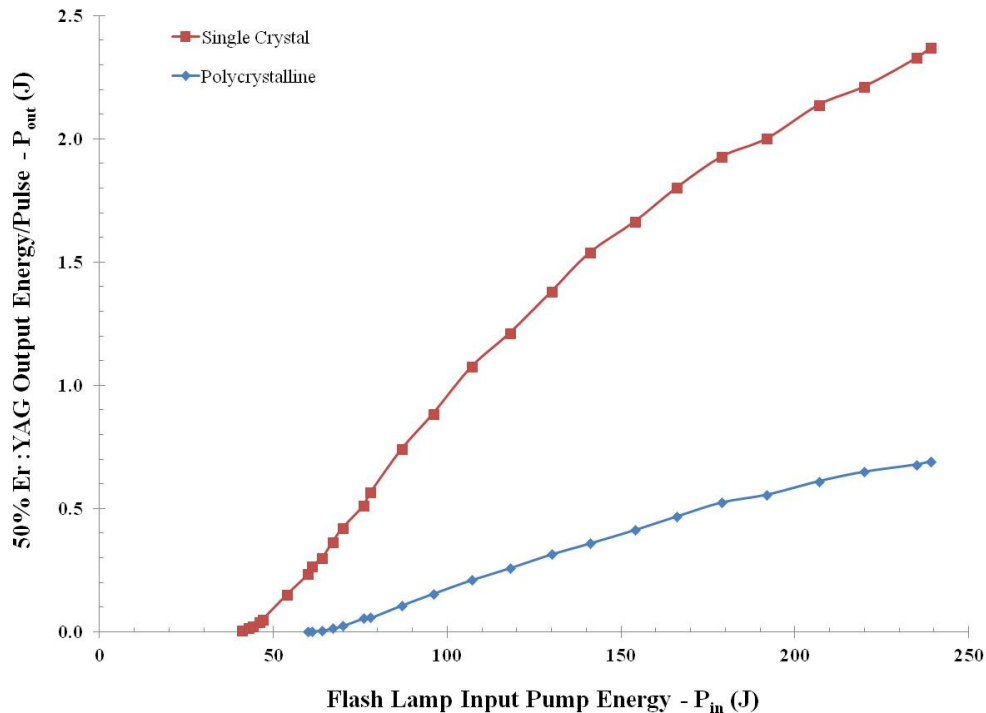
Figure 5.2: Laser output of 50% Er:YAG as a function of incident pump power delivered by the flash-lamp.

133

5.2.2 Diode Pumped 0.9% Nd:YAG Laser

The complexity of the experimental setup utilized the Er:YAG laser experiment was significantly reduced and the experiment repeated to evaluate the laser performance for the three different 0.9 % Nd:YAG . As in the case of the Er:YAG laser comparison described above, the setup used and all operating conditions were kept constant except simply substitute the Nd:YAG laser gain sample.

Figure 5.3 shows the diode pumped Nd:YAG laser setup. The three different 5x5x6 mm^3 0.9% Nd:YAG samples were evaluated: a single crystal Nd:YAG (Sample I.D. - S1, Northrop-Grumman, Synoptics Inc., Charlotte, NC); a high quality polycrystalline Nd:YAG (Sample I.D. - K1, Konoshima Ltd., Osaka, Japan)); and a poor quality Nd:YAG (Sample I.D. - G18, Air Force Research Laboratory, WPAFB, OH).

For all three Nd:YAG samples, the two parallel 5x5 mm^2 faces were commercially polished to a laser quality flatness and parallelism. The polished faces were not AR coated. The rest of the four 5x6 mm^2 sides were roughened, to prevent parasitic oscillations. The Nd:YAG blocks were housed in a water-cooled copper block where the surfaces in contact with the Nd:YAG block were lined with indium foil to increase thermal contact and heat removal efficiency. The cooling conditions were 25 $^{\circ}$C, flow rate of 1.5 GPM at 50 psi.

The laser resonator consisted of flat high reflector (HR) and flat output coupler (OC) separated by 5 cm. The side of the HR facing the Nd:YAG block was dual band coated to be R > 99.5% at 1064 nm (the lasing wavelength) and T > 80% at 808 nm (the excitation pump wavelength). The side of the OC facing the Nd:YAG block was also dual band coated to have R ~ 90% at 1064 nm and R ~ 99.5% at 808 nm (to reflect back into the Nd:YAG the pump light that was not absorbed during the first pass).
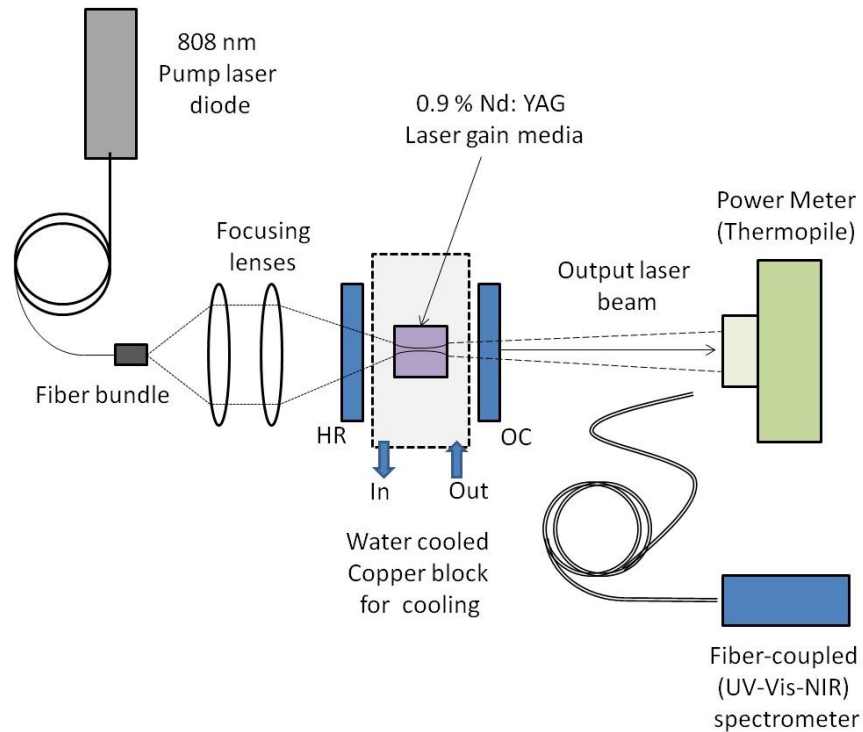
Figure 5.3: Schematic of the DPSS Laser setup used for laser oscillations in 0.9 %
Nd:YAG.

The pump source for the Nd:YAG was, a continuous wave (cw) 12 Watt 808 nm (FWHM
< 10nm) fiber coupled diode (Model T40, Spectra Physics, Santa Clara, CA). The output
wavelength of the diode was actively temperature controlled using thermoelectric coolers. The
output power from the Nd:YAG laser was measured using a thermopile detector coupled to a
digital readout (Model 50V, NOVA II display, Ophir Inc.,).

Results of Laser Oscillation Experiments: Diode Pumped 0.9% Nd:YAG

Figure 5.4 shows the output power as a function of input power for the three different
Nd:YAG samples evaluated. The lasing threshold for single crystal and high quality PLM
Nd:YAG is similar (2 W (SC1) vs. 2.25 W (K1)). The lasing threshold for the poor quality PLM
Nd:YAG (Sample G18) is approximately 8.5 W. All three Nd:YAG samples showed an increase
in the output power with increasing input power.
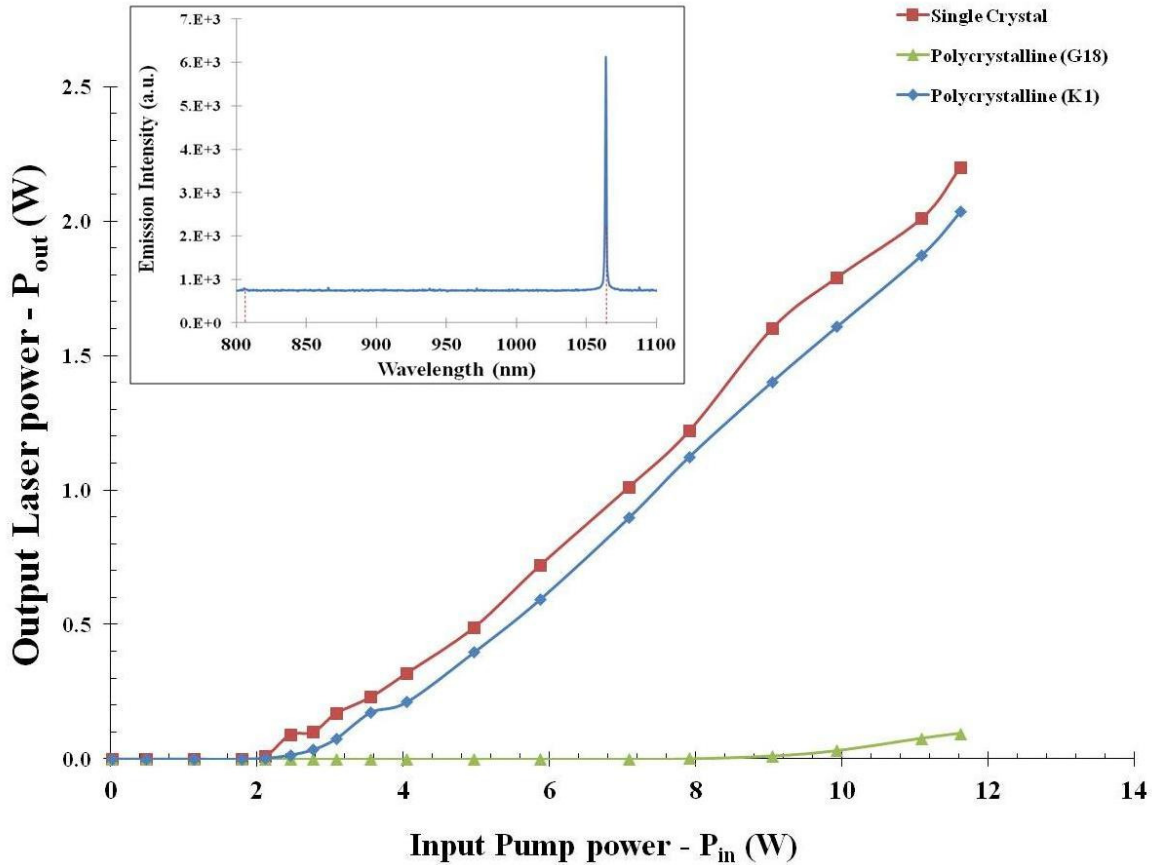
Figure 5.4: Laser output power as a function of incident pump power, for the three different 0.9 % Nd:YAG samples. The inset graph shows the emission wavelength at 1064 nm, from the laser for all the three samples.

The maximum output power level achieved by single crystal, high quality PLM, and the poor quality PLM Nd:YAG with 11.6 W input power was 2.2 W, 2.1 W, and 0.095 W, respectively. The optical-to-optical slope efficiency for the same three samples was 18.76%, 17.52%, and 0.82%, respectively.

5.2.3   Diode Pumped 20% Er:Y_2O_3

Figure 5.5 shows setup used in the PLM Er:Y_2O_3 experiment. The faces of the 10 mm diameter x 5mm thick PLM 20% Er:Y_2O_3 (World Labs Co., Nagoya, Japan) were polished flat and parallel to laser quality finish and were not AR coated. The Er:Y_2O_3 sample was wrapped on the edges in indium foil and passively conduction cooled by holding it in a brass holder that

136

provided a large thermal mass for heat extraction. The laser resonator consisted of flat HR (R > 99.5% at 3 µm, T ~ 80% at 975 nm) and flat OC (R ~ 90% at 3µm) separated by 15 mm. The HR and OC were not optimized in any way for the 975 nm pump wavelength.

The pump source for the Er:Y_2O_3 was a cw, 25 Watt 975 nm (FWHM < 2nm) fiber coupled diode (Model Brightlase® Ultra-50, QPC Inc., Sylmar, CA). The wavelength of the diode was primarily controlled via the use of a Bragg grating built into the semiconductor structure. The diode was mounted on to a water cooled copper conduction block.

The 975 nm pump wavelength matches to the energy level of the $^4I_{11/2}$ stark manifold, and has been demonstrated to be an efficient method of directly pumping the erbium for achieving mid-IR emission [125 - 127]. The cw pump light was modulated using a mechanical chopper to yield a 1 ms (~ 3x the $^4I_{11/2}$ upper state lifetime) pulse at 4 Hz repetition rate. The output from the diode was focused onto the Er:Y_2O_3 using CaF_2 lenses to yield approximately 500 microns spot size.

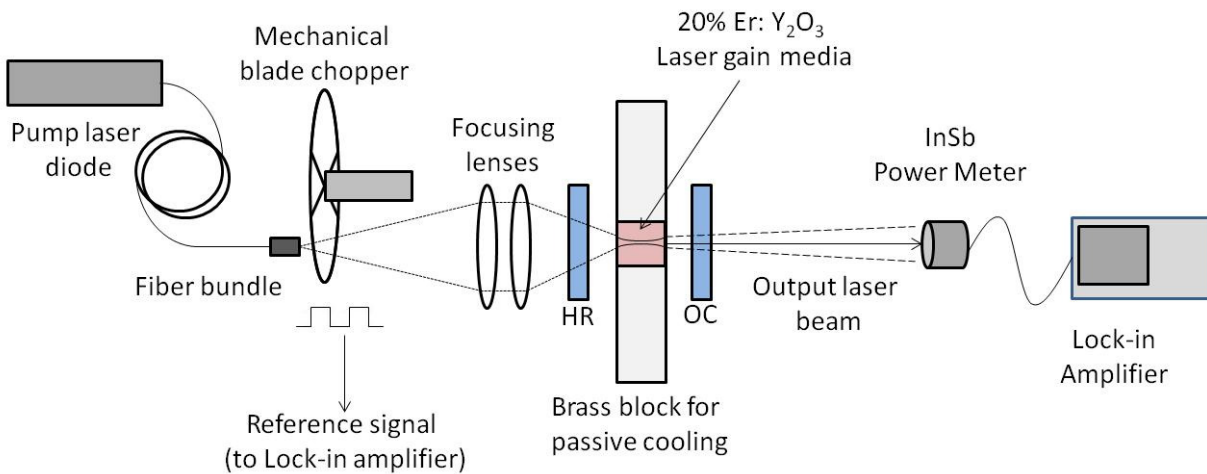**Figure 5.5:** Schematic of the DPSS Laser setup used for laser oscillations in 20% Er:Y_2O_3.

The output power from the pump laser was limited to ~10 W. The output from the Er:Y_2O_3 was monitored using a LN2 cooled InSb detector with a 2 mm thick Germanium window acting as a filter to block the pump light from reaching the detector.

Results of Laser Oscillation Experiments: Diode Pumped 20% Er:Y_2O_3

No laser oscillations were observed for the 20% Er:Y_2O_3 experiment regardless of incident pump power. A weak broadband fluorescence signal was detected on the LN2 cooled InSb detector at all angles but the signal did show any threshold behavior (i.e., increase in intensity with increasing pump power). At 10 W pump power, the sample fractured into two pieces due to inadequate cooling.

5.3   Discussion

The intent of the laser experiments was to demonstrate the effect of bulk scattering loss on laser performance in terms of parameters relevant to the laser engineer / scientist (i.e., threshold for laser onset, output power, slope efficiency, and spatial beam quality). If the PLM was of high quality, then there would (should) not be any difference in the laser performance. Conversely, if the PLM was of poor quality, there would be a significant difference in the laser performance compared to the laser performance using a single crystal laser gain media.

The original (and only intended) experiment was to utilize a single crystal and a high quality polycrystalline 50% Er:YAG rod in a flash-lamp pumped setup. The results shown in Figure 5.6 clearly did not support the original assumption. Comparison of the lasing onset threshold, maximum output energy per pulse as a function of incident energy, and the slope efficiency results obtained using the single crystal clearly outperform the results obtained using the (supposedly) high quality polycrystalline 50% Er:YAG.

138
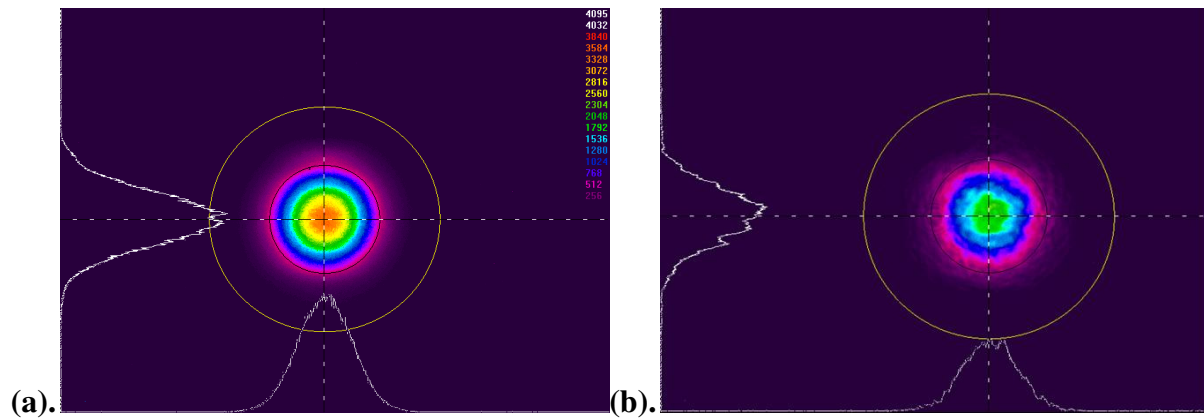
Figure 5.6: Transmitted beam profile through (a) single crystal and (b) polycrystalline 50% Er:YAG Laser rods of 110 mm length.

Utilizing the diagnostic techniques detailed in the previous chapter, the polycrystalline Er:YAG rod was evaluated for bulk scatter. Using just the transmitted beam profiling (see Figure 5.6), the results show that while the transmitted beam profile through the length of both the single crystal is unchanged, the transmitted beam profile through the polycrystalline Er:YAG rod shows significant degradation in the Gaussian distribution and thus explain the poor laser performance observed in the laser experiment.

In keeping with the original objective to compare laser performance between using single crystal and high quality PLM, the first experiment was repeated but this time utilizing a PLM that was confirmed as being high quality. The second set of experiments utilized three matched samples of 0.9% Nd:YAG; a single crystal (S1), a high quality PLM (K1), and a poor quality PLM (G18). The results in Figure 5.4 show that while there is very little difference in the laser performance between the single crystal sample (S1) and the high quality PLM sample (K1), the low quality PLM sample G18 performed very poorly. The trends of the laser performance results observed are corroborated when utilizing the diagnostic techniques reported in the previous chapter (Figure 5.7). In the case of the single crystal Nd:YAG, the transmitted beam profile shows no distortion to the laser beam as it propagates through the sample. The Schlieren

image across the single crystal sample also shows the absence of localized defects and bulk scatter in any part of the sample. In the case of the high quality PLM sample (K1, Figure 5.7(b)), the transmitted beam profile shows little or no distortions to the beam as it passes through the sample.

The reduction in the intensity of the beam is due to Fresnel reflection losses. The Schlieren image of the PLM (K1) sample shows localized regions of distortions near one end of the sample. A quick check of the laser output measurement made in the region at the top of the sample showed a marked reduction in the output power confirming the negative impact of bulk scattering. In case of the poor quality PLM (G18) a large number (approximately 6 - 8 per mm^2) of localized defects were observed in the Schlieren image, and the TBWP showed distortions to the beam (Figure 5.7 (c)).
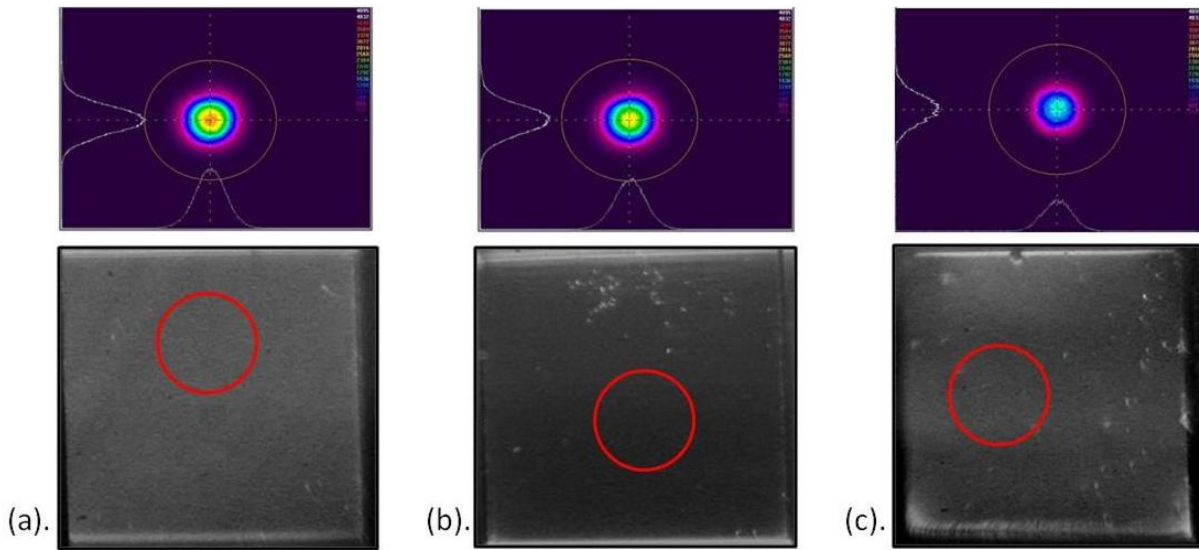
Figure 5.7: Transmitted Beam Wavefront (top) and Schlieren images (bottom) for the three different 0.9% Nd:YAG samples (a) Single crystal sample (S1), (b) high quality PLM sample (K1), and (c) poor quality PLM sample (G18) evaluated in the laser setup. The red circle identifies the region in the gain media selected for laser oscillation.
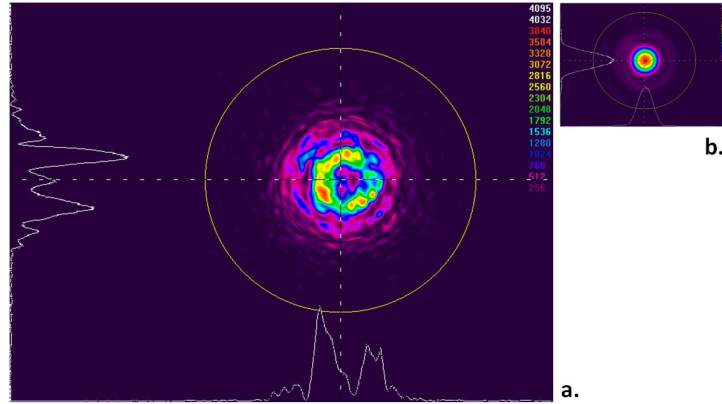
Figure 5.8: (a) Transmitted beam profile of (Y183) 20% Er:Y$_2$O$_3$. (b) Beam profile of the diffraction limited Gaussian profile beam incident on to the sample
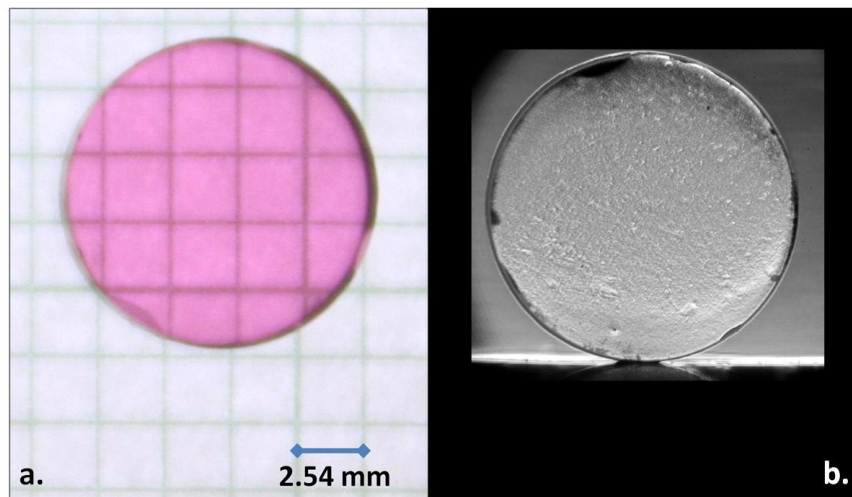
Figure 5.9: (a) Bright field (transmission) image of the (Y183) 20% Er:Y$_2$O$_3$ on a graph paper and (b) Schlieren image, showing the severe refractive index inhomogeneities in the bulk of the PLM.

Comparing the intensity profile from TBWP (Figure 5.7 (a), (b) and (c)), we note the peak intensity for samples S1 (105) and K1 (86) are close, where as for G-18 (54) is approximately 50% lower. Furthermore, the FWHM values for SC1 (89) and K1 (90) are identical, where as for G18 (100) is broader indicative of its poorer quality.

In the case of the poor quality PLM, visual inspection of sample G18 did not show the presence of any bulk scattering. However, the transmitted beam profile and the Schlieren images

141

clearly show the presence of the inhomogeneities in the refractive index in sample G18. Even then, the transmitted beam profile through the selected area in G18, which demonstrated the best laser performance and is marked with a red circle, shows not only the reduction in the transmitted intensity due to Fresnel reflection losses but also distortions in the transmitted beam (Figure 5.7(c)). The Schlieren image for G18 shows an inhomogeneous distribution of defects, with many localized regions of distortions along with many large inclusions around the edges. The resulting higher threshold pump power required for the lasing onset and lower output power are a direct manifestation of bulk scattering in sample G18.

Even though the FWHM for the three Nd:YAG samples were similar, however the full width at 0.1 max (FW0.1M) values were also measured for the same beam profiles for the three samples. This concept was borrowed from X-ray diffraction analysis, where subsurface damage in samples are compared using FW0.1M because of the large variations can be identified at those level, which are not visible in FWHM (as was the present case). The FW0.1M showed considerable difference between the poor quality G-18 sample (FW0.1M (G18) ~ 240) and the other two good samples, SC-1 (FW0.1M ~ 145), and for K-1 (FW0.1M ~ 160) further supporting the conclusion that the sample G18 was inferior to PLM sample K-1 and the single crystal SC-1.

Attempts to lase the 20% Er:Y_2O_3 did not yield any positive results. As was the case with the poor quality PLM, visual inspection of the Er:Y_2O_3 sample Y183 showed no indication of the presence of any bulk scattering. However, the transmitted beam profile and the Schlieren images of sample Y183 clearly show the presence of severe non-uniformity in the refractive index (Figure 5.8). The distortions observed are due to the presence of bulk scattering in the PLM Er:Y_2O_3 (Y183), which resulted in severe losses in the PLM that ultimately prevented the

laser oscillations from occurring. The absence of laser oscillations from the 20% $Er:Y_2O_3$, was primarily due to the losses in the gain media from bulk scattering.

5.4   Conclusions

The lasing experiments described in the present chapter highlighted the effects of bulk scattering losses on the laser performance parameters such as lasing threshold, output energy or power, and the optical-to-optical slope efficiency. Laser performance in high quality PLM was shown to be very comparable to the laser performance using single crystal laser gain media. The presence of bulk scattering at modest levels was shown to reduce the laser performance as evidenced by increased threshold for lasing and lower output energy per pulse. The presence of severe bulk scattering was shown to prevented lasing from occurring.

The differences in the laser performance were corroborated by results obtained from Transmitted Beam Profiling and Schlieren Imaging optical metrology techniques developed in the previous chapter thus validating the applicability of these techniques to rapidly, accurately, and reliably characterize the bulk scattering and thus the quality of PLMs.

Chapter 6

Conclusions and Future work

6.1   Bulk Scattering in PLMs

Polycrystalline laser materials (PLMs) are the next generation of laser materials being developed as replacement of single crystal laser material in high power applications. Advantages of PLM over single crystal materials: ease of fabrication, large dimensions, near-net-shapes, complex shapes and doping profiles. Bulk scattering has always been recognized as the main source of loss in PLMs. The presence of bulk scattering is due to the inhomogeneity in the refractive index across the PLM, and leads to a reduction in the inline transmission through the PLM sample. Inhomogeneities in the refractive index of the PLMs are due to the presence of voids, pores, and phases at the grain boundaries of its microstructure, observed in the SEM and CLSM images of the fractured PLM surfaces.

The loss due to bulk scattering leads to lower laser output power, higher turn-on or laser threshold pump powers, and in some cases even catastrophic material failure. Previously, identification of bulk scatter in PLM has been by the ability to read or image through a thin sample of the PLM material. Alternatively, FTIR measurements on thin sample lengths are sometimes used to approximate a scattering coefficient, based on the Beer-Lambert law, which provide little information to the laser designers.

But, most commonly, it is the ability to 'see' through the sample, which is the acceptable method of testing and qualifying of PLMs for application for laser generation. This is deceptive, inadequate, and in many cases simply wrong

6.2   Present Work

This study has put forward and developed, improved characterization methods to identify the presence of bulk scattering, due to refractive index inhomogeneities in PLMs. New methods developed for the characterization of bulk scatter in PLM are: Transmitted Beam Wavefront Imaging, ARS and Schlieren Imaging.

Rare earth doped YAG and Y_2O_3, were examined as representative polycrystalline laser materials with bulk scattering, and compared with similar single crystal materials. Laser oscillation experiments to compare the single crystal laser material, high quality PLM and poor quality PLMs were performed. The laser experiments showed the reduced laser output and increased threshold pump power, in the poor quality PLMs sample as identified by beam profiling and Schlieren imaging.

Transmitted Beam Wavefront Imaging records the distortions introduced to a laser beam after it propagates through the bulk of the PLM. The presence of refractive index inhomogeneities in the bulk of the PLM cause different parts of the incident laser beam to have different paths through the sample. Bulk scattering in the PLM creates distortions in the transmitted beam, in the forward specular direction, which leads to the beam profile to appear as shattered.

Angle Resolved Scattering (ARS) measurements allowed the mapping of the scattered intensity in both the forward and the backward direction, in all 360 degree angles in a plane, about the PLM sample. The cumulative scattered light intensity, in the forward direction away from the specular beam direction, was used to compare different samples which otherwise had similar transmitted beam wavefront distortions.

145

Finally, a modification of the white light Schlieren Imaging technique was used to directly image the inhomogeneities in the refractive index of the PLMs. The Schlieren imaging setup, allowed for the quick characterization of PLM samples of large dimensions. Using the Schlieren images, it is now possible to directly image the spatial distribution of the refractive index in the sample.

6.3   Future Work

Effect of bulk scattering in PLM have not been explored in detail. This initial investigation into identifying and characterizing bulk scatter has brought out many other related questions. Further research and development of characterization of bulk scattering in PLMs require the improvement of the present experiments, for both higher sensitivity and resolution.

The use of better laser sources, like a narrow line width laser with tunable wavelengths, e.g., Titanium doped Sapphire laser operating in the NIR region. Coupled with such a laser, would be a larger dimension high-resolution beam profiler to image the beam. This would allow the identification of the refractive index inhomogeneities at different wavelength regions away from absorption region an image the distortions in higher resolution. The use of a larger goniometer for the ARS, will allow a better mapping of the scattered light field from the samples.

Furthermore, Schlieren imaging of the PLMs using polarized light and monochromatic light has to be explored. Previous work of Schlieren imaging using a monochromatic laser light, suggests a larger dynamic range for the imaging conditions.

Simulation of the process of beam distortion, based on a diffusion or a random walk model, assuming various parameters in the PLM, like size and number density of scattering centers have to be explored.

Towards the development of PLM laser materials as alternate to single crystal materials, there is a need of systematic study, relating the fabrication method and material parameters to bulk scatter in final PLM.

A systematic study, comparing the particle size of starting powders used to make the green body, to the bulk scatter observed in the final aggregate transparent ceramic PLM. Most of the PLM are made from mono-disperse starting powders, that are either in the 100s of nm or in 10s of µm range, with very little deviation. It has been predicted that use of poly-disperse powders can allow for greater packing densities in the pre-sintered green body, which after sintering can lead to a low porosity (low bulk scatter) transparent PLM.

Finally, a relation between bulk scatter in PLM to the fabrication methodology used in both the process steps involved towards creating the green body (pre-sintered), and the sintering process itself. This includes an exploration in alternate sintering methods, like rapid microwave heating instead of the conventional sintering by convection and conduction) of the green body to create the final transparent PLM. More investigations are required to identify the effect of bulk scatter on the polarization of the transmitted and scattered light. The effect of bulk scattering on pulse propagation and the effect of bulk scattering on pulse width as it travels through the sample, needs more exploration. This will allow us to estimate the effective path length that the pulse takes to travel through the sample.

Bibliography

1. T. H. Maiman, Nature (1960)

2. J. M. J. Madey, Appl. Phys. 42 (1971)

3. B. Bishop, News Releases Lawrence Livermore National Laboratory, March, Https://www.llnl.gov/news/newsreleases/2012/Mar/NR-12-03-02.html (2012)

4. B. P. Abbott, Rep. Prog. Phys. 72 (2009)

5. H. Lubatchowski, *Lasers in Medicine: Laser-Tissue Interactions and Applications*, Wiley (2007)

6. J. N. Parker and P. M. Parker, *Laser Eye Surgery: A Medical Dictionary, Bibliography and Annotated Research Guide to Internet References*, ICON Health Publications (2003)

7. F. Frankhauser and S. Kwasniewska, *Lasers in Ophthalmology,* Kugler, The Hague (2003)

8. W. M. Steen, J. Mazumder, K. G. Watkins, *Laser Materials Processing*, 3rd ed., Springer, Heidelberg (2003)

9. E. Kannatey-Asibu Jr, *Principles of Laser Materials Processing,* Wiley (2008)

10. T. Fuji and T. Fukuchi, *Laser Remote Sensing*, CRC (2005)

11. C. D. Boley, S. N. Fochs, A. M. Rubenchik, Journal of Directed Energy (UCRL-JRNL-234510), vol. 3 (2008)

12. W. Koechner, *Solid State Laser Engineering*, 6th edn. Springer, Berlin (2006)

13. R. R. Monchamp, J. Cryst. Growth. 11, (1971)

14. A. Ikesue and Y.L. Aung, Nature Photonics (2008)

15. K. H. Sun and M. L. Huggins, J. Am. Ceram. Soc. 29 (1946)

16. M. L. Huggins and J. M. Stevels, J. Am. Ceram. Soc. 37 (1954)

17. E. Carnall, S. E. Hatch, and W. F. Parsons, Mater. Sci. Res. 3 (1966)

18. C. Greskovich and K. N. Wood, Am. Ceram. Soc. Bull.52 (1973)

19. A. Ikesue, J. American Ceramic Society 78 (1995)

20. K. Ueda, LEOS 2005, The 18th Annual Meeting of the IEEE (2005)

21. V. Lupei, Opt. Mater. 31 (2009)

22. I. Imai, M. Fujita, H. Oishi, M. Irie, S. Kimijima and T. Miyai., Optics and Photonics Japan, Ceramic Laser International Workshop (2006)

23. Y. Yanase, M. Fujita and M. Irie., The 24 Japan-Korea International Seminar on Ceramics (2007)

24. M. Fujita, Advanced Solid-State Photonics, Ceramic Lasers Summit (2008)

25. B. Yamamoto, B. Bhachu, K. Cutter, S. Fochs, S. Letts, C. Parks, M. Rotter, and T. Soules, Advanced Solid-State Photonics, OSA Technical Digest Series (2008)

26. C. F. Bohren and D. R. Huffman, *Absorption and Scattering of Light by Small Particles*, Wiley (1983)

27. M. Kerker, *The Scattering of Light*, Academic, New York (1909)

28. L. I. Mandelstam, *Light Scattering by Inhomogeneous Media*, Zh. Russ. Fiz-Khim. Ova.58 (1926)

29. J. M. Bennett and L. Mattsson, *Introduction to Surface Roughness and Scattering* , OSA, (1993)

30. J. C. Stover, *Optical Scattering - Measurement and Analysis*, 2nd Ed. SPIE (1995)

31. M. O. Ramirez, J. Wisdom, H.F. Li, Y.L. Aung, J. Stitt, G. L. Messing, V. Dierolf, Z.W. Liu, A. Ikesue, R. L. Byer, V. Gopalan, Opt. Express 16 (2008)

32. J. P. Boon and P. A. Fleury, *The Spectrum of Light Scattered by Fluids*, Academic Press, New York (1973)

33. J. C. Huie, R. Gentilman, *Window and Dome Technologies and Materials*, SPIE (2005)

34. G. P. Agrawal, *Nonlinear Fiber Optics*, 4th ed. Academic Press (2006)

35. J. G. J. Peelen, Transparent hot-pressed alumina: I: Hot pressing of alumina, Ceramurgia International, Vol. 5 (1979)

36. J. G. J. Peelen, Transparent hot-pressed alumina: II Transparent versus translucent alumina, Ceramurgia International, Vol. 5 (1979)

37. W. Heller, Science and Technology Rev. (2006)

38. A. Ikesue, K. Yoshida, J. Am. Ceram. Soc. 81 (1998)

39. Y. Rabinovitch, D. Tetard, M. D. Faucher, M. Pham-Thi, Optical materials, 24 (2003)

40. A. S. Dukhin and P. J. Goetz, Ultrasound for characterizing colloids, Elsevier (2002)

41. G. Gouesbet, Journal of Quantitative Spectroscopy and Radiative Transfer 110 (2009)

42. R. V. Jones, H. M. Kahan and D. P. Stubbs; *Optical and Acoustical Micro-electronics*, Polytechnic Press, Brooklyn, NY (1975)

43. J. G. Li, T. Ikegami, J. H. Lee, J. Eur. Ceram. Soc. 20 (2000)

44. C. Li, W. Liu, H. Gao, B. Jiang, Y. Wang, H. Kou, Y. Shen, Y. Pan, Y. Bo, Q. Peng, D. Cui, D. Jiang and Z. Xu, Appl Phys B (2011)

45. A. E. Siegman, *Lasers*, University Science Books (1986)

46. A. Kaminskii, *Laser crystals: their physics and properties*, Springer-Verlag (1981)

47. A. Kaminskii, *Crystalline lasers: physical processes and operating schemes*, CRC Press (1996)

48. G. Laufer, *Introduction to Optics and Lasers in Engineering*, Cambridge University Press (1996)

49. H. C. Van de Hulst, *Light scattering by small particles*, John Wiley and Sons, New York (1957)

50. C. Kittel, *Introduction to Solid State Physics*, 8th ed. Wiley (1995)

51. D. J. Griffiths, *Introduction to Electrodynamics*, 3rd ed. Prentice Hall (1998)

52. R. W. P. King, *Fundamental Electromagnetic Theory*, New York, Dover (1963)

53. P. Calmettes, *Optics Communications*, Vol. 44, No. 5, pp. 306-310 (1983)

54. A. Ghatak, *Optics*, 4th ed. McGraw Hill (2009)

55. M. M. Braun and L. Pilon, Thin Solid Films, Vol. 496, No.2, pp. 505-514 (2006)

56. A. Schuster, *An Introduction to the Theory of Optics*, Edward Arnold, London (1904)

57. E. Hecht, *Optics*, 4th ed. Addison Wesley (2002)

58. D. S. Saxon, "Lectures On The Scattering Of Light", Department of Metrology, Scientific Report #9, University of California Library, University of California, Los Angeles

59. P. Bouguer, Essai d'Optique: sur la gradation de la lumiere, Paris, France, Claude Jombert (1729)

60. J. H. Lambert, Augsburg, Germany, Eberhardt Klett, pp. 391 (1760)

61. A. Beer, Annalen der Physik und Chemie, Vol. 86, pp. 78–88 (1852)

62. R. Kitchin, *Stars, Nebulae and the Interstellar Medium: Observational Physics and Astrophysics*, CRC Press (1987)

63. K. N. Liou, *An Introduction to Atmospheric Radiation*, Academic Press (2002)

64. G. Mie, Ann. Phys. 330, pp. 377–445 (1908)

65. J. A. Stratton, *Electromagnetic Theory*, New York, McGraw-Hill (1941)

66. Http://water.usgs.gov/owq/FieldManual/Chapter6/6.7_contents.html

67. Http://www.iso.org/iso/en/CatalogueDetailPage.CatalogueDetail?CSNUMBER=30123

68. Http://www.thermallaminatingfilms.com/haze.php

69. S. Hendy, Applied Physics Letters, Vol. 81, No. 7, pp. 1171-73 (2002)

70. ISO-7027, International Organization for Standardization, Geneva, Switzerland (1999)

71. C. D. Brandle, Czochralski growth of oxides. J. Crystal Growth, Vol. 264, pp. 593-604 (2004)

72. Http://www.as.northropgrumman.com/businessventures/synoptics/assets/synoptics_cz_growth.pdf

73. Http://www.vloc.com/PDFs/YAGBrochure.pdf

74. J. Sanghera, W. Kim, G. Villalobos, B. Shaw, C. Baker, J. Frantz, M. Hunt, B. Sadowski, I. Aggarwal, Development of Ceramic Laser Host Materials, Technologies for Optical Countermeasures - VIII, SPIE, 8187 (2011)

75. Http://www.irconnect.com/noc/press/pages/news_releases.html

76. R. E. Chinn, *Ceramography*, ASM International and the American Ceramic Society (2002)

77. G. L. Kehl, *The Principles of Metallographic Laboratory Practice*, McGraw–Hill Book Co. (1949)

78. R. E. Chinn, *Ceramography: Preparation and Analysis of Ceramic Microstructures*, ASM International, (2002)

79. G. Petzow, *Metallographic Etching: Techniques for Metallotraphy, Ceramography, Plastography*, ASM International; 2nd ed. (1999)

80. K. Serivalsatit, B. Yazgan Kokuoz, B. Kokuoz, and J. Ballato, Optics Letters, Vol. 34 No. 7 (2009)

81. B. D. Cullity, S. R. Stock , *Elements of X-Ray Diffraction*, Prentice Hall, 3rd Ed, (2001)

82. Z. Huanga, X. Sun, Z. Xiu, S. Chen, C. Tsai, Materials Letters, Vol. 58 (2004)

83. J. Wang, Y. Yue , W. Tao, Q. Yu, Z. Tao, X. Sun, Trans. Nonferrous Met. Soc. China, Vol. 13, No. 5 (2003)

84. D. Pelloquin, M. Louër, D. Louër, Journal of Solid State Chemistry, Vol. 112, No. 1 (1994)

85. R. Boulesteix, A. Maître, J.-F. Baumard, Y. Rabinovitch, F. Reynaud, Optics Express, Vol. 18, No. 14 (2010)

86. D. C. Harris, *Materials for Infrared windows and Domes*, SPIE Press Monograph Vol. PM70 (1999)

87. G. C. Holst, *Testing and Evaluation of Infrared Imaging Systems*, 2nd ed., SPIE (1998)

88. J. P. Boon, and P. A. Fleury, *The Spectrum of Light Scattered by Fluids*, Adv. Chem Phys. XXIV, Academic Press, New York (1973)

89. Http://www.allaboutgemstones.com/gemstone_diaphaneity.html

90. Http://www.edmundoptics.com

91. H. R. Blackwell, J. Optical Society America, Vol. 36, pp. 624–643 (1946)

92. C. Li, W. Liu, H. Gao, B. Jiang, Y. Wang, H. Kou, Y. Shen, Y. Pan, Y. Bo, Q. Peng, D. Cui, D. Jiang, Z. Xu, Appl Phys B, 104, (2011)

93. ASTM D1003 - 11e1, "*Standard Test Method for Haze and Luminous Transmittance of Transparent Plastics*", ASTM International, West Conshohocken, PA, 2003, DOI: 10.1520/D1003-11E01

94. Http://www.reoinc.com/products/hene_lasers/Multi-line

95. Http://www.ophiropt.com

96. Http://www.bede.com, Quickgraph software, Ver. 1 (1998)

97. ASTM standard E2175-01, "*Standard Practice For Specifying The Geometry Of Multi Angle Spectrophotometers*", ASTM International, West Conshohocken, PA (2008)

98. ANSI C95.3, "American National Standard Recommended Practice for the Measurement of Potentially Hazardous Electromagnetic Fields - RF and Microwave" (1991)

99. S. A. Prahl, Http://omlc.ogi.edu/calc/mie_calc.html, "Mie Scattering Calculators" (2006)

100. V. Weidner and J. Hsia, Appl. Opt. Vol. 18 (1979)

101. J. C. Dainty, ed., *Laser Speckle and Related Phenomena*, Springer-Verlag, Berlin (1975)

102. M. Giglio, M. Carpineti, A. Vailati, and D. Brogioli, Applied Optics, Vol. 40, No. 24 (2001)

103. M. Born and E. Wolf, *Principles of Optics*, Cambridge University Press (1999)

104. B. Berne and R. Pecora, *Dynamic Light Scattering*, Wiley, New York (1974)

105. B. A. Zimm, J. Chem. Phys. 16 (1948)

106. B. A. Brice, M. Halwer, and R. Speiser, J. Opt. Soc. Am. 40 (1950)

107. S. L. Jacques, C. A. Alter and S. A. Prahl, Lasers Life Sci., Vol. 1 (1987)

108. T. Riddolls, J. R. Dutcher, C. Gigault, Review of Scientific Instruments, Vol.66, No.2 (1995)

109. W. Schärtl, Springer Laboratory, 25-37 (2007)

110. W. A. Sibley, Physical Review, Vol. 132, No. 5 (1963)

111. Y. H. Rim, J. W. Haus and J. Schroeder, Phys. Rev. A 42 (1990)

112. K. M. Mcnamara, MRS Proceedings, Vol. 588, 283 (1999)

113. R. Apetz, M. P. B. van Bruggen, Journal of the American Ceramic Society Volume 86, Issue 3 (2003)

114. Jin-Jian Chen, PhD Thesis, Boston University (1990)

115. W. J. Smith, *Modern Optical Engineering*, McGraw-Hill (2007)

116. G. S. Settles, *Schlieren and Shadowgraph Techniques*, Springer (2001)

117. R. Hooke, Micrographia, Observation LVIII, 217-219, London (1665)

118. W. Lauterborn and T. Kurz, *Coherent Optics*, Springer (2003)

119. W. Merzkirch, *Methods of Experimental Physics*, Vol. 18, Academic Press, New York (1981)

120. W. Merzkirch, *Flow Visualization*, 2nd edn., Academic Press, New York, (1987)

121. A. Vogel, I. Apitz, S. Freidank, and R. Dijkink, Opt. Lett. 31, pp. 1812-1814 (2006)

122. C. L. Stong, Scientific American, Vol. 231, No. 2 (1974)

123. A. Marion, *An Introduction to Image Processing*, Chapman and Hall (1991)

124. Http://www.cambridgeincolour.com/tutorials

125. V. Peters, L. Fornasiero, E. Mix, A. Diening, K. Petermann, and G. Huber, Conf. on Lasers and Electro-Optics Europe, Technical Digest, CFF10, pp. 379 (1998)

126. T. Sanamyan, J. Simmons, M. Dubinskii, Laser Physics Letters, Vol. 7, No. 8, pp. 569–572 (2010)

127. R. L. Aggarwal, D. J. Ripin, J. R. Ochoa, and T. Y. Fan," J. Appl. Phys. Vol. 98, No. 103514 (2005)

128. J. Matthews, *Crystan Handbook of Infra-red and ulta-voilet optical materials*, Crystan Ltd (2008)